Max-Planck-Institut
für Meteorologie

MAX-PLANCK-GESELLSCHAFT

IMPRS

Warm and sensitive Paleocene-Eocene climate

Malte Heinemann

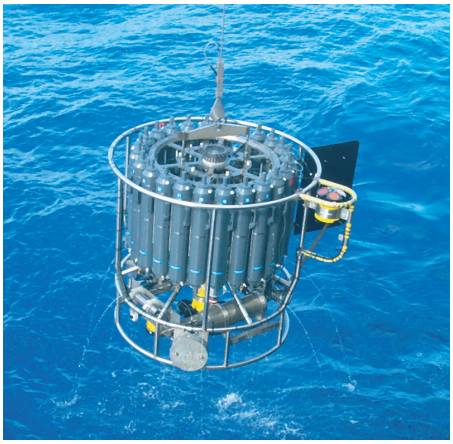

Berichte zur Erdsystemforschung 70/2009

Reports on Earth System Science

Berichte zur Erdsystemforschung 70 2009

Warm and sensitive Paleocene-Eocene climate

Dissertation zur Erlangung des Doktorgrades der Naturwissenschaften
im Department Geowissenschaften der Universität Hamburg
vorgelegt von

Malte Heinemann

aus Gifhorn

Hamburg 2009

Reports on Earth System Science 70 2009

ISSN 1614-1199

Malte Heinemann
Max-Planck-Institut für Meteorologie
Bundesstrasse 53
20146 Hamburg
Germany

Als Dissertation angenommen
vom Department Geowissenschaften der Universität Hamburg

auf Grund der Gutachten von
Prof. Dr. Jochem Marotzke
und
Dr. Johann H. Jungclaus

Hamburg, den 6. Juli 2009
Prof. Dr. Jürgen Oßenbrügge
Leiter des Department Geowissenschaften

ISSN 1614-1199

Warm and sensitive
Paleocene-Eocene climate

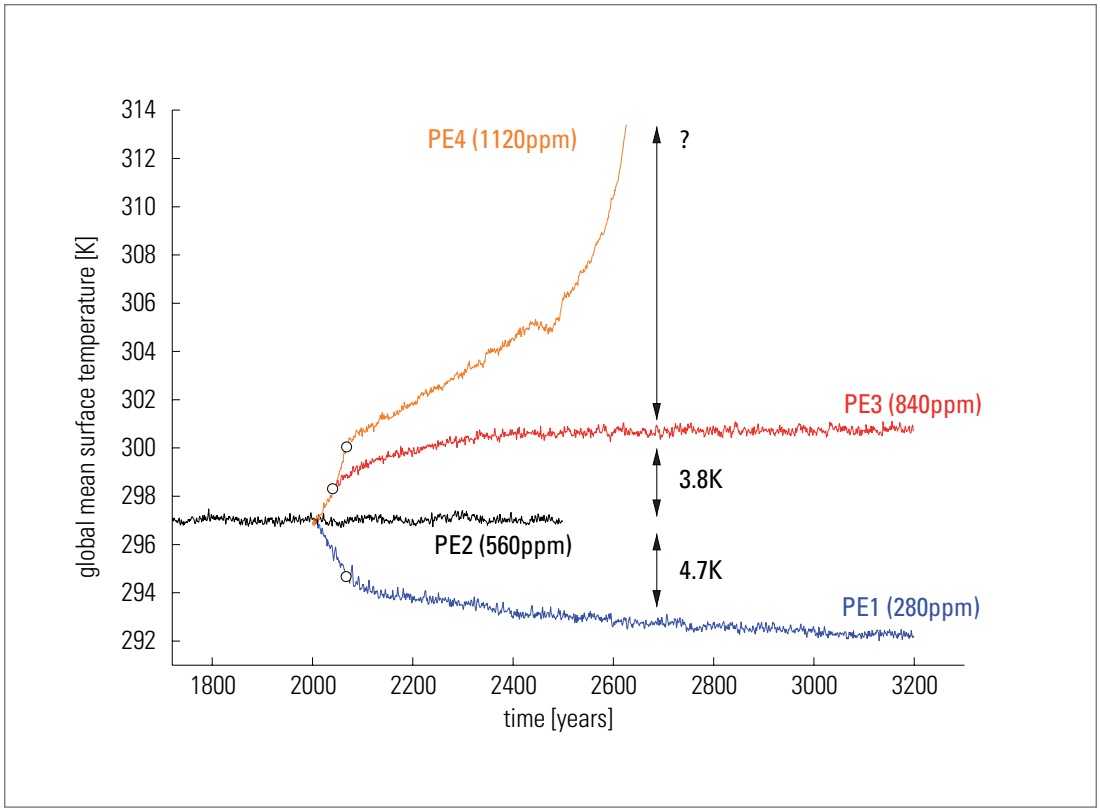

Malte Heinemann

Hamburg 2009

Abstract

We investigate the late Paleocene to early Eocene (PE) climate about 55 million years ago, and its sensitivity to a variation of atmospheric carbon dioxide concentrations (pCO_2) using the coupled atmosphere-ocean-sea ice general circulation model ECHAM5/MPI-OM.

Applying a moderate pCO_2 of 560 ppm yields a warm and ice-free climate with, compared to a pre-industrial reference, 5 to 8 K warmer low latitudes and up to 40 K warmer high latitudes. This high-latitude amplification is in line with proxy data, yet the Arctic surface temperatures may still be too low. Using a zero-dimensional energy balance model as a diagnostic tool reveals that about two thirds of the warming are due to a reduced atmospheric longwave emissivity, mostly from an increased atmospheric water vapour content. The remaining one third of the warming is due to a reduced planetary albedo. The planetary albedo reduction is caused by the lack of glaciers, the lack of sea ice, reduced snow cover, and a darker vegetation. We suggest that these local radiative effects, rather than increased meridional heat transports, were responsible for the low equator-to-pole temperature gradient during the PE.

Increasing pCO_2 from 560 to 840 ppm yields an additional surface warming of 3.8 K, further increasing pCO_2 to 1120 ppm yields a runaway climate. The warming during both pCO_2 increase experiments is caused by a decreased longwave emissivity of the clear sky atmosphere and a decreased shortwave cloud radiative effect, at a ratio of about 3:1. The large climate sensitivities have to be regarded with caution, as they may in part be caused by an artificial interaction with ozone.

Irrespective of the pCO_2, we find North Atlantic Deep Water (NADW) formation in the proto-Labrador Sea and a southward deep western boundary current in all stable simulations. The NADW becomes shallower for larger pCO_2. Southern Ocean deep water formation for a pCO_2 of 560 ppm is relatively weak, exhibits centennial oscillations, and drives a northward deep water flow in the eastern Atlantic. Decreasing pCO_2 from 560 to 280 ppm leads to the onset of strong South Pacific sinking. Increasing pCO_2 from 560 to 840 ppm yields reduced Southern Ocean sinking. We do not find sinking in the North Pacific in any of our runs.

Summing up, we present the first coupled PE climate model solution with moderate pCO_2 that shows relatively warm, sea-ice-free high latitudes, and still reasonably matches lower-latitude sea surface temperature reconstructions. Our runs do not support the notion that an ocean circulation switch triggered the Paleocene/Eocene Thermal Maximum (PETM). However, our results indicate that the PE climate was very sensitive to a variation of pCO_2, which implies that a relatively small input of carbon — possibly from methane hydrates — could have caused the warming during the PETM.

Contents

Chapter 1

Introduction

1.1 Motivation and research questions

Warm periods in the Earth's past provide a challenging test of our understanding of climate system processes and our ability to predict them (Huber et al. 2000). The late Paleocene to early Eocene (PE) about 55 to 50 million years ago was the warmest period during the Cenozoic Era (65 million years ago to present; review in Zachos et al. 2001). Moreover, the boundary between the Paleocene and the Eocene (54.8 million years ago) was marked by an extraordinary, short-lived global warming event known as the Paleocene/Eocene Thermal Maximum (PETM), also named Late Paleocene Thermal Maximum (LPTM) or Eocene Thermal Maximum 1 (ETM1), which was associated with an increase of atmospheric greenhouse gas concentrations (e.g., Dickens et al. 1995). This abrupt warm climate aberration was superimposed on the long-term warming trend during the Paleocene towards the Early Eocene Climatic Optimum (about 51 million years ago). In this study, we use the atmosphere-ocean-sea ice general circulation model (GCM) ECHAM5/MPI-OM to investigate the warm PE climate, the warming during the PETM, the role of the ocean for the PE climate, and the hypothesis that an ocean circulation change triggered the PETM.

Paleo-reconstructions suggest that high-latitudes during the PE were very warm — for example, Estes and Hutchinson (1980) suggested that alligators lived on Ellesmere Island —, while tropical and subtropical temperatures were only moderately warmer than at present (e.g., Tripati and Elderfield 2004). This indicates that the equator-to-pole temperature gradient during the PE was much lower than at present. Climate models have not been able to reproduce this low equator-to-pole temperature gradient (Barron 1987; Huber and Sloan 2001; Shellito et al. 2003). To our knowledge, there is no PE coupled climate model solution consistent with the geologic record. Hence, the first research question of this study is:

(1) Can we simulate the warm PE climate with its low equator-to-pole temperature gradient using ECHAM5/MPI-OM?

Because the previous climate models could not reproduce the low temperature gradient, it was suggested that they lack mechanisms that reduce the temperature gradient.

Proposed mechanisms include a largely increased ocean heat transport (Covey and Barron 1988; Sloan et al. 1995), or a high-latitude warming due to changing cloud properties (Sloan and Pollard 1998; Kump and Pollard 2008; Abbot and Tziperman 2008). We will attempt to answer the question:

(2) What mechanisms may have led to the warm PE climate and the low temperature gradient?

Estimates for the atmospheric CO_2 concentration (pCO_2) during the PE range from near present-day values (300 ppm, Royer et al. 2001) to more than 2000 ppm (Pearson and Palmer 2000) even before the PETM. We investigate the climate response to a variation of atmospheric pCO_2, to answer the question:

(3) What was the atmospheric pCO_2 before the PETM / how much greenhouse gas forcing do we need to match the reconstructed PE temperatures?

Paleo-reconstructions indicate that the Earth's surface at the beginning of the PETM warmed by 3 to 9 K in less than 10,000 years (Röhl et al. 2000; Thomas et al. 2002; Zachos et al. 2003; Tripati and Elderfield 2004; Sluijs et al. 2006; Zachos et al. 2006). This surface warming was associated with an input of isotopically light carbon to the atmosphere-ocean system, which led to a $\delta^{13}C$ carbon isotope excursion (CIE) of about -2.5‰ and an acidification of the ocean. The CIE and the acidification support the notion that elevated atmospheric pCO_2 drove the PETM (Bowen et al. 2004; Pagani et al. 2006b; Handley et al. 2008). Yet the source of the carbon remains a mystery (Pagani et al. 2006a). Dickens et al. (1995) suggested that dissociation of methane hydrates buried in marine sediments represented the carbon source. The amount of methane needed to explain the large CIE is relatively small, because the carbon from bacterially produced methane has a very low average $\delta^{13}C$ of -60‰ (Kvenvolden 1993). If the carbon originated from the Earth's mantle ($\delta^{13}C$ of about -25‰) or from organic carbon ($\delta^{13}C$ of about -5‰), the magnitude of the carbon addition necessary to explain the CIE would be much larger (Dickens et al. 1995). Given the source of the carbon, the magnitude of the CIE and the magnitude of the surface warming during the PETM can be used to estimate the PE equilibrium climate sensitivity to a doubling of atmospheric pCO_2. Assuming that methane was the primary driver of the PETM, Pagani et al. (2006a) computed that an equilibrium climate sensitivity of 6.8 to 7.8 K would be necessary to explain the warming. They conclude that the PETM either resulted from an enormous input of CO_2 that currently defies a mechanistic explanation, or climate sensitivity was extremely high. Previous PE modelling studies do not support such large climate sensitivities. For example, Shellito et al. (2003) found a climate sensitivity of about 2 K using a slab ocean version of the NCAR Climate System Model CSM. Recently, Winguth et al. (submitted) confirmed this low climate sensitivity using

a PE version of the fully coupled NCAR atmosphere-ocean model CCSM3. Therefore, we ask the following question:

(4) Does our PE model exhibit a large enough climate sensitivity to support the hypothesis that a methane release caused the PETM?

The methane hydrate dissociation hypothesis requires a trigger. One appealing hypothesis is that an ocean circulation switch caused rapid bottom water warming and the thermal dissociation of methane hydrates. In fact, Bice and Marotzke (2002) found an ocean circulation switch from South Pacific to North Pacific sinking, which led to a widespread bottom water warming in an ocean GCM. In their model setup, the ocean circulation switch was triggered by an increase of the strength of the hydrological cycle by 60 %. Relatively recent paleo-reconstructions of 'deep water ages' support the notion that the onset of the PETM was associated with a switch from southern sinking to northern sinking (Tripati and Elderfield 2005; Nunes and Norris 2006). The following question arises:

(5) Using a coupled GCM, can we confirm the hypothesis that an ocean circulation switch triggered the PETM?

Using a coupled GCM advances the ocean-only GCM approach of Bice and Marotzke (2002), and necessitates a different strategy in our numerical experiments. Instead of studying the effect of a stronger, prescribed hydrological cycle, we investigate the ocean circulation response to a variation of atmospheric pCO_2 with all its feedbacks, such as a variation of the hydrological cycle.

1.2 Outline of the thesis

In Chapter 2, we introduce the PE setup of the coupled atmosphere-ocean-sea ice GCM ECHAM5/MPI-OM, and we describe and analyse the PE control climate, addressing the above-defined research questions (1) and (2). In Chapter 3, Section 3.1, we investigate the sensitivity of our PE model solution to a variation of atmospheric pCO_2, addressing the research questions (3) and (4). In order to maintain numerical stability of ECHAM5 at high surface temperatures, a modification of its longwave radiative transport module becomes necessary. We motivate and describe this modification in Section 3.2. Moreover, we adapt the prescribed ozone climatology to increased tropopause heights. This adaptation of the ozone climatology is necessary to avoid artificial warming in response to too high ozone concentrations in the upper troposphere. We motivate this ozone adaptation and investigate the sensitivity of our PE simulations with respect to this ozone adaptation in Section 3.3. In Chapter 4, we concentrate on the role of the ocean circulation for the PE climate, and investigate the possibility of

an ocean circulation switch as a trigger for the PETM, addressing our last research question (5). We present our conclusions and an outlook in Chapter 5.

Chapter 2 has been submitted for publication in *Climate of the Past*, and it has been published in the journal's access reviewed discussion forum [1]. Similarly, the Chapters 3 and 4 are intended as paper drafts, and each of them can be read on its own.

[1] Heinemann, M., Jungclaus, J. H., and Marotzke, J.: Warm Paleocene/Eocene climate as simulated in ECHAM5/MPI-OM, Climate of the Past Discussions, 5, 1297-1336, 2009.

Chapter 2

Warm PE climate

2.1 Introduction

Simulating warm periods in Earth history is a major challenge in climate research. The very warm climates during the late Cretaceous to early Paleogene (about 100 to 35 Million years ago) seem especially problematic, since model results are not consistent with paleo-reconstructions of low pole-to-equator temperature gradients and reduced seasonalities on high-latitude continents. In this study, we aim at reducing this gap between modelling and proxy data for the late Paleocene to early Eocene (PE), about 50 to 55 million years ago. To this end, we set up a PE version of the coupled atmosphere-ocean-sea ice general circulation model (GCM) ECHAM5/MPI-OM. Using a simple energy balance model, we quantify the mechanisms that lead to the warm climate in our PE GCM.

Evidence for the warm PE climate is provided by a wide range of proxies. Sea surface temperatures (SSTs) inferred from oxygen isotopes, Mg/Ca ratios, and biomarkers suggest that the tropics were moderately warmer than at present, while high latitudes and especially Arctic temperatures were much warmer (e.g., Thomas et al. 2002; Tripati and Elderfield 2004; Zachos et al. 2003, 2006; Sluijs et al. 2006). Estes and Hutchinson (1980) found warm-climate proxies such as salamanders, lizards, snakes, turtles, and an alligator on the Canadian Archipelago (see also Markwick 1994, 1998). Greenwood and Scott (1995) inferred from the existence of high-latitude palm trees that a large part of the Earth surface, including continental interiors, had climates with winter temperatures much higher than today.

Climate models, employing large greenhouse gas concentrations, have been able to reproduce the high mean temperature of the PE (e.g., Shellito et al. 2003). However, it has long been noticed that they fail to match the low pole-to-equator temperature gradient (e.g., Barron 1987). Note that, when Barron (1987) discussed the low pole-to-equator temperature gradient problem, it was believed that tropical SSTs during the PE were even lower than at present (e.g., Shackleton and Boersma 1981). This led Barron (1987) to the conclusion that 'the Eocene polar warmth could be explained by an energy redistribution, a more efficient poleward heat transport, and external factors

would be not required'. Ever since, tropical temperature reconstructions have been adjusted towards warmer conditions (e.g., Sexton et al. 2006). If very high tropical temperatures are confirmed by further proxy analyses, the mismatch between models and proxy data may be reduced further (Huber 2008).

Taking the warm poles, relatively cold tropics, and reduced seasonality at face value, it has been suggested that the climate models lack one or more mechanisms that lead to such a so-called 'equable' climate. Increased ocean heat transport has often been invoked to explain the problematic warm poles (e.g., Covey and Barron 1988). Sloan et al. (1995) estimated that a 30% increase in (total) poleward heat transport would be required to maintain Eocene high-latitude temperatures. Huber and Sloan (2001) revisited the hypothesis of increased oceanic heat transport, and simulated the Eocene with a fully coupled atmosphere-ocean-sea ice GCM, the Climate System Model (CSM) version 1 developed at the National Center for Atmospheric Research (NCAR). Their Eocene model solution showed a near-modern meridional temperature gradient, and a near-modern oceanic heat transport. They concluded that the theory of increased ocean heat transport for maintaining low temperature gradients was incorrect or incomplete. Other hypotheses draw on local radiative changes rather than heat transport. Sloan and Pollard (1998) suggested that, given high atmospheric methane concentrations, polar stratospheric clouds might contribute to a high-latitude warming. Kump and Pollard (2008) found that increased cloud droplet radii and precipitation efficiency could cause an additional warming and high-latitude amplification. They argued that this change of the cloud properties could have been a response to a reduced global primary production by temperature stress, causing a reduction in cloud condensation nuclei concentration. Abbot and Tziperman (2008) suggested another mechanism related to clouds. They argued that deep convection during winter in ice-free high-latitude oceans might lead to high-latitude warming.

Still, to our knowledge, there is no PE model solution consistent with the geologic record. Modelling the PE remains a major challenge in climate research. We aim at testing whether the model-proxy data mismatch persists in a PE setup of the state-of-the-art coupled model ECHAM5/MPI-OM.

The boundary between the Paleocene and the Eocene is marked by an extraordinary, short-lived global warming event known as the Paleocene/Eocene Thermal Maximum (PETM), also named Late Paleocene Thermal Maximum (LPTM) or Eocene Thermal Maximum 1 (ETM1). This event is associated with a massive increase of atmospheric greenhouse gas concentrations (e.g., Dickens et al. 1995), and is frequently assumed to be an analogue for future greenhouse warming scenarios (e.g., Alley et al. 2002). Note that we aim at modelling the already warm background climate during the PE, not the PETM itself.

To better understand the processes that lead to the warm PE climate in our model, we compare the PE simulation to a pre-industrial reference simulation (PR). We briefly

analyse the atmospheric and oceanic meridional heat transports in the PE model solution compared to PR. However, this study focuses on understanding the radiative effects responsible for the warm PE climate. Using a simple energy balance model, we assign the simulated warming of the PE climate compared to the PR climate to greenhouse gas forcing, albedo changes, cloud feedback processes, orographic effects, and orbital changes.

The chapter is organised as follows. In Section 2.2, we describe the atmosphere-ocean-sea ice GCM ECHAM5/MPI-OM, focussing on the settings specific to the PE. In Section 2.3, we describe the simulated PE climate, briefly compare it to the geologic record, and highlight differences compared to PR. In Section 2.4, we analyse the different mechanisms that lead to the warm PE climate in our simulation. In Section 2.5, we present a discussion and conclusions.

2.2 Numerical model setup

The model ECHAM5/MPI-OM is based on the tropospheric model ECHAM5 resolving the atmosphere up to 10 hPa, the ocean-sea ice model MPI-OM, and the OASIS coupler. In this chapter, we describe the basic model properties, boundary conditions, and parameter choices we use in our PE setup of ECHAM5/MPI-OM.

2.2.1 Atmosphere model (ECHAM5)

The atmosphere general circulation model ECHAM5 (here: version 5.3, Roeckner et al. 2003) has been developed from the operational forecast model of the European Centre for Medium-Range Weather Forecasts (ECMWF) and a parameterisation package developed in Hamburg. ECHAM5 has a spectral dynamical core that solves the equations for vorticity, divergence, temperature and the logarithm of surface pressure in terms of spherical harmonics with a triangular truncation. Transport of water vapour, cloud liquid water, and cloud ice is computed on a Gaussian grid, using a flux-form semi-Lagrangian scheme (Lin and Rood 1996). We use the spectral truncation T31, which corresponds to a Gaussian grid with a gridpoint spacing of approximately 3.75°.

The shortwave radiation scheme (Fouquart and Bonnel 1980) has four spectral bands, one for visible and ultraviolet, and three for the near infrared. The scheme includes Rayleigh scattering, absorption by water vapour, ozone (O_3), carbon dioxide (CO_2), methane (CH_4) and nitrous oxide (N_2O). Water vapour is a prognostic variable. Ozone is interpolated in time from a monthly zonal mean climatology (Fortuin and Kelder 1998). Carbon dioxide, methane and nitrous oxide are assumed to be uniformly mixed. Carbon dioxide estimates for the PE range from 300 ppm to more than 2000 ppm before the PETM, and even higher concentrations during the PETM (e.g., Pearson and Palmer 2000; Royer et al. 2001). Since we aim at simulating the PE background climate, we

use a relatively low carbon dioxide concentration of 560 ppm, which is twice the pre-industrial value. There is no proxy available for methane nor for nitrous oxide. For simplicity, methane and nitrous oxide are set to pre-industrial values (concentrations given in Table 2.1).

Longwave radiation is computed in the Rapid Radiative Transfer Model (RRTM) developed by Mlawer et al. (1997). The RRTM scheme computes fluxes in the spectral range $10\,\mathrm{cm}^{-1}$ to $3000\,\mathrm{cm}^{-1}$. The computation is organised in 16 spectral bands and includes line absorption by water, carbon dioxide, ozone, methane, nitrous oxide, and aerosols. Aerosol distributions are prescribed following Tanré et al. (1984).

The cloud scheme consists of prognostic equations for water vapour, liquid and solid water, and bulk cloud microphysics. Cloud cover is computed diagnostically from relative humidity following Lohmann and Roeckner (1996).

We interpolate the orography from a 55 Ma $2^\circ \times 2^\circ$geography reconstructed by Bice and Marotzke (2001) (Fig. 2.1a). The standard version of ECHAM5 utilises a parameterisation developed by Lott and Miller (1997) to account for interactions between subgrid-scale orography (SSO) and the atmospheric flow. This SSO parameterisation needs the standard deviation, anisotropy, slope, orientation, minimum, maximum, and mean elevation of the orography for each gridpoint. Since we do not have that information for the PE, we switch the SSO parameterisation off in the PE run.

For simplicity, we prescribe a globally homogeneous vegetation (parameters given in Table 2.1), which is characterised by a lower albedo compared to the PR average, a slightly larger leaf area index, and a larger forest fraction, consistent with a larger fraction of high-latitude and dark, tropical forests (see, e.g., Utescher and Mosbrugger 2007, for an Eocene vegetation reconstruction). The leaf area index does not vary seasonally in the PE setup. We prescribe a surface roughness length that resembles the pre-industrial average over land. The soil and vegetation parameter settings are akin to a present-day, woody savanna during its growing season (Hagemann et al. 1999; Hagemann 2002).

River runoff is treated interactively in the atmosphere model, and the respective fresh water flux is passed to the ocean as part of the atmospheric freshwater flux field. In our PE setup, we assume that rivers flow along the geopotential height gradient but overleap valleys such that no lakes are formed.

Orbital parameters in our PE simulation are set to constant values (see Table 2.1). The longitude of perihelion, the obliquity, and the eccentricity as computed by Laskar et al. (2004) vary on timescales much shorter than the length of the PE period (Fig. 2.2). Moreover, Laskar et al. (2004) reported that their simulation of the orbital parameters becomes uncertain for more than 40 to 50 Ma ago. We select a longitude of perihelion such that the northern hemisphere winter occurs in the aphelion (almost like today). The present-day obliquity and eccentricity are rather extreme values. For the PE, we select an obliquity and an eccentricity closer to the temporal average of the solution by

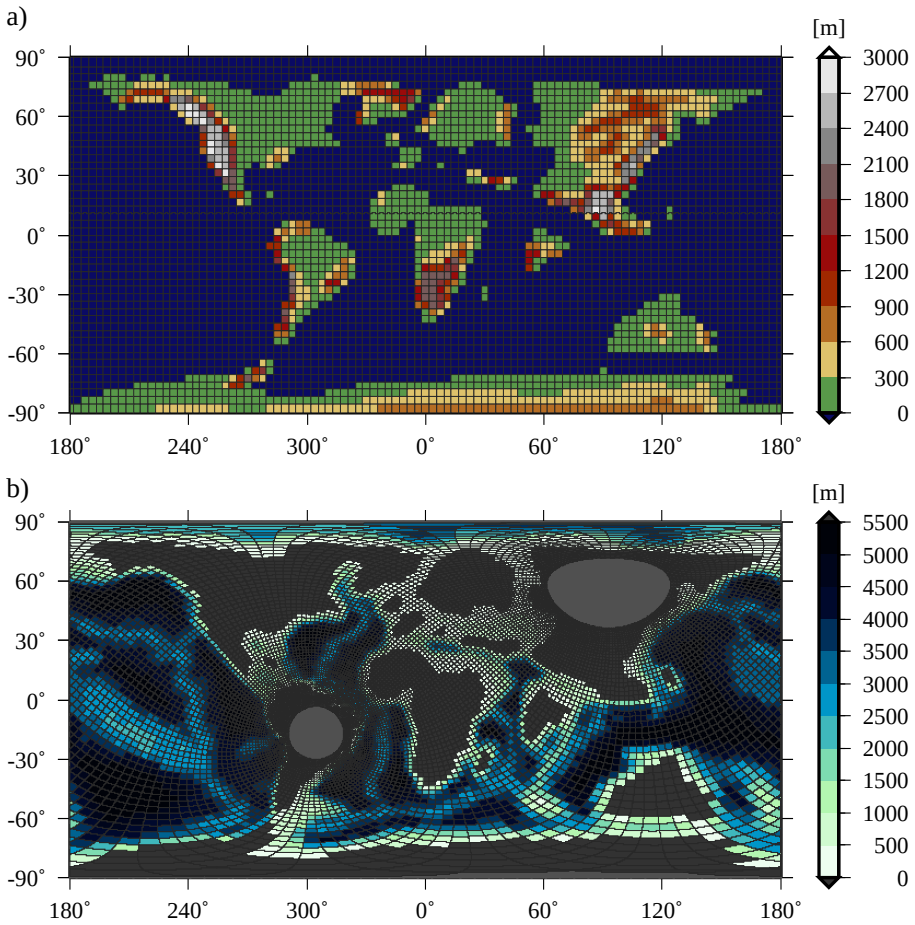

Figure 2.1: (a) PE orography interpolated on the Gaussian grid that corresponds to the T31 spectral truncation; displayed orography not spectrally filtered. (b) PE bathymetry as used in MPI-OM.

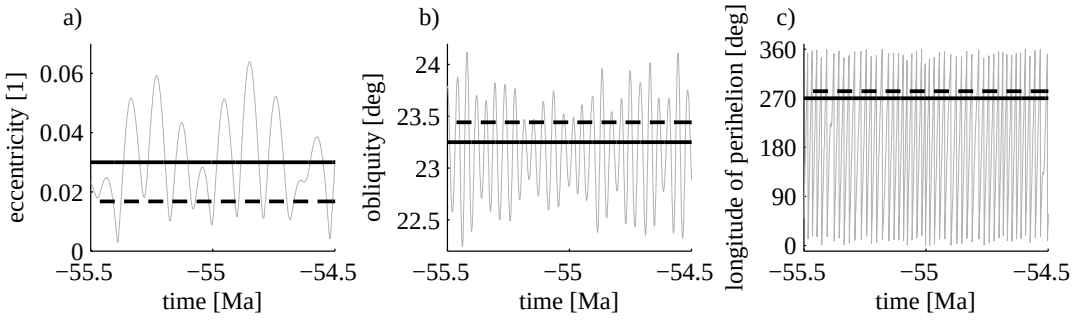

Figure 2.2: (a) Eccentricity, (b) obliquity, and (c) longitude of perihelion as computed by Laskar et al. (2004) (thin grey line), constant values as used for the PE setup (heavy black), and pre-industrial values (heavy black, dashed; for the year 2000 a.d. according to Berger 1978, see also Table 2.1).

Laskar et al. (2004, see Fig. 2.2).

2.2.2 Ocean and sea ice model (MPI-OM)

The Max-Planck-Institute Ocean Model (MPI-OM, here: version 1.2) is a z-coordinate global GCM based on the primitive equations for a hydrostatic Boussinesq fluid with a free surface (Marsland et al. 2003). Scalar and vector variables are formulated on an orthogonal curvilinear C-grid (Arakawa and Lamb 1977). Along-isopycnal diffusion is implemented following Griffies (1998). Horizontal tracer mixing by unresolved eddies is parameterised following Gent et al. (1995). For the vertical eddy viscosity and diffusion the Richardson-number dependent scheme of Pacanowski and Philander (1981) is applied. Since the Pacanowski-Philander (PP) scheme in its classical form underestimates the turbulent mixing close to the surface, an additional wind mixing parameterisation is included. In the presence of static instability, convective overturning is parameterised by greatly enhanced vertical diffusion. A bottom boundary layer slope convection scheme allows for an improved representation of the flow of statically unstable dense water over sills. The effect of ocean currents on surface wind stress is accounted for following Luo et al. (2005). The embedded sea ice model consists of sea ice dynamics following Hibler (1979) and zero-dimensional thermodynamics following Semtner (1976). For more details on MPI-OM and the embedded sea ice model see Marsland et al. (2003) and Jungclaus et al. (2006).

To apply MPI-OM to the PE, we include the PE bathymetry and generate an appropriate model grid. As for the orography in the atmospheric model, we interpolate the bathymetry from the reconstruction by Bice and Marotzke (2001). The MPI-OM

parameter	*PR*	*PE*
carbon dioxide concentration (pCO_2)	278 ppm	560 ppm
methane concentration (pCH_4)	0.65 ppm	0.8 ppm
nitrous oxide concentration (pN_2O)	0.27 ppm	0.288 ppm
total solar irradiance	1367 W m^{-2}	1367 W m^{-2}
eccentricity of the Earth's orbit	0.0167	0.0300
obliquity or inclination of the Earth's axis	23.44^o	23.25^o
longitude of perihelion	283^o	270^o
land surface background albedo	0.25	0.16
sea surface albedo	0.07	0.07
vegetation ratio	0.4	0.4
leaf area index (LAI)	2.2	2.3
forest fraction	0.26	0.40
maximum field capacity of soil (single bucket water height)	0.6 m	1.2 m
FAO soil data flag (1∼sand, 3∼mud, 5∼clay)	2.6	3
surface roughness length over land	1.6 m	1.6 m

Table 2.1: ECHAM5 input parameters as used in the PE model setup compared to those in the pre-industrial reference run (PR); FAO determines volumetric heat capacity and thermal diffusivity of soil; note that, while the PE land surface is homogeneous, the land surface parameters for PR are spatially variable; the PR values given here are mean values. The pre-industrial orbital parameters are given for the year 2000 a.d. according to Berger (1978) while, actually, the orbital parameters in PR vary temporally according to VSOP87 (Variations Séculaire des Orbites Planétaires, Bretagnon and Francou 1988).

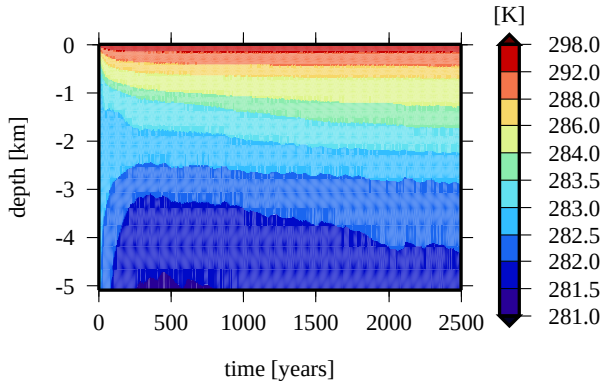

Figure 2.3: Hovmöller diagram of the global ocean potential temperature in the PE simulation (50 year running mean).

grid structure allows for an arbitrary placement of the grid poles; we generate a grid with a grid-North Pole on Paleo-Asia and a grid-South Pole on Paleo-South America (Fig. 2.1b). This model grid has several advantages. Positioning the grid-poles over land removes the numerical singularities associated with the convergence of meridians at the geographical poles. Positioning the grid-poles on *wide* landmasses allows us to reduce the total number of gridpoints. Moreover, this setup yields a higher resolution of many small but important seaways (e.g., open North Atlantic, Central American Seaway, Tethys Seaway, India-Eurasia gateway; Bice and Marotzke 2002). The grid spacing varies between 70 km around South America and 430 km in the Pacific. We use 40 levels in the vertical, of which 9 levels are in the uppermost 100 meters and 18 levels in the uppermost 500 meters.

2.2.3 Model spinup

To approach the equilibrium PE climate state, we run the model for 2500 years. The atmosphere and the ocean are initialised at rest. The ocean is initialised at a potential temperature of 283 K, and a salinity of 34.3 psu, which is approximately the salinity we would get in the present-day ocean if all glaciers melted completely. The atmosphere approaches its equilibrium after some 150 years, whereas in most ocean basins the transient phase lasts for about 1000 years. After 1000 years, the globally averaged temperatures even at the deepest levels only increase by less than 0.3 K per 1000 years (Fig. 2.3).

The Arctic deep ocean takes especially long to equilibrate, since it is only connected to the other basins via shallow sills. Moreover, the Arctic is stratified due to fresh surface water that inhibits vertical mixing. After 2000 years, the Arctic deep ocean is

8 to 10 K warm and still warming by more than 1 K per 1000 years (not shown).

2.2.4 Pre-industrial reference (PR)

In this study, we compare the PE simulation to a 2200 year long ECHAM5/MPI-OM simulation with pre-industrial boundary conditions that has been initialised from Levitus data. We refer to this pre-industrial reference simulation as PR. The pre-industrial boundary conditions include the bathymetry, orography, greenhouse gas concentrations, soil and vegetation properties, and orbital parameters (Table 2.1). The pre-industrial boundary conditions also include the subgrid-scale orographic information; the SSO parameterisation is switched on. Moreover, PR uses a modified physical parameterisation of friction and diffusion to improve the representation of the El Niño-Southern Oscillation (ENSO, see Jungclaus et al. 2006), while PE uses the standard MPI-OM parameter settings as specified by Marsland et al. (2003). While the orbital parameters in PE are constant, the parameters in PR vary temporally according to VSOP87 (Variations Séculaire des Orbites Planétaires, Bretagnon and Francou 1988). The philosophy behind this approach is to compare the PE simulation to an as good as possible representation of the pre-industrial climate.

An alternative approach to set up a pre-industrial reference would be to degrade the pre-industrial boundary conditions to the level of accuracy available for the PE (see, e.g., Huber et al. 2003), which would worsen the representation of the pre-industrial climate. Such a degradation would also include to switch off the SSO parameterisation.

To test the effect of the SSO parameterisation, and to ensure that neither the ENSO-tuning nor the dynamic orbital parameters have a major effect on the pre-industrial climate, we perform a 400 year long pre-industrial sensitivity run. This sensitivity run restarts from PR, it does not use the SSO parameterisation nor the ENSO-tuning, and it uses constant orbital parameters as specified in Table 2.1. Moreover, it uses the PE concentrations of nitrous oxide and methane (Table 2.1), and a carbon dioxide concentration of 280 ppm (instead of 278 ppm). We find that these differences in the model setup compared to PR lead to a global warming of approximately 0.8 K. The warming is largest at northern high latitudes, where it reaches up to 3 K. However, the differences between this pre-industrial sensitivity run and PR remain small compared to the differences between PE and PR. Using the pre-industrial sensitivity run instead of PR would lead to a small modification of some quantitative results, but the general results and conclusions of this work are not affected.

2.3 Description of simulated PE climate

The aim of this section is to describe the simulated PE climate, to briefly compare it to proxy data, and to identify the main differences between PE and PR.

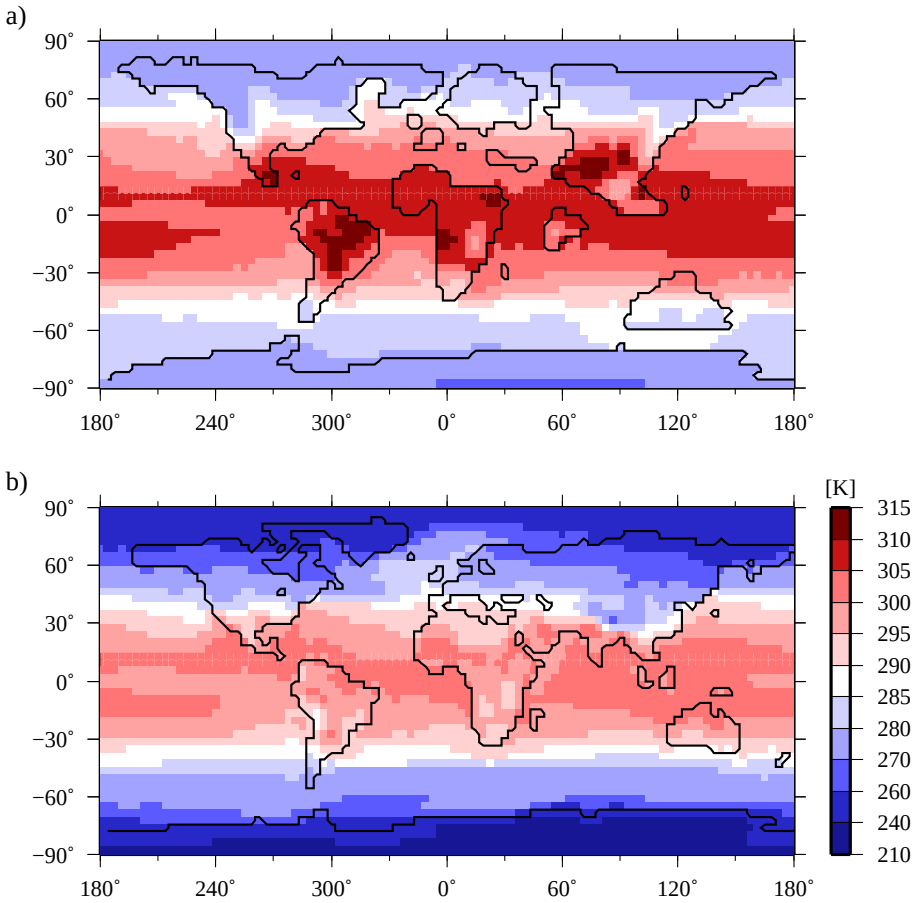

Figure 2.4: Annual mean surface temperature averaged over the last 200 years of (a) PE, and (b) the pre-industrial reference (PR).

2.3.1 Surface temperature

The simulated PE Earth's surface is on average 297 K warm and basically ice-free. There is one small area in the Weddell Sea, and one small area north of proto-Greenland that do have a little bit of sea ice in a few, exceptionally cold winters. The sea ice fraction in these areas amounts to less than 0.1% with a sea ice thickness of less than 3 mm.

The highest annual mean surface temperatures of 313 to 314 K occur in low altitude areas of South Asia, some areas in central South America, and Africa (Figure 2.4a). During local summers, surface temperatures reach up to 325 K in South Asia, 322 K in central South America, and 318 K in North Africa (temperatures are 200-year means of the warmest month).

The lowest annual mean surface temperatures of about 270 K occur over the Antarctic continent. Antarctic summer surface temperatures are around 295 K even at the coldest places. In the northern hemisphere, the lowest surface temperature of 271 K occurs in the Rocky Mountains, where monthly means vary between 261 K and 285 K. The Arctic has the coldest summers on the PE globe; the warmest Arctic monthly mean SSTs only reach about 280 K.

Local winter snow depths reach 1.2 m in the Rocky Mountains, 40 cm in Greenland, 30 cm on the Antarctic continent, and 20 cm in Siberia. During local summers all the snow melts away; there is no long-term snow accumulation.

2.3.2 Comparison to proxy data

We select six different SST reconstructions from the literature to compare them to the simulated zonal mean SSTs (Figure 2.5a). We find that five of the six selected SST reconstructions are close to the simulated seasonal variability of the zonal means. One reconstruction differs very much from the simulated zonal mean SST: Sluijs et al. (2006) inferred Arctic SSTs of about 291 K from the biomarker TEX_{86}. The reconstruction may, however, be biased toward summer SSTs. The simulated monthly mean Arctic SSTs vary between 276 and 280 K. Thus, the simulated Arctic surface is 11 to 13 K colder than inferred by Sluijs et al. (2006).

The annual mean SSTs in the proto-Labrador Sea amount to about 290 K. Note that Ellesmere Island, where Estes and Hutchinson (1980) found the varanid, tortoise and alligator remains, is in the vicinity of the Labrador Sea. According to Markwick (1998), the minimum thermal limit for crocodiles is a coldest-month mean temperature of 278.7 K. While our coldest-month proto-Labrador Sea surface temperature amounts to more than 285 K, our coldest-month land surface temperatures in the vicinity of the proto-Labrador Sea fall just below 270 K. Note that SSTs in the proto-Labrador Sea are about 7 K warmer than SSTs in the North Pacific at similar latitudes. We will attempt to explain this zonal temperature difference in Chapter 4. North American continental temperatures east of the Rocky Mountains amount to more than 285 K, and monthly means are above freezing all year round south of 55° N in that area. This relatively warm area matches the continental area where Markwick (1994) found fossil crocodiles.

2.3.3 PE-PR temperature differences

The PE surface is on average 9.4 K warmer than the PR surface (Table 2.2). We find a large high-latitude amplification of this warming (Figure 2.5b). The low-latitude zonal mean PE surface temperatures are about 5 to 8 K warmer than in PR, while northern high latitudes are warmer by up to 20 K, and southern high latitudes are warmer by up to 40 K. The SST PE-PR differences are smallest in the South Atlantic and North

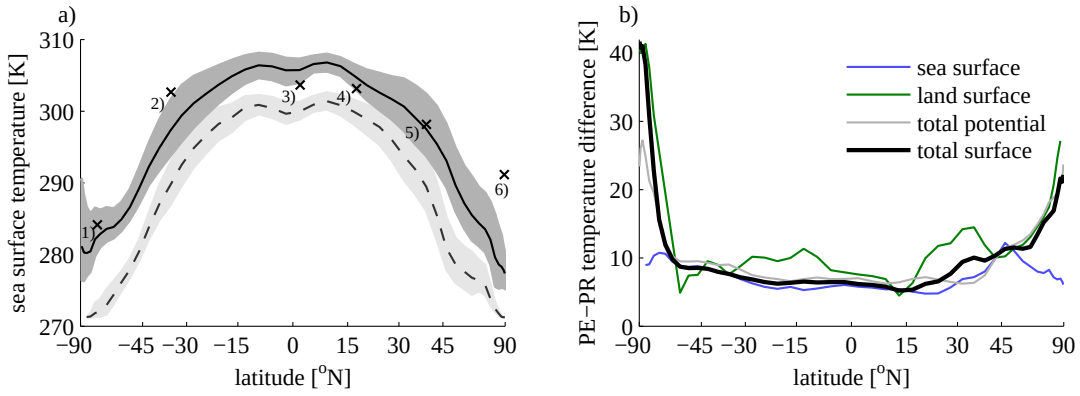

Figure 2.5: (a) Sea surface temperature in PE (solid), and in PR (dashed); the shading indicates the seasonal variability of the 200-year climatology (differences between the warmest and coldest months); crosses are SST estimates from proxy data for the pre-PETM published by 1) Thomas et al. (2002) based on δ^{18}O, 2) and 3) Tripati and Elderfield (2004) based on Mg/Ca ratios assuming the Mg/Ca ratio of seawater to be 5.15 mmol/mol, 4) Zachos et al. (2003) based on TEX_{86}, 5) Zachos et al. (2006) based on TEX_{86}, 6) Sluijs et al. (2006) based on TEX_{86}. (b) Annual mean temperature differences between PE and PR for the total surface (heavy, black), the dry potential temperature at the global mean surface pressure of 985.5 hPa (grey), only land surface (green), and only sea surface (blue). The horizontal scale is such that the spacing between the latitudes is proportional to the area of the Earth's surface between them, i.e., is linear in the sine of the latitude.

and South Pacific subtropical gyres at about ±15° N. The PE zonal mean SSTs are about 5 K warmer at low latitudes, about 10 K warmer in the Southern Ocean, and up to 12 K warmer at 45° N.

While the surface temperature PE-PR difference increases towards higher latitudes, the SST PE-PR difference north of 50° N decreases towards the North Pole. This difference occurs because the SSTs in PR cannot fall below the freezing point of sea water. Over land, the surface temperature as defined in ECHAM5 is computed from the energy balance at the land surface - atmosphere interface. It is not identical but close to the 2 m air temperature. Over water, the surface temperature in ECHAM5 is identical to the SST, which in MPI-OM is the mean temperature of the uppermost, 12 m thick layer. In the presence of sea ice, the surface temperature is defined as the temperature at the sea ice - atmosphere interface. Note that PE is basically sea ice free, while PR has sea ice both in the northern and in the southern hemisphere (see below-freezing surface temperatures in Figure 2.4b). At least 80% of the PR Arctic ocean remain sea-ice covered all year round, the average sea ice thickness amounts to about 3 m. During the northern hemisphere winter, the sea ice extends to about 50° N. The Antarctic sea ice border in the southern hemisphere winter reaches about 65° S, most of the Antarctic sea ice is less than 1 m thick.

2.3.4 Differences in the hydrological cycle

Compared to PR, the PE hydrological cycle is intensified by about 25% (Figure 2.6). Convective precipitation is higher by about 0.3 m per year (20 to 30%) at low latitudes between ±10° N. Also, convective precipitation is higher by about 0.2 m per year at latitudes higher than 30°, which is remarkable since there is hardly any convective precipitation at high latitudes in PR. This is consistent with the hypothesis that convective clouds cause high-latitude warming in PE (Abbot and Tziperman 2008). The PE peak large-scale precipitation is higher than in PR by more than 0.2 m per year, and it is shifted to higher latitudes. Snowfall is reduced and occurs at higher latitudes only. Evaporation is enhanced by -0.2 to -0.4 m per year with the largest absolute changes in the northern-hemisphere low latitudes, and the largest relative changes at the poles.

2.3.5 Meridional heat transport

The total PE and PR atmospheric heat transports are fairly symmetric about the equator, with maximum poleward transports of about 5.3 PW (1 PW=10^{15}W) at ±40° N. We find that the meridional transport of latent heat is increased in PE compared to PR, especially the poleward transports around ±45° N, and the equatorward transport in the northern Hadley cell (around 15° N). The meridional transports of dry static energy reduce such that the total atmospheric heat transport in PE and PR hardly differ from each other (Figure 2.7a).

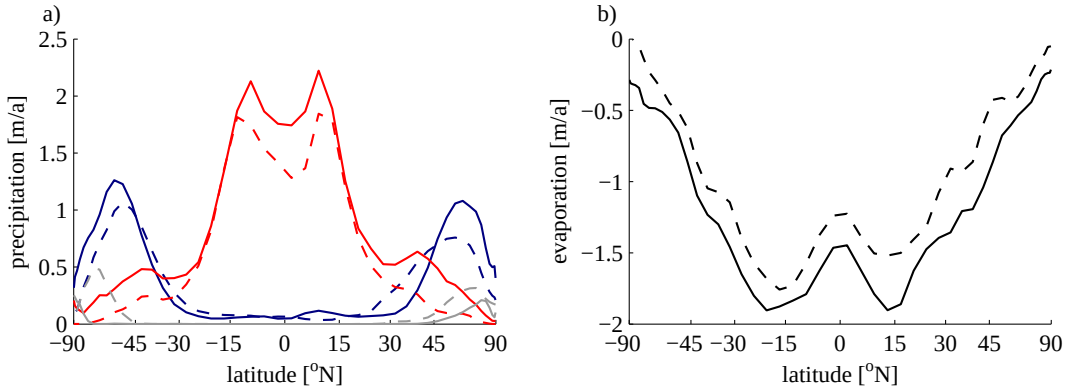

Figure 2.6: (a) Zonal mean convective precipitation (red), large scale precipitation (dark blue), and snowfall (grey); (b) zonal mean evaporation; both precipitation and evaporation are diagnosed from the last 200 years of PE (solid) and PR (dashed). The horizontal scale is linear in the sine of the latitude.

The maximum northward heat transport in PE is about 0.5 PW smaller than in PR. We find that most of this difference is due to a decreased heat transport by the meridional overturning circulation (MOC, see Figure 2.7b). However, the poleward oceanic gyre heat transport across 45° N is also reduced by almost 0.4 PW in PE compared to PR.

2.4 Analysis of mechanisms causing PE-PR differences

The aim of this section is to isolate and quantify the most important mechanisms that lead to the surface temperature differences between PE and PR.

2.4.1 Zero-dimensional energy balance model (EBM)

The Earth's surface in PE is on average 9.4 K warmer than in PR (Table 2.2). To better understand this large difference in surface temperature, we first compare the planetary albedos and the effective longwave emissivities in PE to those in PR. The PE planetary albedo is smaller by 0.026 (Table 2.2); less shortwave radiation is reflected by the atmosphere. This causes PE to be warmer than PR. The PE effective longwave emissivity is smaller by 0.044; the fraction of the longwave radiation emitted at the surface and leaving the top of the atmosphere is reduced. This also causes PE to be warmer than PR.

To quantify these effects, we apply a zero-dimensional energy balance model (EBM)

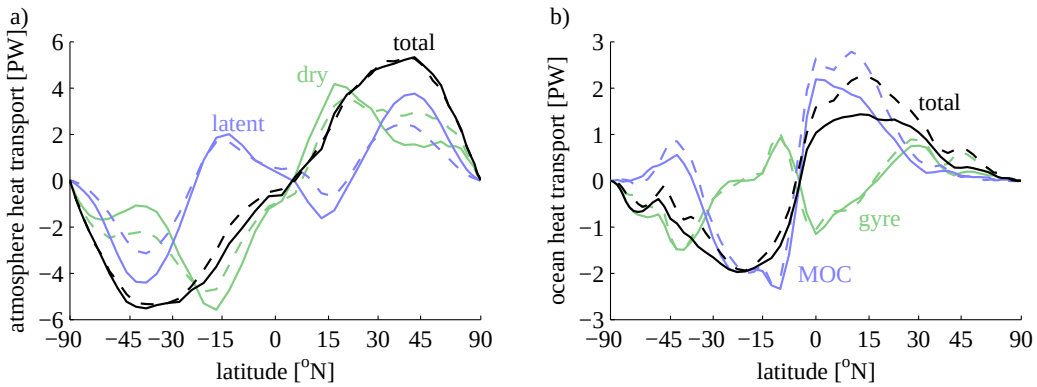

Figure 2.7: (a) Zonally integrated meridional heat transport in the atmosphere due to the advection of dry air (green), due to the advection of moisture/latent heat (blue), and the sum (black), for PE (solid) and PR (dashed), computed from the last 100 years of each run with 6 hourly instantaneous sampling; (b) zonally integrated oceanic meridional transport of internal energy due to the meridional overturning circulation (MOC, blue), due to the gyre circulation (green), and the sum (black), for PE (solid) and PR (dashed), computed from monthly means of the last 1000 years of each run. The horizontal scale is linear in the sine of the latitude.

parameter	*PR*	*PE*
surface temperature τ_s	287.6 K	297.0 K
mean surface pressure	985.5 hPa	985.5 hPa
mean sea level pressure (SLP)	1012 hPa	1001 hPa
potential temperature at SLP	289.9 K	298.4 K
planetary albedo α	0.318	0.292
clear sky planetary albedo α_c	0.173	0.133
surface albedo α_s	0.137	0.094
effective emissivity ϵ	0.585	0.541
clear sky effective emissivity ϵ_c	0.658	0.608
surface temperature $\tau_{s,ebm}$	289.5	298.0
surface temperature $\tau_{s,ebm,c}$	295.7	304.9
longwave cloud radiative forcing (CRF)	28.8 $\mathrm{Wm^{-2}}$	29.6 $\mathrm{Wm^{-2}}$
upward longwave radiation at the surface LW_s^{up}	-395 $\mathrm{Wm^{-2}}$	-445 $\mathrm{Wm^{-2}}$
shortwave CRF	-49.6 $\mathrm{Wm^{-2}}$	-54.3 $\mathrm{Wm^{-2}}$
total cloud cover	0.617	0.576
vertically integrated water vapour	25.5 $\mathrm{kg\,m^{-2}}$	45.3 $\mathrm{kg\,m^{-2}}$
spectrally filtered surface height h	231 m	141 m

Table 2.2: Some key global mean climate parameters; while τ_s is the global mean surface temperature as diagnosed from the GCM, $\tau_{s,ebm}$ is the EBM derived surface temperature (see Eq. (2.1)) using the GCM diagnosed planetary albedo α and effective longwave emissivity ϵ, $\tau_{s,ebm,c}$ is computed from the clear sky values α_c and ϵ_c.

that equates incoming shortwave radiation and outgoing longwave radiation for a grey atmosphere:

$$\frac{S_0}{4}(1-\alpha) = \epsilon\sigma\tau_{s,ebm}^4 \tag{2.1}$$

where $\tau_{s,ebm}$ is the surface temperature predicted by the EBM, S_0=1367 $\mathrm{Wm^{-2}}$ the total solar irradiance, and σ=5.67·10^{-8}$\mathrm{Wm^{-2}K^{-4}}$ the Stefan-Boltzmann constant. The factor 1/4 accounts for the difference between the area of the circular Earth profile in the sunshine, and the area of the spherical Earth. We derive the planetary albedo α and the effective longwave emissivity ϵ from the globally averaged radiative fluxes in our coupled GCM

$$\alpha = \frac{SW_t^{up}}{SW_t^{down}}\ , \quad \epsilon = \frac{LW_t^{up}}{LW_s^{up}} \tag{2.2}$$

where SW_t^{up} and SW_t^{down} are the upward and downward shortwave fluxes at the top of the atmosphere, and LW_t^{up} and LW_s^{up} are the upward longwave fluxes at the top of the atmosphere and the surface, respectively.

The EBM (2.1), fed with these albedos and emissivities, yields surface temperatures of 298.0 K and 289.5 K for the PE and PR simulations, respectively (Table 2.2). These temperatures are off the GCM temperatures by less than 2 K. The EBM temperature difference between PE and PR of about 8.5 K compares relatively well to the 9.4 K temperature difference in the GCM. According to the EBM, about 5.7 K of the warming are due to the reduced emissivity of longwave radiation, and about 2.8 K are due to the reduced planetary albedo (Figure 2.8). The PE-PR *planetary* albedo difference is in line with the PE-PR *surface* albedo difference of −0.043. The largest zonal mean PE-PR surface albedo differences are located at high latitudes (Figure 2.9). This is in part caused by our assumption that there are no glaciers in PE. The other main factor is that PE, in contrast to PR, is basically sea ice free. Moreover, there is less high-latitude snowfall in PE compared to PR (Section 2.3.1). Notice that the planetary albedo change is smaller than the surface albedo change because of cloud effects (see Section 2.4.2).

2.4.2 Cloud radiative forcing

To estimate the effect of clouds in both GCM simulations, we again apply the EBM (Eq. (2.1)). This time, however, we use the *clear sky* radiative fluxes to compute the clear sky albedo α_c and clear sky effective longwave emissivity ϵ_c

$$\alpha_c = \frac{SW_{t,c}^{up}}{SW_t^{down}} \ , \quad \epsilon_c = \frac{LW_{t,c}^{up}}{LW_s^{up}} \tag{2.3}$$

where $SW_{t,c}^{up}$ is the upward clear sky shortwave flux, and $LW_{t,c}^{up}$ is the upward clear sky longwave flux at the top of the atmosphere. Note that the surface emits longwave radiation depending on the surface temperature, no matter what the cloudiness. The clear sky fluxes in ECHAM5 are computed assuming that there are no clouds; the difference between the albedos / emissivities computed from the clear sky and full sky fluxes thus yields the effect of clouds.

We find that clouds cause a 1 K stronger cooling in PE than in PR (namely 6.5 K compared to 5.5 K, see Figure 2.10). This is due to a larger increase of the planetary albedo in PE compared to PR. The planetary albedo increase due to clouds amounts to 0.159 for PE and only 0.145 for PR. By multiplication with $S_0/4$, this translates into a shortwave cloud radiative forcing (CRF) of $-54.3\,\mathrm{Wm}^{-2}$ in PE compared to $-49.6\,\mathrm{Wm}^{-2}$ in PR. Note that this larger negative shortwave CRF in PE occurs despite a reduced total cloud cover (Table 2.2). Even though the cloud cover is reduced, the shortwave effect of the clouds is larger in PE because the surface is darker. According to the EBM, the PE shortwave CRF causes a cooling of 15.0 or 15.5 K, depending on whether we change the albedo or the emissivity first (black auxiliary lines in Figure 2.10 are only drawn for emissivity decrease first). The pre-industrial shortwave CRF causes

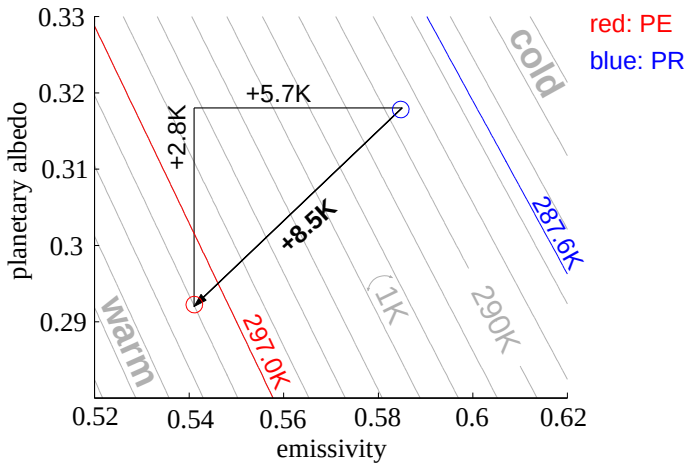

Figure 2.8: Using the EBM to trace back the temperature difference between PE and PR to albedo and emissivity changes in the GCM; grey lines are contour lines of the EBM-predicted temperature for certain emissivities and albedos, contour intervals are 1K; the red and blue lines are the GCM-diagnosed temperatures for PE and PR, respectively; the circles are the surface temperatures predicted by the EBM using the GCM-diagnosed emissivities and albedos; the black arrow indicates the EBM-predicted PE-PR temperature difference; the black lines are auxiliary lines to estimate the albedo and emissivity caused temperature difference separately.

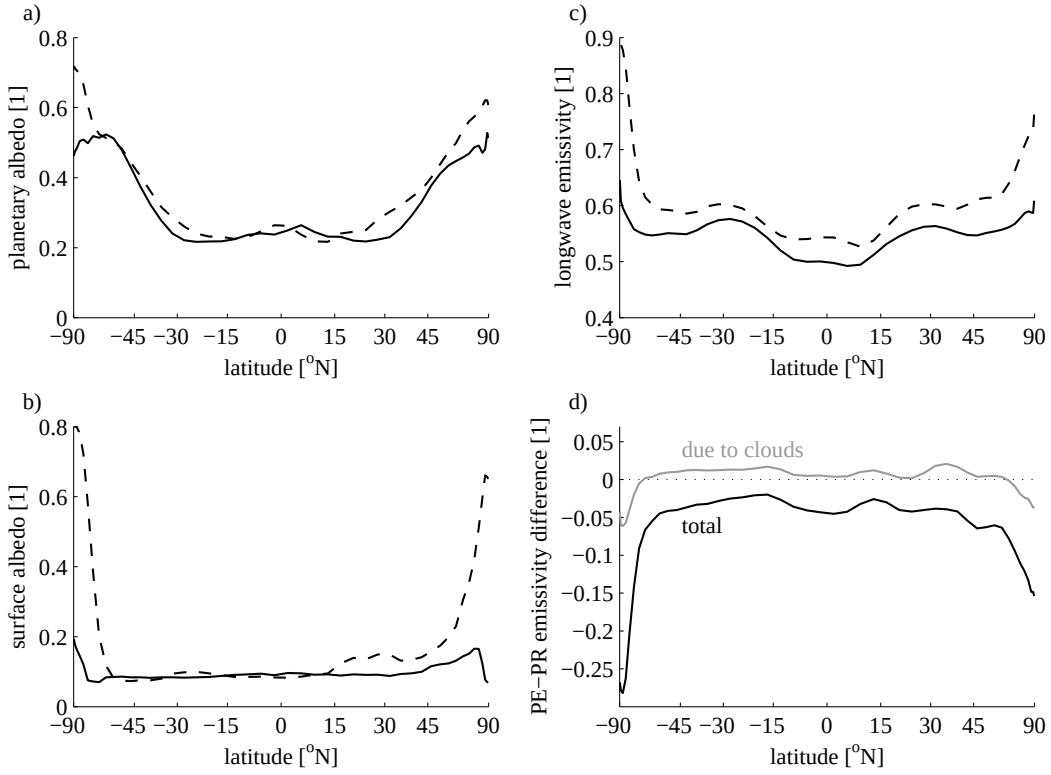

Figure 2.9: (a) Zonal mean planetary albedo, (b) surface albedo, and (c) effective longwave emissivity for PE (solid) and PR (dashed); (d) PE-PR emissivity change (black) and PE-PR emissivity change due to clouds (grey) diagnosed from the difference between the full sky and clear sky emissivities. The horizontal scale is linear in the sine of the latitude.

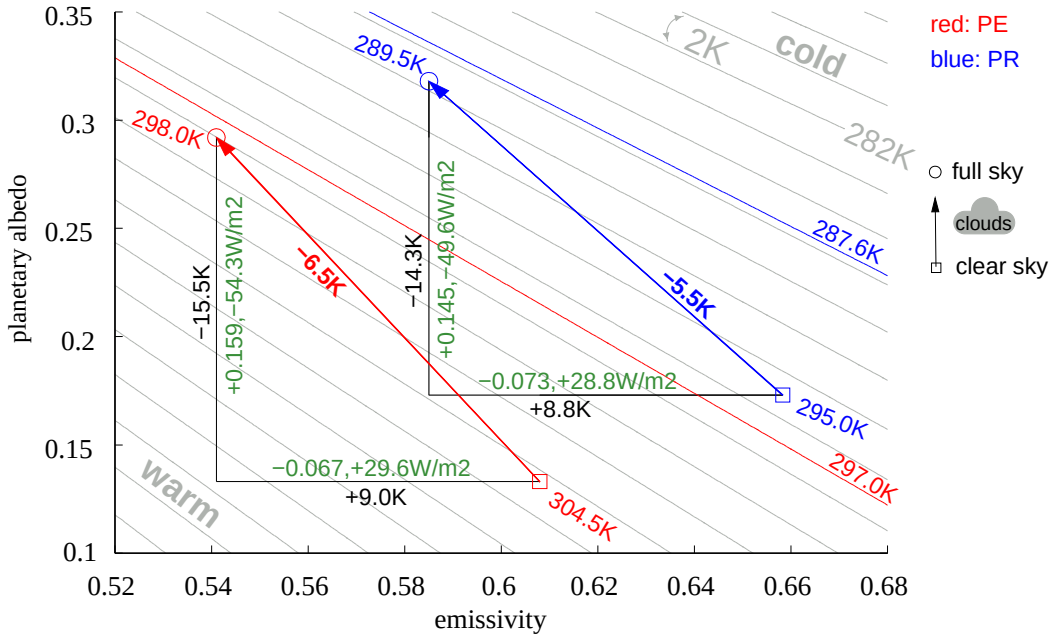

Figure 2.10: Using the EBM to estimate the effect of clouds on the PE-PR temperature difference; grey lines are contour lines of the EBM-predicted temperature, contour intervals are 2K; the red and blue lines are the GCM-diagnosed temperatures for PE and PR, respectively; the circles are the temperatures as computed from the EBM using the GCM-diagnosed *full sky* emissivities and albedos; the squares are EBM temperatures computed for the GCM-diagnosed *clear sky* emissivities and albedos; the red and blue arrows indicate the cooling due to clouds in PE and PR, respectively; the black lines are auxiliary lines to decompose the temperature differences into differences caused by albedo and emissivity; green numbers are emissivity and albedo changes due to clouds and the according cloud radiative forcing.

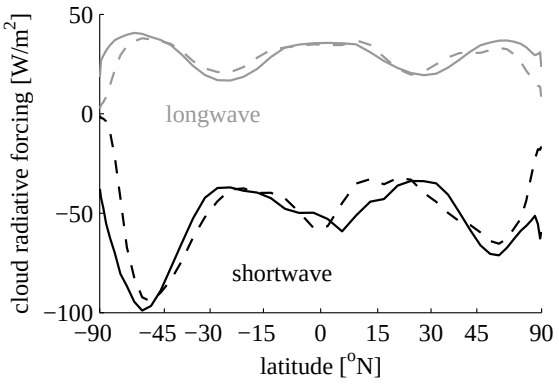

Figure 2.11: Zonal mean longwave (grey) and shortwave (black) cloud radiative forcing as diagnosed from PE (solid), and PR (dashed). The horizontal scale is linear in the sine of the latitude.

a cooling of 13.9 or 14.3 K. The difference of 0.7 to 1.6 K is reduced by about 0.2 K due to a larger positive longwave CRF for PE (29.6 Wm^{-2} compared to 28.8 Wm^{-2}). This larger longwave CRF in PE occurs despite a smaller emissivity change, because the absolute amount of longwave radiation emitted from the surface is much larger (445 Wm^{-2} compared to 395 Wm^{-2}, Table 2.2).

Note that the global mean PE-PR emissivity difference due to cloud cover changes is small only because the reduced emissivity due to clouds at high latitudes is over-compensated by an increased low latitude emissivity (grey lines in Figures 2.9c and 2.11). Thus, cloud changes via absorption of longwave radiation cause a high-latitude amplification of the PE-PR temperature difference. On the other hand, clouds via the reflection of shortwave radiation diminish the high-latitude amplification due to surface albedo changes (Figure 2.9a compared to b, and Figure 2.11).

2.4.3 Topographic changes

Some of the regional PE-PR surface temperature differences are caused by topographic height changes. To estimate this effect, we compare the PE-PR surface temperature difference to the potential temperature difference. We compute the potential temperatures at the global mean surface pressure, assuming a dry adiabatic lapse rate of 9.8 $\mathrm{K(km)}^{-1}$. We find the largest topographic effects in Antarctica, where the lower PE orography accounts for a zonal mean surface warming of up to 15 K, and in the present-day Himalaya, where it accounts for a surface warming of about 3 K (compare solid black to grey line in Figure 2.5b). The global mean spectrally averaged surface height in PE is about 90 m lower than in PR (Table 2.2). The global mean PE and PR

potential temperatures at the respective mean sea level pressures differ by 0.9 K less than the global mean surface temperatures. However, since the global mean surface pressure in ECHAM5 is prescribed at 985.5 hPa (the atmosphere does not change its mass; see Trenberth and Smith 2005), the variation of the global mean surface height does not influence the global mean surface temperature.

2.4.4 Greenhouse gas forcing

As we have seen in Section 2.4.2, clouds only slightly affect the global mean PE-PR emissivity difference. The non-CO_2 well-mixed greenhouse gases in the PE simulation are kept at pre-industrial levels (Table 2.1). Hence the lower emissivity in the PE simulation should be due to the doubled CO_2 concentration and an increased atmospheric water vapour content. A doubled CO_2 concentration yields an additional radiative forcing of 3.7 Wm^{-2} (e.g., Forster et al. 2007). The temperature change due to this additional radiative forcing can be computed from

$$\frac{S_0}{4}(1-\alpha) + 3.7\mathrm{Wm}^{-2} \equiv \epsilon\sigma\tau'^4_{s,ebm}$$

which defines the changed surface temperature $\tau'_{s,ebm}$, and results in

$$\tau'_{s,ebm} - \tau_{s,ebm} \approx 1.1\,\mathrm{K}. \tag{2.4}$$

The globally averaged, vertically integrated atmospheric water vapour content has almost doubled in PE compared to PR (Table 2.2). Note the large relative changes of the water vapour content at high latitudes (Figure 2.12). Unfortunately, we cannot diagnose the radiative forcing of this water vapour increase directly from our GCM setup; however, we can compute the water vapour effect as a residual. The total PE-PR surface temperature difference due to emissivity changes amounts to +5.7 K (Section 2.4.1). The stronger positive longwave CRF in PE only yields about +0.2 K (Section 2.4.2). Doubled pCO_2 yields +1.1 K. The residual, which we ascribe to the larger PE atmospheric water vapour content, amounts to +4.4 K.

2.4.5 Orbital forcing

The choice of the orbital parameters as described in Section 2.2 leads to the following changes in PE, compared to PR: less incoming shortwave radiation in the northern hemisphere in May, June, and July; less incoming radiation in the Arctic spring and autumn; and more radiation mostly during December and January in low and mid latitudes (Figure 2.13b). Integrated over the annual cycle, this amounts to about 0.3 Wm^{-2} more incoming shortwave radiation at low and middle latitudes in PE, and about 1 Wm^{-2} less incoming shortwave radiation at high latitudes (Figure 2.13a). This

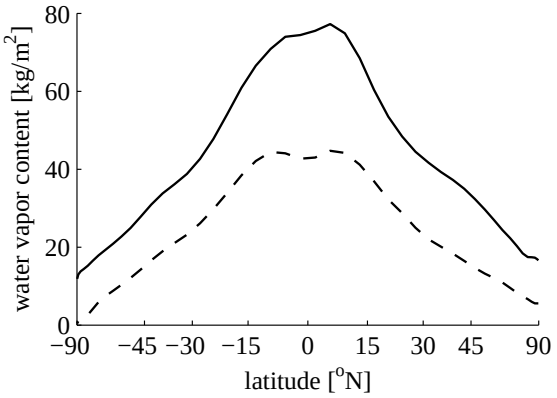

Figure 2.12: Zonal mean vertically integrated water vapour in the PE simulation (solid) compared to the pre-industrial simulation (dashed). The horizontal scale is linear in the sine of the latitude.

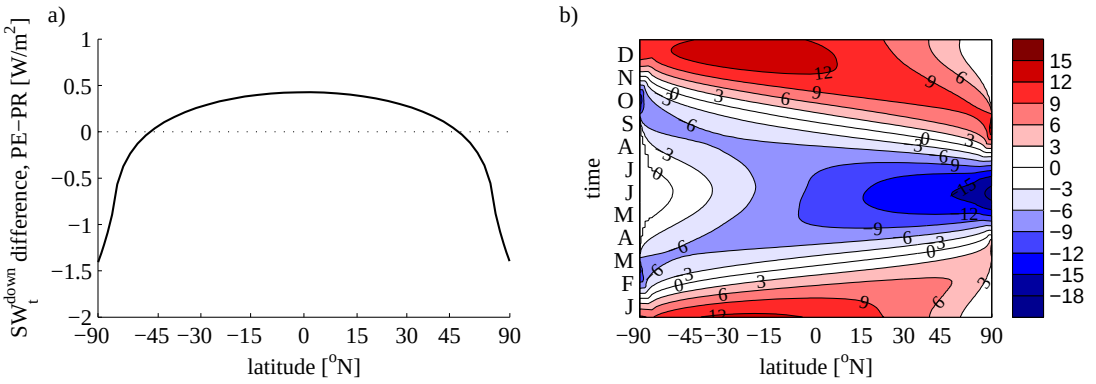

Figure 2.13: (a) Annual mean and (b) seasonal cycle of the difference of the zonal mean incoming shortwave radiation at the top of the atmosphere between PE and PR; red indicates more incoming radiation in the PE simulation. Contour intervals are 3 Wm^{-2}. The horizontal scale is linear in the sine of the latitude.

redistribution of the incoming shortwave radiation at the top of the atmosphere, from high latitudes to low latitudes, is due to the reduced obliquity in PE (Figure 2.2).

As mentioned in Section 2.2, the orbital parameters obliquity, eccentricity, and longitude of perihelion vary on timescales that are short compared to the length of the PE period. Changes of these parameters do not lead to a change of the global mean incoming shortwave radiation and thus should not, in the first approximation, affect the global mean temperature. However, other results might change; for example, choosing a larger obliquity in our PE setup would have caused a smaller pole-to-equator temperature gradient.

From the theory of stellar evolution, it is known that the Sun has gradually brightened by more than 30 % since it settled down to steady nuclear burning of hydrogen roughly 4.5 billion years ago (e.g., Endal and Sofia 1981; Peltier 2003). Due to this brightening, the total solar irradiance 55 million years ago was up to 0.6 % (about $8\,\mathrm{Wm}^{-2}$) smaller than at present. According to the EBM (2.1), and given the PE albedos and emissivities, the temperature change due to such a reduction of the radiative forcing would amount to less than $-0.5\,\mathrm{K}$.

2.5 Discussion and conclusions

Using the coupled atmosphere-ocean-sea ice general circulation model ECHAM5/MPI-OM, we perform a long, stable climate simulation for the late Paleocene to early Eocene (PE). The simulated PE Earth surface is on average 297 K warm and ice-free. To our knowledge, we have obtained the first coupled PE simulation with moderate GHG forcing that is warm enough at high latitudes to keep the poles free from sea ice, while reasonably matching the lower latitude SST reconstructions. However, if we take the SST proxy data by Sluijs et al. (2006) at face value, the simulated Arctic surface temperature is still too cold.

A possible shortcoming of this study is the assumption of a globally homogeneous vegetation. Including a more realistic vegetation distribution such as the one reconstructed by Utescher and Mosbrugger (2007) may, at least regionally, affect the climate (Sewall et al. 2000). Also, we did not include lakes in our PE model setup. Including lakes (e.g., the North American Green River lake system) could lead to a further reduction of the seasonality in the continental interiors (Sloan 1994).

We find that the *total* atmospheric heat transports in PE and the pre-industrial reference (PR) are very similar, although the latent heat fraction is larger in PE than in PR. The total poleward heat transport by the ocean is smaller in PE compared to PR. We conclude that, looking at zonal averages, the meridional heat transports do not contribute to the more equable PE climate in our simulation (confirming the results of Huber and Sloan 2001). The influence of the ocean circulation on the PE climate will be discussed in more detail in Chapter 4.

Compared to PR, the simulated PE Earth surface is on average 9.4 K warmer. While low latitudes in PE are on average about 5 to 8 K warmer, northern high latitudes are warmer by up to 20 K, and southern high latitudes are warmer by up to 40 K. As a diagnostic tool to roughly understand this temperature difference, we fit a zero-dimensional energy balance model (EBM) to the PE and PR GCM solutions.

According to the EBM, one third of the PE-PR surface temperature difference is due to a reduced planetary albedo. The surface albedo in PE compared to PR is reduced mostly due to the lack of glaciers, the lack of sea ice, and reduced snowfall. However, this large high-latitude surface albedo change is partly compensated by a more negative shortwave cloud radiative forcing. In that sense, clouds in our PE model work against the high-latitude amplification of the snow and ice albedo feedback. Nevertheless, the planetary albedo reduction is largest at high latitudes.

Two thirds of the warming are due to a reduction of the effective longwave emissivity. We find that clouds cause a significant reduction of the effective longwave emissivity at high latitudes. This reduction of the emissivity at high latitudes is overcompensated by an increase of the emissivity due to clouds at lower latitudes. This way —via their effect on the longwave emissivity—, clouds in PE compared to PR hardly affect the global mean temperature, but they cause a polar warming and a tropical cooling.

The doubled atmospheric pCO_2 directly causes a warming of about 1 K. We ascribe the residual of the emissivity-induced PE-PR temperature difference, which amounts to more than 4 K, to the water vapour feedback. The emissivity change due to the combination of the doubled pCO_2 and the water vapour feedback is also largest at high latitudes, and thus leads to a high-latitude amplification.

The reduced orographic height in the PE setup should not affect the global mean temperature, but it does have large regional effects. Up to 15 K of the southern high-latitude PE-PR surface temperature difference is due to the lower Antarctic surface height in PE.

As a consequence of the reduced obliquity in our PE setup, a small amount of incoming shortwave radiation at the top of the atmosphere is redistributed from high latitudes to low latitudes. The resulting annual mean reduction of the radiative forcing by about $1\,\mathrm{Wm}^{-2}$ at high latitudes should only slightly increase the pole-to-equator temperature gradient in the PE simulation. Note that, for comparison, the cloud-induced emissivity reduction at high latitudes yields an additional, annual mean CRF of up to $20\,\mathrm{Wm}^{-2}$.

Summing up, the equable PE climate as simulated in ECHAM5/MPI-OM is due to topographic effects, due to surface albedo changes, and most importantly due to a reduction of the effective longwave emissivity that is largest at high latitudes.

Chapter 3

Sensitive PE climate

3.1 Sensitivity to atmospheric carbon dioxide

3.1.1 Introduction

In this section, we investigate the sensitivity of the simulated PE climate to a variation of the atmospheric carbon dioxide concentration (pCO_2). We do this for two reasons. First, estimates for the atmospheric pCO_2 before the PETM range from 300 ppm (Royer et al. 2001) to more than 2000 ppm (Pearson and Palmer 2000). For the PE control simulation as described in the previous chapter, we use an atmospheric pCO_2 of 560 ppm. To assess the sensitivity of the PE model solution to the uncertain GHG forcing, we investigate the climate response to decreased and increased atmospheric pCO_2. Second, the PETM is associated with an increase of atmospheric pCO_2. However, neither the source nor the magnitude of the CO_2 input are certain. We compare the pCO_2 sensitivity runs, especially the pCO_2 increase experiments, to the reconstructed warming at the beginning of the PETM.

Proxy data indicate that the Earth's surface at the start of the PETM warmed by 3 to 9 K in less than 10,000 years (Thomas et al. 2002; Zachos et al. 2003; Tripati and Elderfield 2004; Sluijs et al. 2006; Zachos et al. 2006). This on geological timescales relatively abrupt warming was followed by a more gradual cooling that lasted about 200,000 years (Röhl et al. 2000).

The surface warming was associated with a large input of light carbon (C) to the atmosphere-ocean system (light meaning a low $^{13}C/^{12}C$ isotopic ratio). The magnitude of this light carbon input is measured in terms of $\delta^{13}C$, which expresses the $^{13}C/^{12}C$ ratio of a sample, for example of carbon from calcite shells of marine plankton that sedimented during the PE, relative to the standard of the Vienna Pee Dee Belemnite fossil (V-PDB) or the Vienna Standard Mean Ocean Water (V-SMOW)

$$\delta^{13}C = \frac{^{13}C/^{12}C_{sample} - ^{13}C/^{12}C_{standard}}{^{13}C/^{12}C_{standard}}. \tag{3.1}$$

The size of the $\delta^{13}C$ carbon isotope excursion during the PETM was probably about -2.5‰ (for an overview on $\delta^{13}C$ changes during the last 65 Ma see Zachos et al. 2001;

Bowen et al. 2004; Pagani et al. 2006a,b; Handley et al. 2008). Zachos et al. (2005) presented geochemical data indicating a rapid acidification of the ocean during the PETM, and a shoaling of the ocean's carbonate compensation depth within less than 10,000 years. Both the acidification and the carbon isotopic excursion support the notion that elevated atmospheric pCO_2 drove the PETM. Yet, the source of the CO_2 remains a mystery (Pagani et al. 2006a).

Dickens et al. (1995) suggested that an increase in bottom water temperature could have led to a change in sediment thermal gradients, dissociation of large quantities of oceanic hydrate, and release of methane to the ocean-atmosphere inorganic carbon reservoir. The amount of methane needed to explain the large carbon isotope excursion is relatively small, because the carbon from bacterially produced methane has a very low average δ^{13}C of -60‰ (Kvenvolden 1993). Note that methane, once it is released to the oxic, sunlit atmosphere, oxidises to form CO_2 on a timescale of about a decade (Brasseur and Solomon 1986; Archer 2007).

Given the source of the carbon (i.e., given its δ^{13}C), the magnitude of the carbon isotopic excursion plus the proxy-derived warming at the PETM can be used to constrain the PE equilibrium climate sensitivity. The equilibrium climate sensitivity is defined as the global annual mean surface air temperature change experienced by the climate system after it has attained a new equilibrium in response to a doubling of atmospheric pCO_2 (Randall et al. 2007). Assuming methane as the primary driver of the PETM, Pagani et al. (2006a) computed that an equilibrium climate sensitivity of 6.8 to 7.8 K would be necessary to explain the warming.

The acidification and associated rise of the carbonate compensation depth indicate that the size of the carbon addition was larger than can be accounted for by the methane hydrate hypothesis (Zachos et al. 2005; Higgins and Schrag 2006). Panchuk et al. (2008) used an intermediate complexity Earth system model to investigate the sedimentary response to different PETM carbon release scenarios. They found that 6800 Pg C (δ^{13}C of -22‰) was the smallest pulse to reasonably reproduce observations of the extent of seafloor $CaCO_3$ dissolution. If 6800 Pg C is the lower bound on pulse size, then the upper bound on climate sensitivity is reduced to about 4 K (second Figure in Pagani et al. 2006a; Panchuk et al. 2008).

Previous PE modelling studies do not support large climate sensitivities. For example, Shellito et al. (2003) found a climate sensitivity of about 2 K using a slab ocean version of the NCAR Climate System Model CSM. Recently, Winguth et al. (submitted) confirmed this low climate sensitivity using a PE version of the fully coupled NCAR atmosphere-ocean model CCSM3.

The low CCSM PE climate sensitivity is in line with the relatively low transient response of 1.5 K, and the low long-term sensitivity of 2.7 K of the CCSM contemporary climate (Randall et al. 2007). For comparison, the transient response and long-term sensitivity of the ECHAM5/MPI-OM contemporary climate amount to 2.2 K and 3.4 K,

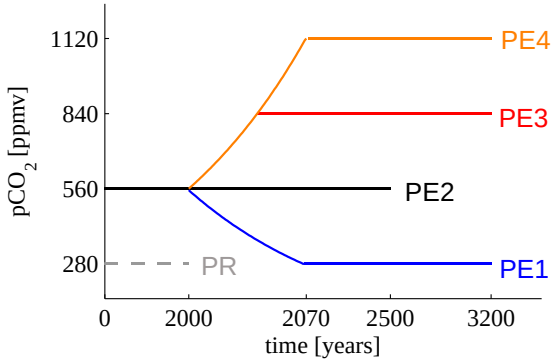

Figure 3.1: Experimental setup of the atmospheric carbon dioxide sensitivity experiments. Solid lines show the atmospheric carbon dioxide concentrations in the PE simulations. We refer to the PE simulations with onefold, twofold, threefold, and fourfold pre-industrial carbon dioxide concentrations as PE1 (blue), PE2 (black), PE3 (red), and PE4 (orange) respectively. The dashed grey line indicates the pre-industrial reference.

respectively. Note that the contemporary, long-term climate sensitivities were derived from simulations using the full atmosphere GCMs coupled to slab oceans, not to the full ocean GCMs. We investigate the PE climate sensitivity using the fully-coupled atmosphere-ocean-sea ice GCM ECHAM5/MPI-OM.

This section is organised as follows. In Section 3.1.2, we present the experimental setup of the CO_2 sensitivity runs. In Section 3.1.3, we describe the climate response to the pCO_2 variation. In Section 3.1.4, we compare the simulated surface temperature change to the reconstructed SST increase during the PETM. In Section 3.1.5, we study the mechanisms that lead to the surface temperature changes using a zero-dimensional EBM. In Section 3.1.6, we briefly describe meridional heat transport changes. In Section 3.1.7, we focus on the Arctic climate change in response to the pCO_2 variation. Section 3.1.8 presents a discussion of the results and conclusions.

3.1.2 Experimental setup

Using the PE version of ECHAM5/MPI-OM, we perform the following pCO_2 sensitivity runs. Starting in year 2000 of our PE control simulation, we decrease the atmospheric pCO_2 by one percent per year until stabilising in year 2069 at the pre-industrial pCO_2 of 280 ppm, and we increase pCO_2 by one percent per year until stabilising at 840 ppm in year 2041, and 1120 ppm in year 2070 (Figure 3.1). We refer to these PE simulations with onefold, twofold, threefold, and fourfold pre-industrial pCO_2 as PE1, PE2, PE3, and PE4, respectively.

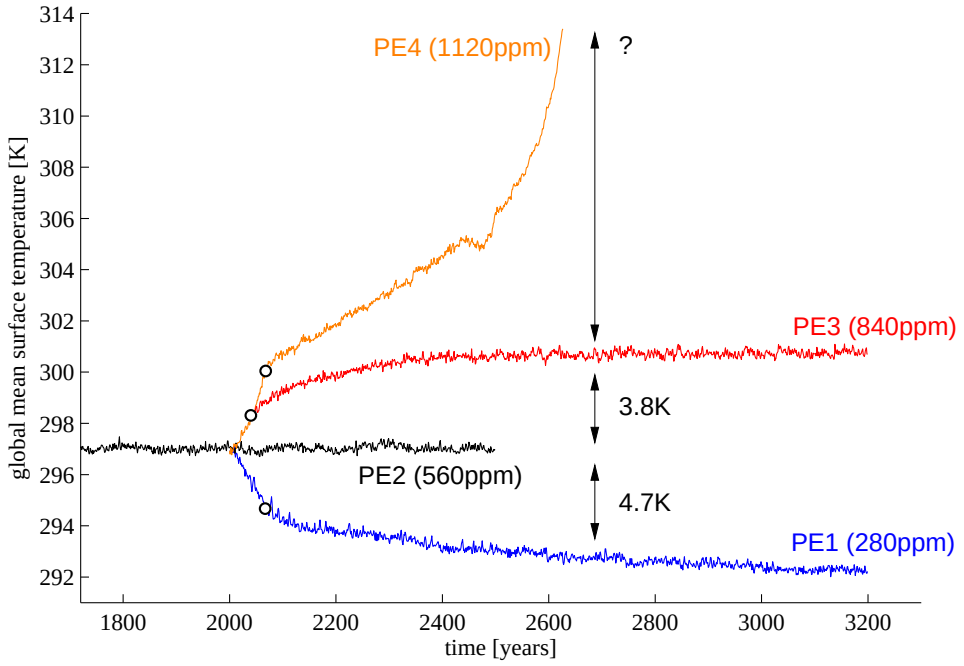

Figure 3.2: Time series of the global mean surface temperatures for the Paleocene-Eocene pCO_2 sensitivity experiments PE1 (blue; pCO_2-decrease to 280 ppm), PE2 (black; control simulation with pCO_2 of 560 ppm), PE3 (red; pCO_2-increase to 840 ppm), and PE4 (orange; pCO_2-increase to 1120 ppm). The indicated temperature differences are based on the last 200 years of PE1, PE2, and PE3. The black circles show the points at which the pCO_2 concentrations are stabilised.

For the pCO_2 increase experiments we modify ECHAM5 in two ways. First, to maintain numerical stability of ECHAM5 at high surface temperatures, we ensure positive definite optical thicknesses in the longwave radiative transport model. We describe the details of this modification in Section 3.2. Second, we adapt the prescribed ozone climatology to increased tropopause heights. This adaptation of the ozone climatology is necessary to avoid artificial warming in response to too high ozone concentrations in the upper troposphere. The details of this ozone adaptation, and the sensitivity of our PE simulations with respect to this ozone adaptation are discussed in Section 3.3.

3.1.3 Surface temperature response

The pCO_2 decrease from 560 to 280 ppm in PE1 leads to a drop of the equilibrium surface temperature by more than 4.7 K (Figure 3.2). Note that the global mean surface temperature at the end of PE1 is still about 4.7 K warmer than in PR, although PE1

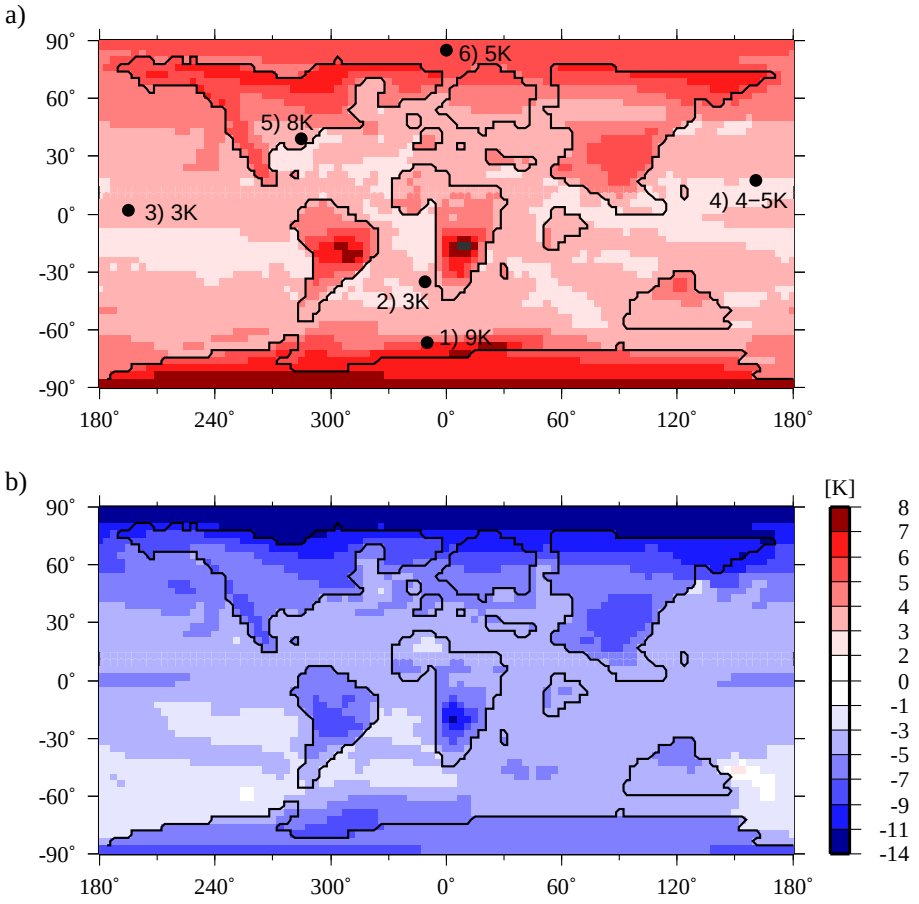

Figure 3.3: (a) PE3-PE2 surface temperature difference; black dots indicate the paleo-locations for temperature reconstructions by 1) Thomas et al. (2002, based on δ^{18}O), 2) and 3) Tripati and Elderfield (2004, based on Mg/Ca ratios assuming the Mg/Ca ratio of seawater to be 5.15 mmol/mol), 4) Zachos et al. (2003, based on TEX_{86}), 5) Zachos et al. (2006, based on TEX_{86}), and 6) Sluijs et al. (2006, based on TEX_{86}); the numbers indicate the reconstructed SST increase during the PETM. (b) PE1-PE2 surface temperature difference.

and PR basically have the same prescribed greenhouse gas forcing (Table 3.1). This means that the PE-PR boundary condition differences other than greenhouse gases yield a global mean surface temperature difference of about +4.7 K, which is half of the PE-PR surface temperature difference of 9.4 K as described in Chapter 2. These 4.7 K also include the switched-off SSO parameterisation and ENSO-tuning, and the constant instead of dynamic orbital parameters, which in combination with the internal feedback mechanisms cause a warming of about 0.8 K in the pre-industrial simulation (Section 2.2.4).

Increasing pCO_2 to 840 ppm causes a warming of about 3.8 K. This warming due to the 1.5 fold pCO_2 increase, assuming a logarithmic increase of the surface temperature with pCO_2, translates into an equilibrium climate sensitivity of

$$\frac{3.8\,K}{log_2(1.5)} = 6.5\,K. \tag{3.2}$$

Note that we compute the climate sensitivities from the *surface* temperatures; if we used the 2 m air temperatures, we would even get slightly larger climate sensitivities (Table 3.1). This PE climate sensitivity is almost twice as large as the ECHAM5/MPI-OM equilibrium climate sensitivity computed for the contemporary climate using a slab ocean model. It is more than three times as large as the PE climate sensitivity reported by Shellito et al. (2003) and Winguth et al. (submitted). We will attempt to isolate the mechanisms that lead to this large climate sensitivity in Section 3.1.5.

Increasing pCO_2 to 1120 ppm leads to a runaway effect. After the stabilisation of the atmospheric pCO_2, the global mean surface temperature keeps rising until numerical problems occur in year 2629 at a global mean surface temperature of more than 313 K. Note that the global mean surface temperature exhibits a transient drop around the year 2444. We will explain this drop in Chapter 4. Note that the results of the pCO_2 increase experiments depend on the tropospheric ozone parameterisation, which will be discussed in Section 3.3.

3.1.4 Comparison to reconstructed PETM warming

Sea surface temperature reconstructions suggest that the Arctic had been warm and sea ice free already before the PETM (Chapter 2, Figure 2.5a, Sluijs et al. 2006). In PE1, the Arctic surface cools down by more than 11 K to less than 270 K, and is seasonally sea ice covered. This Arctic climate change will be discussed in more detail in Section 3.1.7. Overall, PE1 is too cold at high latitudes to appropriately represent the PE climate. Note feedback mechanisms associated with the formation of sea ice were probably not at work during the PETM. We should compare the warming during the PETM to the warming during PE3 rather than to the PE2-PE1 temperature differences.

According to Zachos et al. (2003) and Tripati and Elderfield (2004), the low and mid latitudes warmed by 3 to 5 K during the PETM (Figures 3.3a and 3.4b). According to

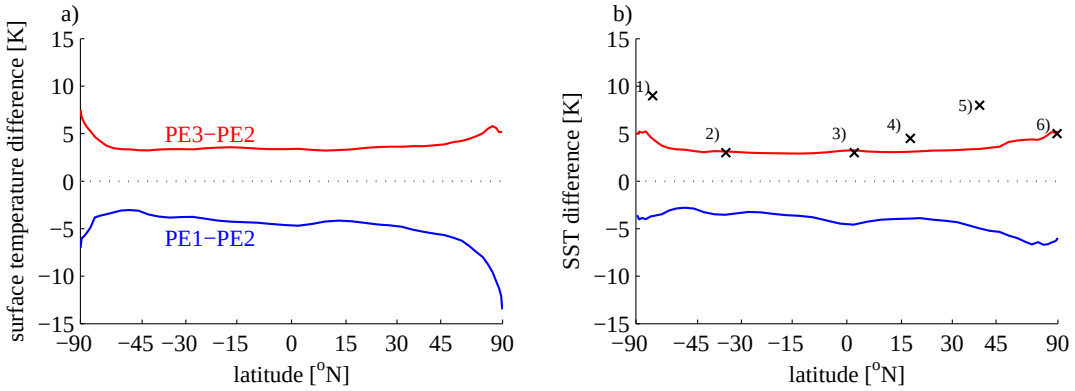

Figure 3.4: (a) Zonal mean surface temperature difference for PE3 (red), and PE1 (blue) compared to PE2; (b) zonal mean sea surface temperature (SST) difference for PE3 (red), and PE1 (blue) compared to PE2; crosses indicate differences between SST estimates from proxy data during and before the PETM; proxy data sources: 1) Thomas et al. (2002), 2) and 3) Tripati and Elderfield (2004), 4) Zachos et al. (2003), 5) Zachos et al. (2006), 6) Sluijs et al. (2006). The horizontal scale is linear in the sine of the latitude.

Sluijs et al. (2006), Arctic SSTs warmed by about 5 K. The SST increase in PE3 more or less matches these reconstructed SST increases. According to Thomas et al. (2002), the SST in the proto-Weddell Sea increased by as much as 9 K. While the zonal mean SST increase in PE3 in the Southern Ocean amounts to less than 5 K (Figure 3.4b), locally, we do find a temperature increase of more than 7 K relatively close to the proto-Weddell Sea (Figure 3.3a). We will attempt to explain this large zonal difference in Chapter 4. However, the relatively small warming of about 3 K at the paleo-location of Wilson Lake (New Jersey) in PE3 does not at all match the reconstructed SST increase of 8 K by Zachos et al. (2006).

3.1.5 Analysis of climate response and comparison to EBM

Decreasing pCO_2 in PE1 leads to an increase of the planetary albedo by 0.012 (Table 3.1); the atmosphere reflects more shortwave radiation, which leads to a cooler climate. At the same time, the effective longwave emissivity in PE1 increases by 0.027; a larger fraction of the longwave radiation emitted by the surface leaves the top of the atmosphere, which also leads to a cooler climate. The emissivity increase and the albedo increase are largest at high latitudes (Figure 3.5a-b). Increasing pCO_2 leads to the reverse effects, a reduction of the planetary albedo by 0.013 and a reduction of the effective longwave emissivity by 0.016, which both lead to a warmer climate. The

planetary albedo reduction due to the pCO_2 increase in PE3 does not show a very clear latitudinal structure; the largest reduction occurs over the Antarctic continent. The emissivity reduction during PE3 is largest at high latitudes. Thus, most of the relatively small high-latitude amplification of the warming during PE3 in response to the pCO_2 increase should be due to the high-latitude amplification of the emissivity reduction.

To quantify the different contributions of the albedo and effective emissivity changes to the global mean surface temperature changes in PE1, PE3, and PE4, we fit a zero-dimensional EBM to the GCM output. The EBM is described in Section 2.4.1.

For the well equilibrated runs PE1, PE2, and PE3, the EBM-derived global mean surface temperatures τ_s^{ebm} are 0.8 to 1.0 K higher than the GCM-diagnosed surface temperatures τ_s (Table 3.1, Figure 3.6). The EBM, fed with the GCM albedo and effective emissivity responses to the pCO_2 decrease in PE1, predicts a global mean cooling of 4.8 K, which is very close to the GCM-predicted cooling of 4.7 K. According to the EBM, the GCM-predicted increase of the effective emissivity causes about 3.6 K of the cooling. Only about 1.2 K of the cooling are due to the increased planetary albedo. For the pCO_2 increase from 560 to 840 ppm, the EBM predicts a warming of 3.6 K, which is also close to the GCM-predicted warming of 3.8 K. Here, according to the EBM, the emissivity reduction causes about 2.3 K of the warming. The remaining warming of 1.3 K is due to a decreased planetary albedo.

To constrain the effects that lead to the runaway climate, we also apply the EBM to the average of the years 2430 to 2439 of PE4. We refer to this transient time interval as PE4T. The EBM-predicted temperature for PE4T is 1.4 K higher than the GCM-diagnosed temperature. The EBM, fed with the GCM albedo and effective emissivity decreases from PE3 to PE4T, predicts a global mean surface temperature increase by 4.9 K. The GCM-diagnosed temperature increase amounts to only 4.3 K. This mismatch of 0.6 K occurs because we apply an energy *balance* model to the unbalanced, transient climate state PE4T. In the GCM, the surface temperature response lags the emissivity and planetary albedo changes. At the Earth's surface, shortwave radiative fluxes, longwave radiative fluxes, sensible heat fluxes, latent heat fluxes, and conductive heat fluxes through sea ice should be balanced on a temporal mean if the ocean is in a quasi-steady state. For PE4T, the global mean heatflux imbalance at the surface amounts to $+2\,Wm^{-2}$ (Table 3.1), indicating that the ocean still absorbs a significant amount of heat. For PE1, PE2, and PE3 the global mean oceanic heat uptake amounts to less than $1\,Wm^{-2}$.

Surprisingly, for PE1, the heat flux imbalances at the top of the atmosphere and at the surface amount to +0.9 and $+0.1\,Wm^{-2}$, respectively, even though the global mean surface temperature shows a small cooling trend during the last 200 years of the simulation (Figure 3.2). Theoretically, the difference between the imbalance at the top of the atmosphere and the imbalance at the surface, which amounts to $+0.8\,Wm^{-2}$,

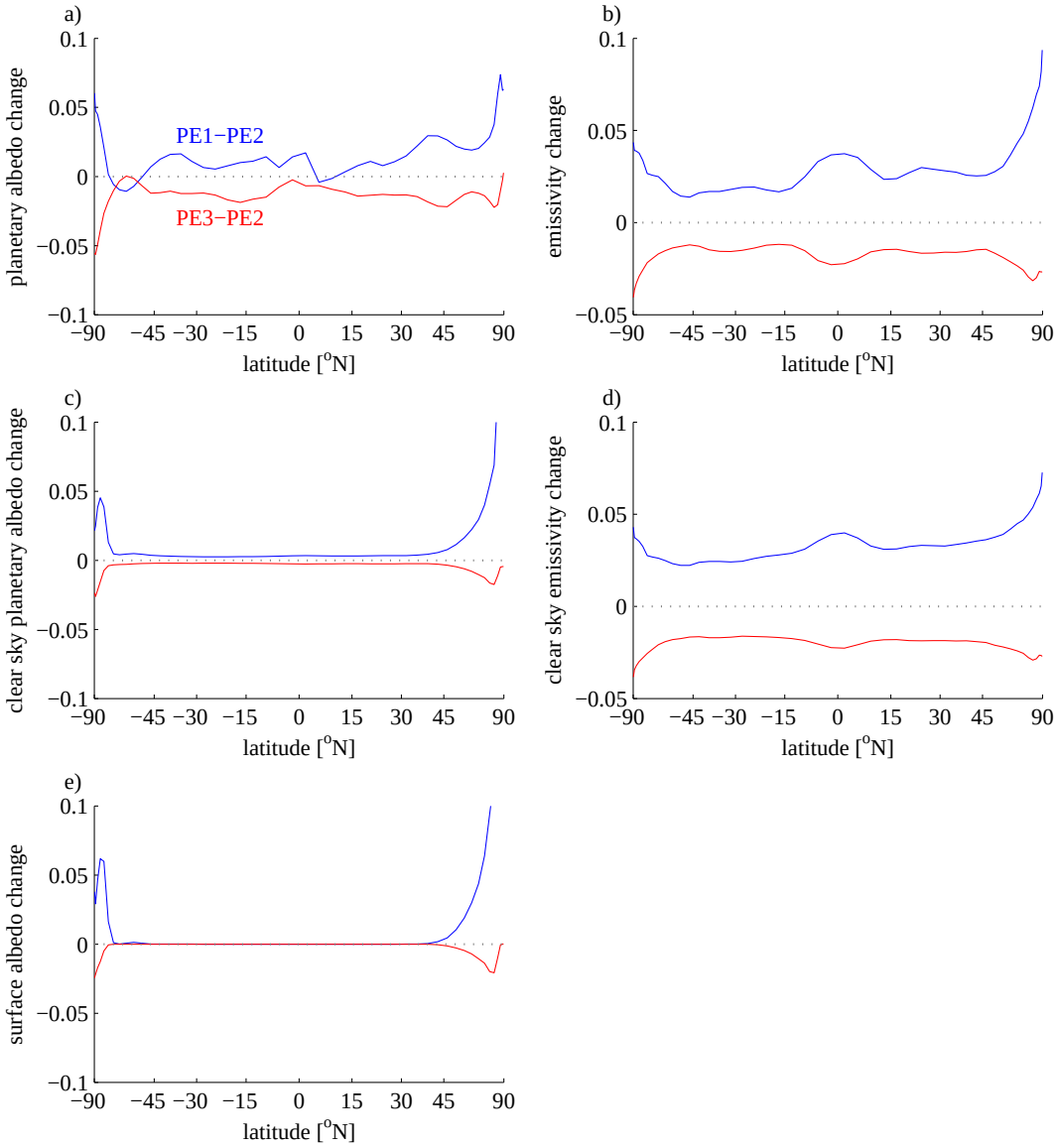

Figure 3.5: Zonal mean differences between PE3 and PE2 (red), and PE1 and PE2 (blue) of (a) the planetary albedo, (b) the effective longwave emissivity, (c) the planetary albedo computed from the clear sky radiative fluxes, (d) the longwave emissivity computed from the clear sky radiative fluxes, and (e) the surface albedo. The horizontal scale is linear in the sine of the latitude.

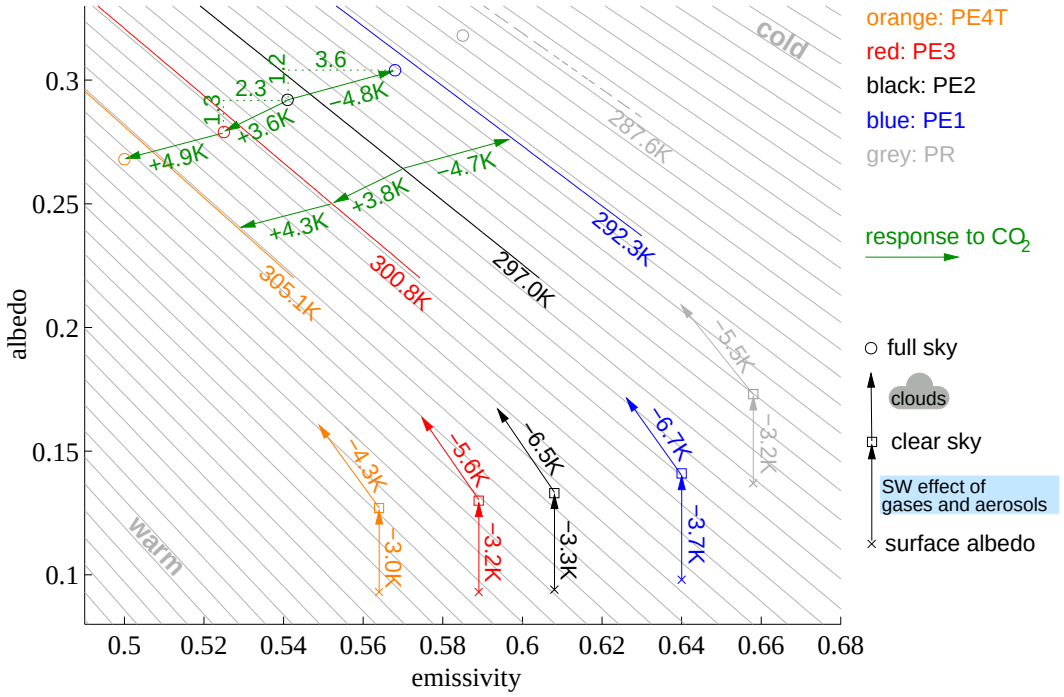

Figure 3.6: Climate response to the variation of atmospheric pCO_2 decomposed using the zero-dimensional EBM 2.1. The grey isolines show the EBM surface temperature as a function of the global mean albedo and emissivity. Isoline intervals are 1 K. The blue (PE1), black (PE2), red (PE3), and orange (PE4T) lines indicate the global mean surface temperature τ_s as diagnosed from the respective GCM runs. Note that, while the diagnoses for PE1 to PE3 are based on the last 200 years of the equilibrated runs, the diagnosis for PE4T (T for transient) is based on the years 2430 to 2439 of the *not* equilibrated run PE4. To decompose the surface temperature response into albedo- and emissivity-driven parts, we compute the global mean surface temperatures using the GCM-diagnosed planetary albedo α and effective emissivity ϵ (circles), the clear sky planetary albedo α_c and clear sky effective emissivity ϵ_c (squares), and the surface albedo α_s and clear sky effective emissivity ϵ_c (crosses). Thus, the differences between the circles and squares are due to clouds, the differences between the squares and crosses are due to effects of the clear sky atmosphere on the shortwave radiation, i.e., absorption and scattering. Pre-industrial reference values are shown in grey (based on the last 200 years of PR).

should lead to a warming of the atmosphere. We do not see the atmosphere warm in PE1. Similar top of atmosphere - surface heatflux imbalances occur for the other simulations. According to Roeckner (personal communication), relatively small mismatches of less than $1\,\mathrm{Wm}^{-2}$ are an acceptable numerical artefact of ECHAM5.

To differentiate between effects of the surface albedo, effects of the clear sky atmosphere, and effects of clouds, we compute (1) the clear sky effective longwave emissivities and clear sky planetary albedos, and (2) the surface albedos from the GCM. The EBM, fed with the clear sky emissivities and albedos, yields the global mean surface temperatures for the different climates under the assumption of instantaneously removed clouds (squares in Figure 3.6). The difference between the temperatures derived from the clear sky planetary albedo and the surface albedo, respectively, reflects the effects of the clear sky atmosphere on the shortwave radiation (difference between squares and crosses in Figure 3.6). In ECHAM5, these effects are Rayleigh scattering and absorption of shortwave radiation by aerosols, CO_2, water vapour, ozone, methane, and nitrous oxide.

The cooling effect of clouds amounts to 6.5 K in PE2, and 5.6 K in PE3. This means that clouds lead to a positive feedback of 0.9 K in response to the pCO_2 increase in PE3. Compared to PE2, the total cloud cover in PE3 is decreased by about 2 % (from 57.6 % to 55.7 %). The decreased cloud cover in PE3 leads to a reduced reflection of shortwave radiation, the shortwave cloud radiative effect (CRF) is reduced by $3.2\,\mathrm{Wm}^{-2}$; the reduced reflection leads to a reduced cooling, hence, to a relative warming. Moreover, although the total cloud cover is reduced in PE3 compared to PE2, the clouds have a $0.4\,\mathrm{Wm}^{-2}$ larger longwave CRF (Table 3.1), because the surface temperature and thus the absolute amount of longwave radiation emitted at the surface is larger. Most of the emissivity reduction in PE3 compared to PE2 is due to the effects of the clear sky atmosphere. According to Forster et al. (2007), a pCO_2 doubling yields a radiative forcing of $3.7\,\mathrm{Wm}^{-2}$. Hence, the pCO_2 increase from 560 to 840 ppm leads to a direct radiative forcing of $3.7\,\mathrm{Wm}^{-2} \times \log_2(1.5) \approx 2.2\,\mathrm{Wm}^{-2}$, which causes a warming of about 0.7 K according to our EBM (computation analogue to that in Section 2.4.4). We attribute the residual clear sky emissivity-driven warming of about 1.5 K to the increased water vapour content (Table 3.1).

The cooling effect of clouds in PE1 amounts to 6.7 K. This means that, although the total cloud cover in PE1 is increased by almost 3 % compared to PE2 (Table 3.1), the positive (cooling) feedback of clouds in response to the pCO_2 decrease only amounts to 0.2 K. We now explain why the feedback is so small. The effect of the planetary albedo decrease by 0.013 during PE1 is diminished, because the clear sky planetary albedo also increases by 0.008 (Table 3.1). This increased clear sky planetary albedo in PE1 is due to two effects. First, it is due to stronger reflection of shortwave radiation by the clear sky atmosphere. This effect of the clear sky atmosphere increases the clear sky planetary albedo at all latitudes (difference between Figure 3.5c and e). Second, it

is due to an increased surface albedo at high latitudes. This increased surface albedo is in line with a larger snow and sea ice cover in PE1 (Figure 3.5e, see Arctic climate change in Section 3.1.7). Moreover, the emissivity increase during the cooling in PE1 is reduced due to clouds; clouds in PE1 have a larger longwave CRF than clouds in PE2 (Table 3.1).

During the runaway effect in PE4, the surface albedo does not change (Table 3.1). There is no more snow to be melted. The cooling effect of clouds in PE4T amounts to 4.3 K, which is 1.3 K less than in PE3. The total EBM-predicted warming in PE4T compared to PE3 amounts to 4.9 K. This indicates that a reduction of the total cloud cover (*burned clouds*) in PE4 causes about 1/4 of the runaway. Although the total cloud cover is reduced in PE4T compared to PE3, the longwave CRF is increased by about 1.3 Wm^{-2}. Note that the reduction of the shortwave CRF is about three times as large as this longwave CRF increase (Table 3.1). Most of the runaway is caused by a decreased clear sky emissivity. This decreased clear sky emissivity is in line with a large increase in the vertically integrated water vapour content. According to Forster et al. (2007) and the EBM, the pCO_2 increase from 840 to 1120 ppm directly causes a warming of about 0.4 K. Note that, using our GCM model setup, we cannot distinguish between the radiative effects of the different components of the clear sky atmosphere. In particular, we cannot distinguish between the effect of water vapour and the potentially large effect of ozone (Section 3.3).

3.1.6 Meridional heat transport changes

We find that the total meridional heat transport hardly changes in response to the pCO_2 variation (Figure 3.7a). The maximum northward heat transport occurs around 30° N and amounts to about 5.9 PW for all simulations. The maximum southward heat transport occurs at about 30° S and amounts to 6.6 PW, 6.9 PW, and 7.2 PW for PE1, PE2, and PE3, respectively. The larger latent heat fluxes in the warmer PE climates are widely compensated by changes of the dry static energy transports (Figures 3.7b-d). The reduced atmospheric heat transport in PE1 is partly compensated by an increased meridional heat transport by oceanic gyres, and by the oceanic meridional overturning circulation (Figure 3.7e-g). We will describe the PE ocean circulation, and the ocean circulation changes associated with these heat transports in Chapter 4.

3.1.7 Arctic climate change

The cooling in response to the pCO_2 decrease in PE1 is largest in the Arctic, where the annual mean surface temperature decreases by as much as 11 K (Figures 3.3b and 3.4a). This cooling is largest during the Northern Hemisphere winter (Figure 3.8a), and is associated with the development of Arctic sea ice (Figure 3.8b). While the Arctic in PE2 is sea ice free, the Arctic in PE1 is seasonally ice covered. Sea ice starts growing in

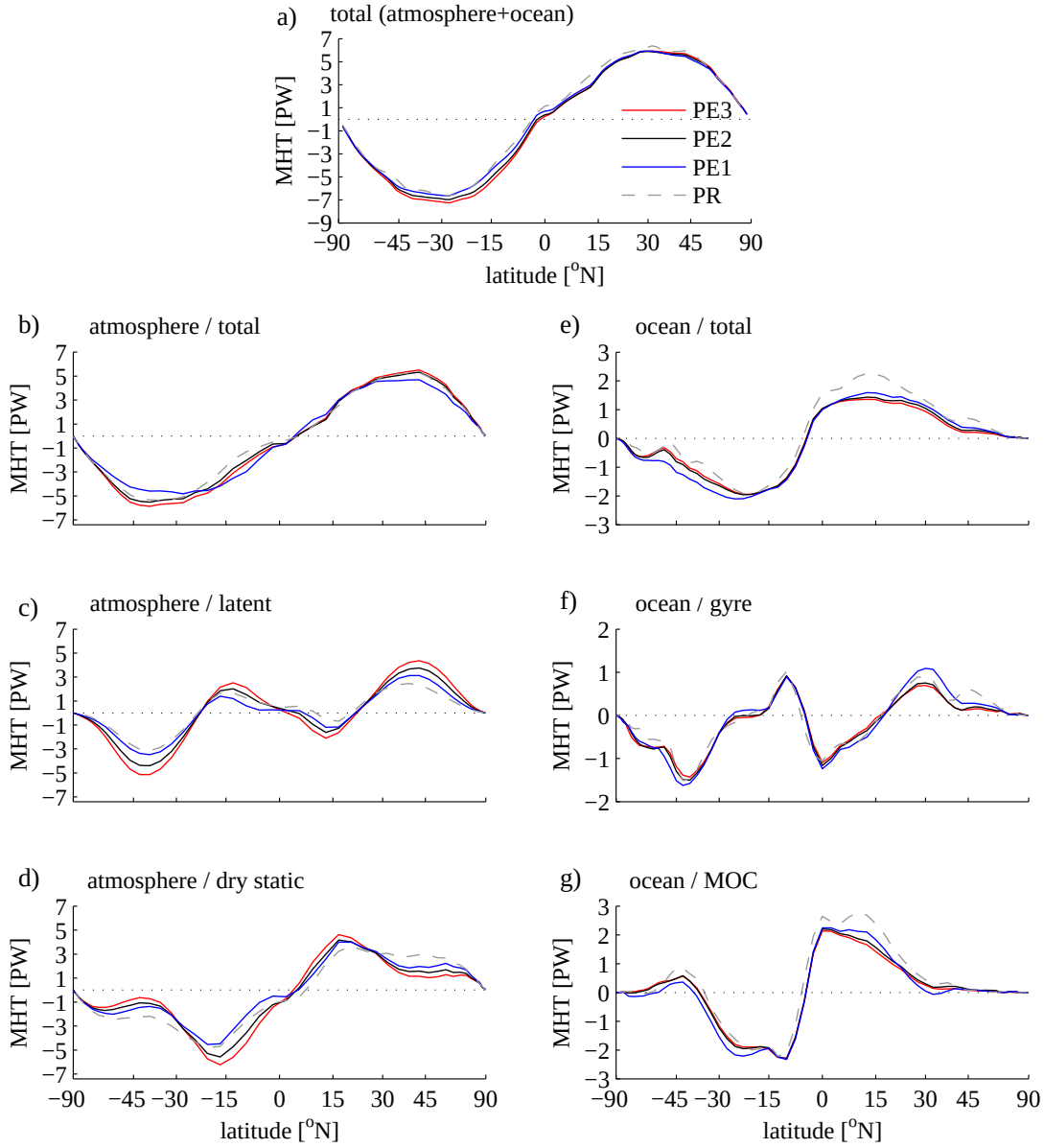

Figure 3.7: Meridional heat transport (MHT) by (a) the total atmosphere-ocean system, (b) the atmosphere, (c) latent heat in the atmosphere, (d) dry static energy in the atmosphere, (e) the ocean, (f) oceanic gyres, and (g) the oceanic meridional overturning circulation (MOC) for PR (grey), PE1 (blue), PE2 (black), and PE3 (red); oceanic MHT computed from the last 200 years of each run, atmospheric MHTs computed from 6 hourly values of the last 100 years of each run. The horizontal scale is linear in the sine of the latitude.

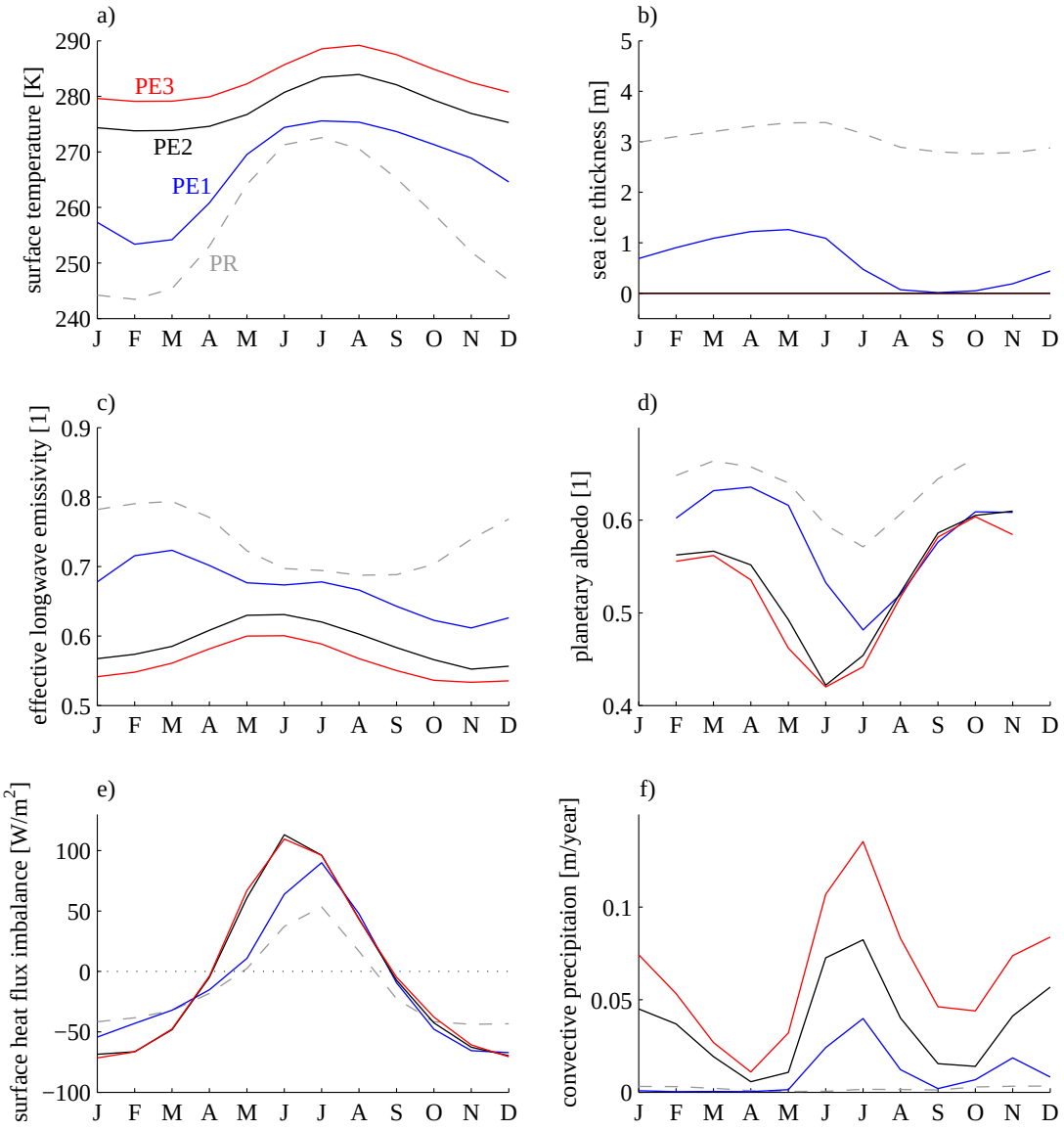

Figure 3.8: Seasonal variation of (a) surface temperature, (b) sea ice thickness, (c) effective longwave emissivity, (d) planetary albedo, (e) imbalance of the shortwave radiation, longwave radiation, sensible heat flux, latent heat flux, and conductive heat flux through sea ice; positive values mean that the ocean and/or sea ice take up heat from the atmosphere, and (f) convective precipitation averaged over the Arctic (north of 75° N) for PR (grey), PE1 (blue), PE2 (black), and PE3 (red); monthly means derived from the last 200 years of each simulation.

September, and on average reaches a maximum thickness of about 1 m (averages taken over the area north of 75° N). For comparison, the average Arctic sea ice thickness in the pre-industrial reference run amounts to about 3 m all year round.

The largest increases of the planetary albedo and the effective longwave emissivity in PE1 compared to PE2 occur in the northern hemisphere spring and early summer; they correlate with the sea ice differences (Figure 3.8). These changes in spring are the main reason for the high-latitude amplification of the annual mean zonal mean emissivity and albedo differences between PE2 and PE1 as seen in Figure 3.5. During the pCO_2 increase in PE3, the Arctic planetary albedo is only slightly reduced, because the sea ice is already gone in PE2 (Figure 3.8d). The Arctic warming in response to the pCO_2 increase from PE2 to PE3 is due to a seasonally homogeneously reduced effective longwave emissivity (Figure 3.8d). Consequently, the Arctic surface temperatures in PE3 compared to PE2 are equally warmer by about 5 K for all seasons (Figure 3.8a).

The disappeared sea ice also gives rise to an increased ocean-atmosphere heat exchange. During the northern hemisphere winter, the lack of sea ice in PE2 and PE3 leads to an increased oceanic heat release to the atmosphere compared to PE1 (Figure 3.8e). During summer, the ocean takes up more heat.

Abbot and Tziperman (2008) suggested that deep convection during winter in ice-free high-latitude oceans might lead to high-latitude warming. We do find that convective precipitation in the Arctic increases during winter and during summer (Figure 3.8f). This is consistent with the hypothesis of Abbot and Tziperman (2008). However, the large-scale precipitation in the Arctic also increases by about 0.2 m per year in PE2 compared to PE1 (not shown). This large-scale PE2-PE1 precipitation difference is four times as large as the convective precipitation difference. From the ECHAM5 output fields, we cannot separate the contributions to the emissivity and albedo changes from the different cloud-types. Hence, we cannot quantify the effect of the mechanism hypothesised by Abbot and Tziperman (2008) in this model setup.

3.1.8 Discussion and conclusions

We find that reducing pCO_2 to 280 ppm starting from the PE control simulation with 560 ppm leads to a cooling of about 4.7 K and regrowing sea ice. Taking proxy data at face value that suggest warm and sea ice free high latitudes even before the PETM (Sluijs et al. 2006), we conclude that a CO_2 concentration of 280 ppm is too low to appropriately simulate the PE climate. Our PE simulation with a CO_2 concentration of 560 ppm (PE2) is the best equivalent to the reconstructed pre-PETM climate (see comparison to proxy data in Chapter 2).

Changes in convective precipitation in the Arctic associated with the sea ice formation in response to the pCO_2 decrease in PE1 support the hypothesis that convective clouds cause high-latitude warming when sea ice melts (Abbot and Tziperman 2008). However,

we did not quantify this effect yet.

According to our model, increasing pCO_2 from 560 ppm to 840 ppm in PE3 leads to an increase of the global mean surface temperature by 3.8 K. The zonally averaged warming amounts to about 3 K at low latitudes and up to 5 K at high latitudes. The warming is already large enough to explain the reconstructed temperature increase during the PETM at some locations. We find large zonal differences in the warming pattern, which we will further discuss in Chapter 4.

The surface temperature increase by 3.8 K in PE3 in response to the 1.5-fold pCO_2 increase is equivalent to an equilibrium climate sensitivity of about 6.5 K. This extrapolated climate sensitivity is three times larger than the PE climate sensitivity reported by Shellito et al. (2003) and Winguth et al. (submitted). About 2/3 of the warming in PE3 are due to a reduced longwave emissivity, 1/3 of the warming is due to a reduced planetary albedo. Most of the planetary albedo reduction originates from a reduced cloud cover, surface albedo changes are small. The longwave cloud radiative effect hardly changes. Thus, most of the emissivity-driven warming is due to the radiative effects of the clear sky atmosphere. Our results indicate that the water vapour increase during PE3 has an effect that is twice as large as the direct effect of the pCO_2 increase. The pCO_2 increase experiment further indicates that the high-latitude amplification of the warming during the PETM was small - at least if we only look at zonal means.

In terms of the present-day oceanic methane hydrate reservoir, thermal dissociation of oceanic methane hydrate during the PETM could have released more than 1100 Pg to 2100 Pg C to the ocean and atmosphere (Dickens et al. 1995). Adding that much carbon entirely to the atmosphere is equivalent to an increase of atmospheric pCO_2 from 560 ppm to about 1500 ppm. However, not all of the carbon from such a methane release must end up in the atmosphere. Some part of it may be taken up by the ocean via dissolution or biological pumps, another part of it may enter the biogeochemical cycle over land (e.g., Denman et al. 2007). Our results indicate that a pCO_2 increase from 560 ppm to 840 ppm is already large enough to explain some estimates of SST increases during the PETM. Such a pCO_2 increase by 280 ppm is equivalent to the addition of less than 600 Pg C to the atmosphere. Even with the lower estimate of Dickens et al. (1995), the carbon input into the atmosphere would be large enough to explain the lowest estimates for the warming during the PETM, if not more than 50% of this release were taken up by the ocean, soil, and vegetation. We conclude that, according to our simulations, from the perspective of climate sensitivity, methane hydrates may have been the source of the GHG that caused the PETM. However, the question of how to explain the large increase of the carbonate compensation depth remains.

Increasing pCO_2 to 1120 ppm leads to a destabilisation of the simulated climate; a runaway effect occurs. We find that almost 1/4 of the warming during the runaway are caused by a reduction of the total cloud cover and the consequent relative warming due

to reduced reflection of shortwave radiation by clouds. Our results indicate that most of the residual warming is due to a decrease of the clear sky emissivity. We describe in Section 3.3 that the pCO_2 sensitivity critically depends on the ozone parameterisation. Unfortunately, using our GCM model setup, we cannot distinguish between the radiative effect of ozone and the other components of the clear sky atmosphere. Hence, we cannot rule out that the PE runaway climate is an artefact of unrealistic ozone concentrations. Note that, even if the runaway is not an artefact of overstressed parameterisations, it could still be due to the lack of feedback mechanisms from other Earth system components, for example the lack of vegetation feedbacks.

parameter	*PR*	*PE1*	*PE2*	*PE3*	*PE4T*
pCO_2 [ppm]	278	280	560	840	1120
2 m air temperature [K]	286.8	291.6	296.6	300.5	305.0
surface temperature τ_s [K]	287.6	292.3	297.0	300.8	305.1
$\tau_s^{ebm}(\alpha, \epsilon)$ [K]	289.5	293.2	298.0	301.6	306.5
$\tau_s^{ebm}(\alpha_c, \epsilon)$ [K]	303.8	309.0	313.5	316.1	320.3
$\tau_s^{ebm}(\alpha, \epsilon_c)$ [K]	281.1	284.5	289.4	293.1	297.4
$\tau_s^{ebm}(\alpha_c, \epsilon_c)$ [K]	295.0	299.9	304.5	307.2	310.8
$\tau_s^{ebm}(\alpha_s, \epsilon_c)$ [K]	298.2	303.6	307.8	310.4	313.8
planetary albedo α [1]	0.318	0.304	0.292	0.279	0.268
clear sky plan. alb. α_c [1]	0.173	0.141	0.133	0.130	0.127
surface albedo α_s [1]	0.137	0.098	0.094	0.093	0.093
emissivity ϵ [1]	0.585	0.568	0.541	0.525	0.501
clear sky emissivity ϵ_c [1]	0.658	0.640	0.608	0.589	0.564
vert. int. water vapour [kg m^{-2}]	25.5	31.4	45.3	59.2	82.4
total cloud cover [1]	0.617	0.604	0.576	0.557	0.544
shortwave CRF [Wm^{-2}]	-49.6	-55.6	-54.2	-51.0	-48.1
longwave CRF [Wm^{-2}]	28.8	30.0	29.6	30.0	31.3
albedo change due to clouds [1]	+0.145	+0.163	+0.159	+0.149	+0.141
emissivity change due to clouds [1]	-0.073	-0.072	-0.067	-0.064	-0.063
SW_t^{net} [Wm^{-2}]	233.0	238.1	242.1	246.4	250.4
LW_t^{net} [Wm^{-2}]	-231.2	-237.2	-240.8	-245.1	-247.8
heatflux imbalance (t) [Wm^{-2}]	+1.8	+0.9	+1.3	+1.3	+2.6
SW_s^{net} [Wm^{-2}]	154.7	159.5	159.2	160.5	160.8
LW_s^{net} [Wm^{-2}]	-55.2	-52.2	-44.3	-38.4	-30.5
latent heatflux [Wm^{-2}]	-80.1	-89.8	-99.6	-108.3	-116.9
sensible heatflux [Wm^{-2}]	-18.2	-17.3	-14.7	-13.0	-11.4
conductive (sea ice) [Wm^{-2}]	-0.4	-0.1	0	0	0
heatflux imbalance (s) [Wm^{-2}]	+0.8	+0.1	+0.6	+0.8	+2.0

Table 3.1: Global mean parameters as diagnosed from the preindustrial reference simulation (PR), and the PE simulations with onefold (PE1), twofold (PE2), threefold (PE3), and fourfold (PE4T) pre-industrial carbon dioxide concentrations. The diagnostics for the equilibrated runs PR and PE1 to PE3 are based on the last 200 years of each simulation. PE4 does not equilibrate, however, the column PE4T contains diagnostics based on the years 2430 to 2439 of the transient run PE4.

3.2 Rapid radiative transport model out of bounds?

3.2.1 Problem

Forcing the standard PE version of ECHAM5/MPI-OM with carbon dioxide concentrations of 840 ppm or 1120 ppm leads to unhoped-for stops of ECHAM5 at a global mean temperature of approximately 300 K (red dots in Figure 3.9). ECHAM5 stops at those timesteps because the temperature of a single gridbox in the atmosphere exceeds a pre-defined temperature range. Additional experiments (not shown) have revealed that these so-called lookup table overflows occur over land and over the ocean, and they occur at intermediate model levels rather than at the highest temperatures close to the surface. The lookup table overflows are detected in differing routines (e.g., vdiff.f90, cucall.f90), and are due to too low or too high temperatures. Moreover, the pre-defined, 'allowed' temperature range is not left gradually, but within single timesteps due to large temperature tendencies of sometimes up to several hundred Kelvin per hour. We find that these extreme, unrealistic temperature tendencies originate from extreme vertical longwave radiative transports as computed in the rapid radiative transfer model (RRTM).

The closer analysis of one of the lookup table overflows reveals that the extreme longwave radiative flux only appears in the full sky but not in the clear sky computation, suggesting that there is a problem related to clouds. However, we find that the actual reason for the large longwave radiative fluxes are negative optical depths from gases or aerosols. Optical depths are found by integrating extinction coefficients for electromagnetic radiation over incremental distances. The unitless optical depth thus quantifies scattering and absorption that occurs along a certain distance (see, e.g., Jacobson 1999). A negative optical depth would mean an increase of the radiative flux along the incremental distance due to scattering or absorption. This is physically not reasonable. In the above mentioned case, the negative optical depth occurs in the 100th of the 140 intervals in the RRTM g-space. The 100th g-space interval belongs to the longwave radiation band 9, which covers the wavenumber range of 1180 to 1390 cm^{-1}. Key species for this band are water and methane in the lower atmosphere, and methane in the middle/upper atmosphere (Mlawer et al. 1997).

However, negative optical depths on their own do not necessarily lead to extreme longwave radiative fluxes. In the above mentioned case, negative values occur for several timesteps in a row, before a singularity during a Padé approximation in the full sky code of the RRTM routine RRTM_RTRN1A_140GP leads to the extremely high longwave flux.

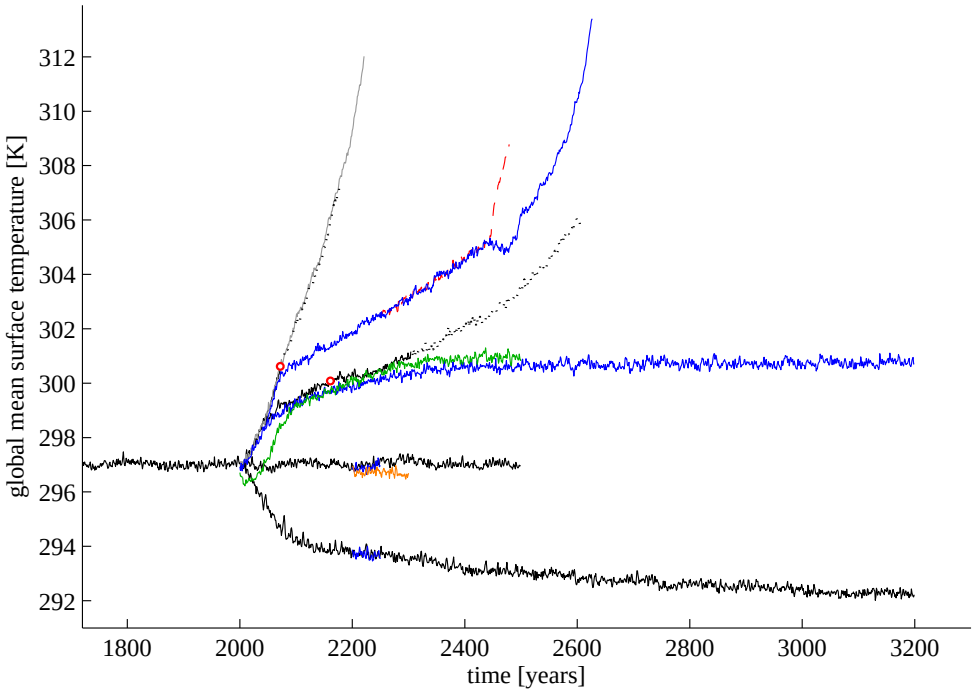

Figure 3.9: Timeseries of the global mean surface temperature for the different experiments discussed in this chapter. Black solid lines are runs that use the original ECHAM5 source code. The lowest and the middle black solid lines are computed from PE1 and PE2, respectively. The red dots indicate the first occurrences of lookup table overflows in the 840 ppm and 1120 ppm carbon dioxide increase experiments. The lower and upper black dotted lines indicate the 840 ppm and 1120 ppm experiments with temperature tendencies limited to ± 24 K per timestep. The grey line indicates the 1120 ppm experiment with the RRTM modified such that negative optical depths are set to zero. Blue lines are runs with tropospheric ozone limited to 400 ppb. The orange line corresponds to a run with tropospheric ozone limited to 150 ppb. The green line corresponds to a carbon dioxide increase experiment to 1120 ppm with all tropospheric ozone moved into the uppermost level of ECHAM5. All blue runs, the upper grey run, the orange run, and the green run make use of the RRTM modification which sets negative optical depths to zero. The dashed red line is a run similar to the blue 1120 ppm run (PE4), however, in that red run, the algorithm for the tropopause diagnostic fails, which leads to an artificial acceleration of the runaway by too high tropospheric ozone concentrations; therefore, in PE4, we apply an adaptation of the algorithm to ensure a correct detection of the tropopause (see Appendix A).

3.2.2 Bugfix

One approach to keep ECHAM5 running despite the negative optical depths is to limit the temperature trends. As a result of limiting the temperature trends in the PE simulation with 840 ppm to ±24 K per timestep, there are no more lookup table overflows, and ECHAM5 runs numerically stable. However, the global mean surface temperature does not equilibrate after the carbon dioxide forcing is held constant at 840 ppm (Figure 3.9). The global mean surface temperature first approaches a plateau at about 300 K, but subsequently increases exponentially. The climate becomes unstable. We find that this runaway effect is artificially caused by the prescribed ozone climatology (Section 3.3).

Another workaround is to set negative optical depths in the RRTM to zero, which tackles the problem closer to its source. We apply this workaround to the 1120 ppm simulation. As a consequence, the simulation becomes numerically stable again without any extreme temperature trends nor lookup table overflows. We find that both bugfix types —setting negative optical depths to zero, or limiting the temperature tendencies— lead to similar 1120 ppm simulations (Figure 3.9, solid grey line and dashed black line are on top of each other). In both simulations, the global mean surface temperature increases rapidly without any sign of stabilisation.

3.2.3 Relevance of the modification

We find that negative optical depths in our PE model setup occur for all carbon dioxide concentrations of 280 ppm to 1120 ppm. Both the frequency and the magnitude of the negative optical depths increase with higher global mean surface temperatures. In the PE simulation with 280 ppm, at temperatures around 294 K, the magnitude of the negative values does not exceed 0.1, and there are less than 1000 occurrences of negative values per timestep. Note that typical optical depths are in the order of 1 to 10. In the control simulation with 560 ppm, at a global mean surface temperature of about 297 K, there are already several thousand small negative optical depths, and negative values in the order of 1 do occur at some timesteps. In the simulation with 1120 ppm, at a global mean surface temperature of more than 305 K, these relatively large negative values occur several thousand times per timestep. However, also note that the total number of optical depths computed per timestep is in the order of 10^7 (one optical depth for each of the 140 intervals in g-space, 96×48 horizontal gridpoints, and 19 vertical levels).

Setting these relatively few negative optical depths to zero helps to numerically stabilise ECHAM5. At the same time, because the relative number of these modifications is small, the effect of these modifications on the actual, simulated climate state may be small. The fact that the 1120 ppm runs with and without the optical depth bugfix are similar during the years 2000 to 2073 (Figure 3.9) supports the notion that the optical depth modifications do not have a large effect on the simulated climate state.

However, negative optical depths are a bad sign, and may be a hint to basic limitations of the rapid radiative transfer model.

3.3 Climate sensitivity to tropospheric ozone

3.3.1 Motivation

Unfortunately, there is no proxy for the atmospheric ozone concentrations during the PE. For simplicity, the ozone concentration in our PE model setup is based on ozone observations over the period 1980 to 1991 (Section 2.2, Fortuin and Kelder 1998). In theory, we could compute the ozone concentrations using a middle atmosphere model with fully interactive chemistry. However, a long-term, coupled ocean-atmosphere-chemistry GCM simulation is computationally too expensive at present. Moreover, even if we find a workaround for the computational cost, determining PE boundary conditions for the chemistry model is difficult. For example, nitrous oxide, which is produced by bacterial processes in soils (Brasseur and Solomon 1986), influences the chemical cycle of ozone; determining nitrous oxide sources is difficult even in the present-day climate (McElroy 1980). To account for all effects that influence the tropospheric and stratospheric ozone concentrations is beyond of the scope of this work. Nevertheless, in this section, we argue that a prescribed ozone distribution based on the observations of Fortuin and Kelder (1998) is inappropriate for very warm climate simulations, and may lead to artificial warming. We propose a simple ozone parameterisation scheme to avoid such artificial warming.

3.3.2 Ozone parameterisation

Ozone is naturally produced in two steps. First, photodissociation of molecular oxygen by ultraviolet radiation at wavelengths shorter than 242.4 nm produces atomic oxygen (Chapman 1930):

$$O_2 + hv \longrightarrow O + O. \tag{3.3}$$

In the second step, which competes with other recombination processes (Brasseur and Solomon 1986), the oxygen atom undergoes a binding collision with an oxygen molecule to form an ozone molecule

$$O + O_2 \longrightarrow O_3. \tag{3.4}$$

As a result of these mechanisms, the greatest ozone production occurs in the tropical stratosphere. Ozone concentrations in the troposphere are much smaller than in the stratosphere (e.g., Fahey 2007). In our simulations with prescribed ozone, the tropopause, which is the border between the stratosphere and the troposphere, moves upward with increasing global mean temperatures (Figure 3.10a). An upward shift of the tropopause should go in hand with an upward shift of the maximum ozone

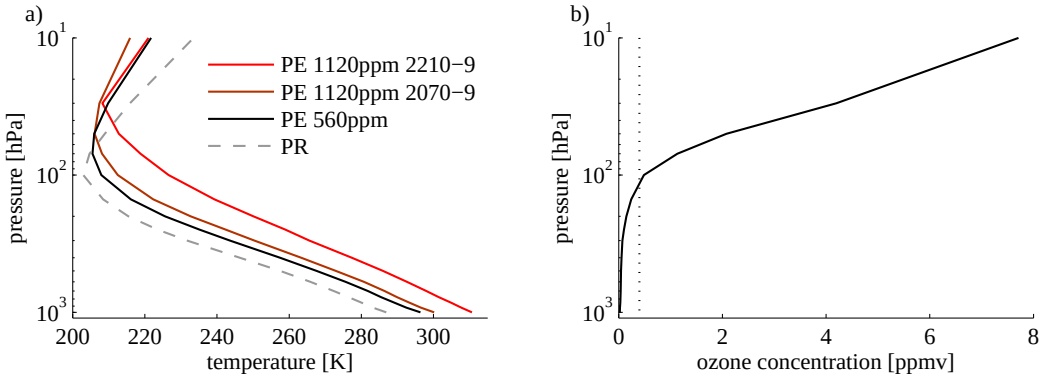

Figure 3.10: (a) Global mean vertical temperature profile for the pre-industrial run (PR, grey dashed), the PE control run (black), and two different intervals of the carbon dioxide increase experiment to 1120 ppm (brown: years 2070-2079, red: years 2210 to 2219; run with negative optical depths set to zero, grey line in Figure 3.9). (b) Global mean vertical ozone profile as prescribed in the standard version of ECHAM5 (interpolated from Fortuin and Kelder 1998); dotted line indicates ozone concentration of 0.4 ppm.

concentration. An upward shift of the tropopause without adjustment of the ozone distribution leads to large ozone concentrations in the upper troposphere, although these large concentrations belong into the stratosphere (compare Figures 3.10a and b). To avoid these artificial, large ozone concentrations in the upper troposphere, we define a maximum ozone concentration (pO_3^*) within the troposphere. Ozone molecules from below the tropopause that contribute to concentrations above pO_3^* are moved into the uppermost level in ECHAM5, such that the vertically integrated number of molecules is preserved.

A further analysis of HAMMONIA chemistry climate model simulations published by Schmidt et al. (2006) revealed that, for contemporary conditions, doubling the atmospheric carbon dioxide leads to an increased tropopause height, an upward shift of the ozone concentrations, and an increased stratospheric ozone concentration in the tropics (Schmidt, personal communication). This suggests that our parameterisation, which shifts ozone upwards along with the tropopause height, may be a reasonable, first-order approximation of the actual dynamical and chemical processes.

3.3.3 Results

We investigate the effect of this tropospheric ozone limitation in the four different carbon dioxide experiments (with 280, 560, 840, and 1120 ppm pCO2). We set pO_3^* to

0.4 ppm (see Figure 3.10b, dotted line).

The ozone limitation has little effect on the ozone distribution in the control simulation with 560 ppm carbon dioxide (Figure 3.11a and c). The annual mean ozone concentrations at about 100 hPa are reduced by less than 0.1 ppm; the largest reductions occur at northern high latitudes. Note that, when ozone is shifted to the uppermost level, the total number of ozone molecules is preserved, not the average ozone concentration. For the 560 ppm control run, the reduction of tropospheric ozone does not affect the temporal mean of the global mean surface temperature (Figure 3.9). The effect of the ozone limitation in the experiment with 280 ppm carbon dioxide is even smaller, because the tropopause is lower (Figure 3.11b). Thus, as for the control run, the temporal mean of the global mean surface temperature is not affected.

By contrast, for the carbon dioxide increase experiments, the tropospheric ozone limitation has a large climatic effect. Including the ozone parameterisation in the 840 ppm carbon dioxide experiment leads to a stabilisation of the climate (Figure 3.9). This stabilisation is due to a reduction of ozone concentrations at the tropopause by less than 1 ppm (Figure 3.11d). It is remarkable that an ozone increase in the upper troposphere by less than 1 ppm could cause a runaway climate. Luckily, we produced these increased upper tropospheric ozone concentrations artificially. Still, this result points out that atmospheric chemistry has potentially large effects on the surface climate. The climate of the 1120 ppm carbon dioxide experiment, even with limited tropospheric ozone concentrations, remains unstable (Figure 3.9). However, the reduced ozone concentrations (Figure 3.11e) lead to a strong reduction of the global mean surface heating rate.

Maybe the runaway climate in the 1120 ppm simulation persists because the allowed tropospheric ozone concentration is still too high. To test this hypothesis, we again run the 1120 ppm carbon dioxide experiment this time with *all* tropospheric ozone removed (Figure 3.9, green line). If the runaway effect is due to tropospheric ozone, the 1120 ppm simulation without tropospheric ozone must stabilise. If it does not stabilise, another (possibly not artificial) mechanism must be responsible for the climate destabilisation. We find that the 1120 ppm run without tropospheric ozone does stabilise. It equilibrates at a global mean surface temperature of about 301 K. Moving all tropospheric ozone from the troposphere into the stratosphere has a strong cooling effect —even on the control climate, as seen from the initial cooling despite the carbon dioxide increase. The equilibrium global mean surface temperature of this 1120 ppm run is similar to the one with 840 ppm and tropospheric ozone limited to 0.4 ppm. Because the surface temperatures in the 1120 ppm run without tropospheric ozone are relatively cold, we cannot exclude the possibility that a different mechanism would lead to a runaway climate for warmer temperatures; in other words, we may not have reached the bifurcation. One possibility to affirm that all runaway climates we have seen here are artificially induced by tropospheric ozone would be to assure that the simulation without tropospheric ozone remains stable for even higher carbon dioxide concentrations.

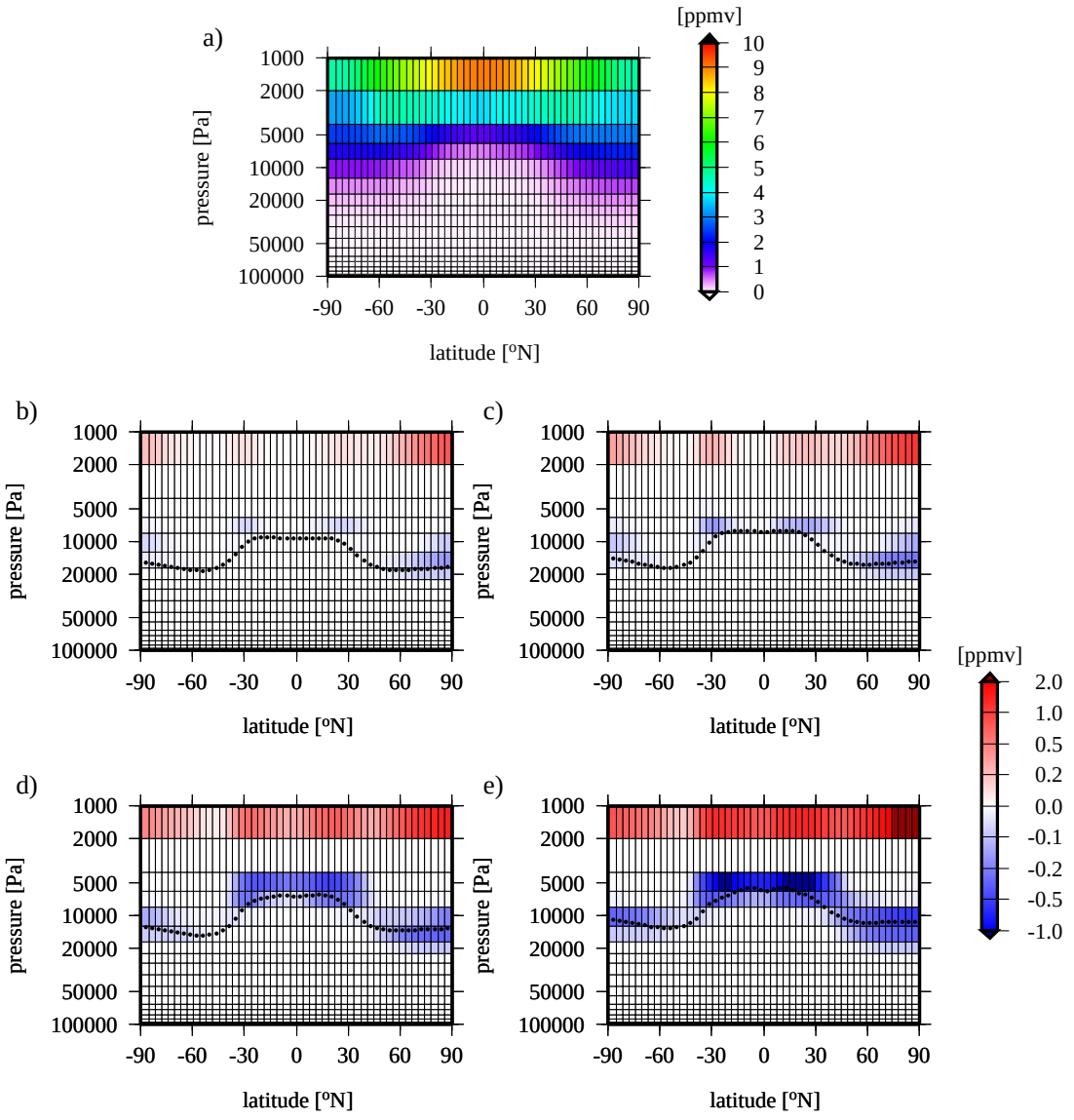

Figure 3.11: (a) Annual mean ozone climatology as interpolated from Fortuin and Kelder (1998), and differences from the ozone climatology for runs that use the ozone parameterisation and carbon dioxide concentrations of (b) 280 ppm (years 2240-2249), (c) 560 ppm (years 2240-2249), (d) 840 ppm (years 3000-3199), and (e) 1120 ppm (years 2430-2439); blue shading indicates a reduction of ozone due to the parameterisation; all the respective runs (b-e) are plotted as blue lines in Figure 3.9.

This is left for future studies.

For the present-day climate, the maximum tropospheric ozone concentration may be as low as 0.15 ppm (Rast, personal communication). Allowing for tropospheric ozone concentrations of up to 0.4 ppm may induce some warming of the surface climate in the (compared to the present-day climate) already relatively warm 280 and 560 ppm PE simulations. In other words, part of the PE-PR effective emissivity reduction (Chapter 2) may be artificially caused by too high tropospheric ozone concentrations. To pursue this presumption, we rerun part of the control simulation with a maximum tropospheric ozone concentration of 0.15 ppm. The resulting global mean surface temperature decreases by about 0.5 K (Figure 3.9, orange line). We conclude that the artificial contribution of tropospheric ozone to the emissivity-induced PE-PR surface warming as discussed in Chapter 2 amounts to at most 0.5 K.

Chapter 4

PE ocean circulation

4.1 Introduction

Previous studies based on numerical modelling and paleo-reconstructions of the PE ocean circulation suggested that the warming during the PETM was associated with, and possibly initialised by, an abrupt change of the global ocean cirulation. To test this hypothesis, we use ECHAM5/MPI-OM to study the PE ocean circulation and its sensitivity to a variation of atmospheric pCO_2.

As discussed in Section 3.1, the PETM was linked to an increase of atmospheric pCO_2, but the source of the CO_2 input is unknown. Dickens et al. (1995) argued that the CO_2 most likely originated from methane hydrates in ocean sediments. They suggested that bottom water warming could have led to thermal dissociation of those methane hydrates and the subsequent release of methane to the ocean and atmosphere.

The methane hydrate dissociation hypothesis requires a trigger. Thomas and Shackleton (1996) speculated that CO_2 from volcanism in the North Atlantic could have warmed high latitudes, leading to the shutdown of high-latitude sinking and the onset of subtropical warm and salty deep water formation. The change from high-latitude to subtropical sinking had previously been suggested to explain the reconstructed rapid bottom water warming during the PETM (Kennett and Stott 1991, this was before the methane hydrate dissociation hypothesis came up).

Bice and Marotzke (2002) found that bottom water warming can also result from a switch from high-southern to high-northern latitude sinking. In their ocean GCM study, an intensification of the atmospheric hydrological cycle (i.e., increased evaporation in the subtropics and increased precipitation in the tropics and at high latitudes) initially led to a warming of intermediate waters due to increased downward movement of relatively saline, warm, subtropical surface waters (see also Bice and Marotzke 2001). Given the existence of a land bridge between proto-Britain and proto-Greenland as a barrier to North Atlantic flow, increasing the strength of the hydrological cycle by 60% caused the sudden onset of sinking in their North Pacific. As their North Pacific was warmer than the previous sinking region, the South Pacific, this switch in dominant deep water source led to a widespread bottom water warming.

Bottom water warming is not the only mechanism that can lead to dissociation of methane hydrates. For example, Katz et al. (2001) suggested that continental slope failure resulted in a catastrophic methane release. Röhl et al. (2000) found that the carbon isotope excursion (CIE) at the onset of the PETM at ODP Site 690 in the Weddell Sea occurred in several, distinct steps. These CIE-steps are consistent with methane releases due to several, distinct continental slope failures. Other suggested mechanisms for methane release include sea level lowering, a comet impact, or the explosive release of metamorphic thermogenic methane from the North Atlantic Volcanic Province (Svensen et al. 2004; Thomas et al. 2006; Thomas 2007).

The hypothesis that a global ocean circulation change significantly contributed to the climate change during the PETM was strengthened by relatively recent evidence from proxy-data. Carbon isotope records indicate that the meridional overturning circulation (MOC) changed from southern sinking to northern sinking at the start of the PETM (Tripati and Elderfield 2005; Nunes and Norris 2006).

In this chapter, we test the hypothesis of ocean circulation changes at the start of the PETM using the coupled atmosphere-ocean GCM ECHAM5/MPI-OM. This advances the ocean-only GCM approach of Bice and Marotzke (2002), and necessitates a different strategy in our numerical experiments. Instead of studying the effect of a stronger, prescribed hydrological cycle, we investigate the ocean circulation response to a variation of atmospheric pCO_2 with all its feedbacks, such as a change of the hydrological cycle.

The philosophy behind this approach is as follows. We aim at testing whether some boundary condition change may have triggered an ocean circulation switch. This boundary condition change may have been the input of volcanogenic CO_2, as suggested by Thomas and Shackleton (1996). It may also have been the several million years long warming trend during the Paleocene towards the Early Eocene Climatic Optimum (Zachos et al. 2001). Whether that warming trend was indeed due to a pCO_2 increase or not, we mimic that warming by a pCO_2 increase. We also study the ocean circulation response to a pCO_2 *decrease*. This sounds counter-intuitive, because it appears more likely that the PETM-triggering boundary condition change is to be mimicked by a pCO_2 increase. However, our motivation is to search the *PE ocean circulation phase space* for qualitatively different solutions. If we do find different ocean circulation solutions, we can then think about possible transitions between them, and their implications for the PETM.

This chapter is organised as follows. In Section 4.2, we describe the ocean circulation in the PE control simulation (PE≡PE2), and identify main differences compared to the pre-industrial reference simulation (PR). In Section 4.3, we study the response of the global ocean circulation to a variation of atmospheric pCO_2. In Section 4.4, we compare the simulated PE ocean circulation and ocean circulation changes to paleoreconstructions. In Section 4.5, we discuss our results and present the conclusions.

4.2 Simulated PE ocean circulation

4.2.1 Surface and barotropic flows

In our PE model setup, the Indian Ocean, the North Atlantic, and the Arctic are connected via the open Tethys Seaway. At the surface, the open Tethys Seaway allows for a westward current from the Indian Ocean into the Atlantic along the coastline of Africa (Figure 4.1). Integrated over the entire depth, we find a westward flow of about 11 Sv into the Tethys between the north-eastern tip of Africa and the largest island in the Tethys (Figure 4.2). Part of this inflow is balanced by a southward transport of about 3 Sv from the Tethys into the Indian Ocean between that largest Tethys island and Asia. About 7 Sv are transported from the Tethys into the Atlantic along the African north coast. About 0.7 Sv are transported northward into the Arctic from the Tethys across the 200 m shallow sill between Europe and Asia. The transport between proto-Greenland and Europe is also northward, but only amounts to less than 0.1 Sv. The oceanic transport into the Arctic is overbalanced by a southward transport of about 1.1 Sv through the Bering Strait into the North Pacific. Note that the oceanic volume transport thus leads to a net export of Arctic water into the North Pacific, while atmospheric moisture transport and river runoff lead to a net import of freshwater into the Arctic (Figure 4.3a).

The more southward position of Australia and the almost closed Drake Passage inhibit a strong Antarctic Circumpolar Current in PE (Figure 4.2). The Drake Passage and the sill between Australia and Antarctica are about 300 to 400 m deep in PE (Figure 2.1a). The eastward Drake Passage transport in PR amounts to about 140 Sv, while it is only 5 Sv in PE. The transport between Australia and Antarctica in PR amounts to 200 Sv, while it is only 5 Sv in PE.

The narrower PE North Atlantic bathymetry inhibits the formation of the North Atlantic current and the subpolar gyre (Figures 4.1 and 4.2). The lack of this subpolar gyre in PE explains the reduced northward meridional oceanic gyre heat transport in PE compared to PR (Figure 2.7b).

The position of the MPI-OM grid-South Pole on South America yields a relatively fine resolution of the open Central American Isthmus in PE. The center of the isthmus is up to 2000 m deep. However, the sill depth at the boundary between the East-Pacific-Caribbean Plate and the North American Plate amounts to only about 700 m (Cuba is on that boundary, see Figure 9 in Sykes et al. 1982; Bice and Marotzke 2001). Even though the Central American Isthmus in PE is open, the westward Equatorial Atlantic Current does not entirely end up in the Pacific, but instead flows northward around Cuba to form a proto-Gulf Stream (Figure 4.1). In contrast to the mainly westward surface velocities along the South American coast, the total volume transport through the Central American Isthmus is eastward from the Pacific into the Atlantic. The total

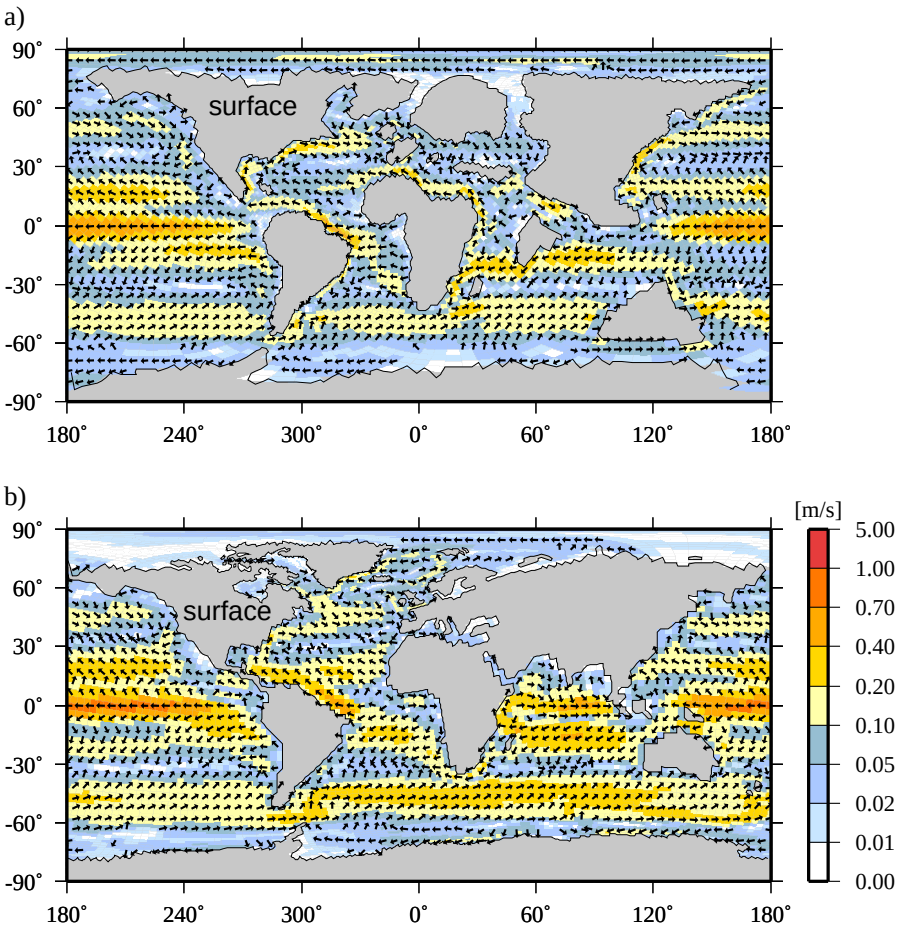

Figure 4.1: Horizontal velocity in the surface layer (uppermost 12 m) averaged over the last 200 years of (a) PE, and (b) PR; for readability, the velocity vectors are interpolated onto a coarse regular grid; background colors indicate the magnitude of the velocity.

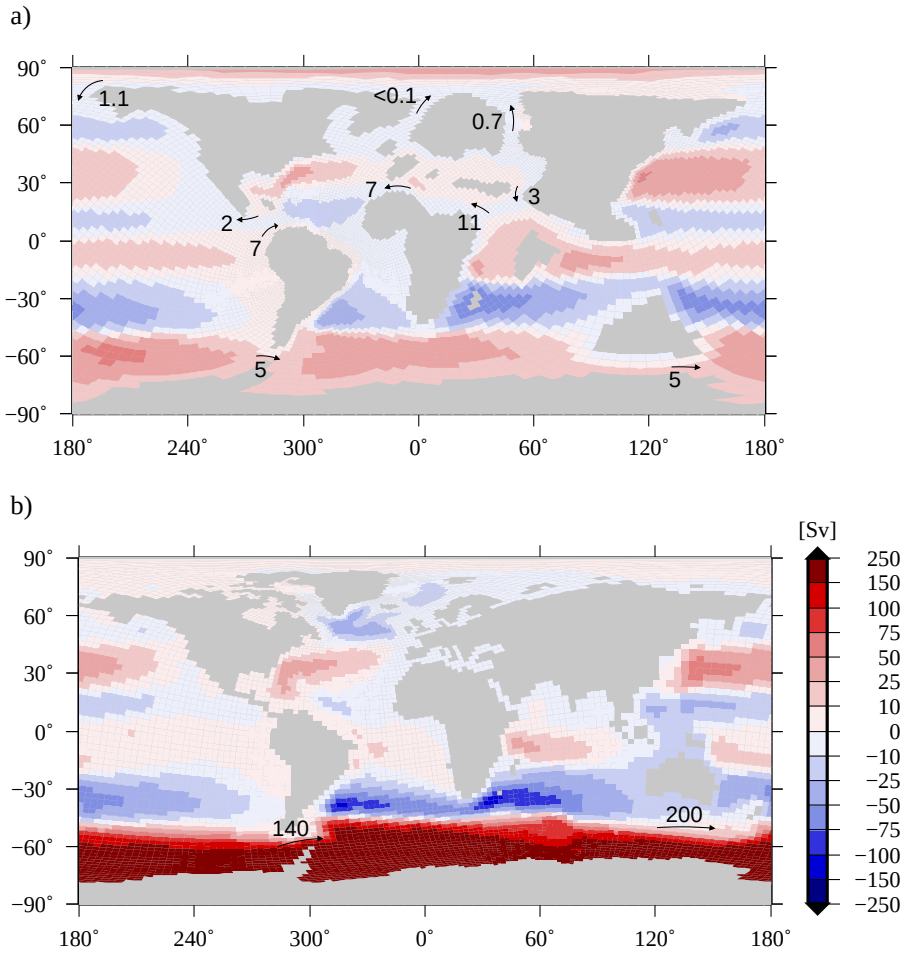

Figure 4.2: Horizontal barotropic streamfunction averaged over the last 200 years of (a) PE, and (b) PR; red maxima are to the right of the flow, blue maxima to the left; the vectors indicate volume transports in Sv.

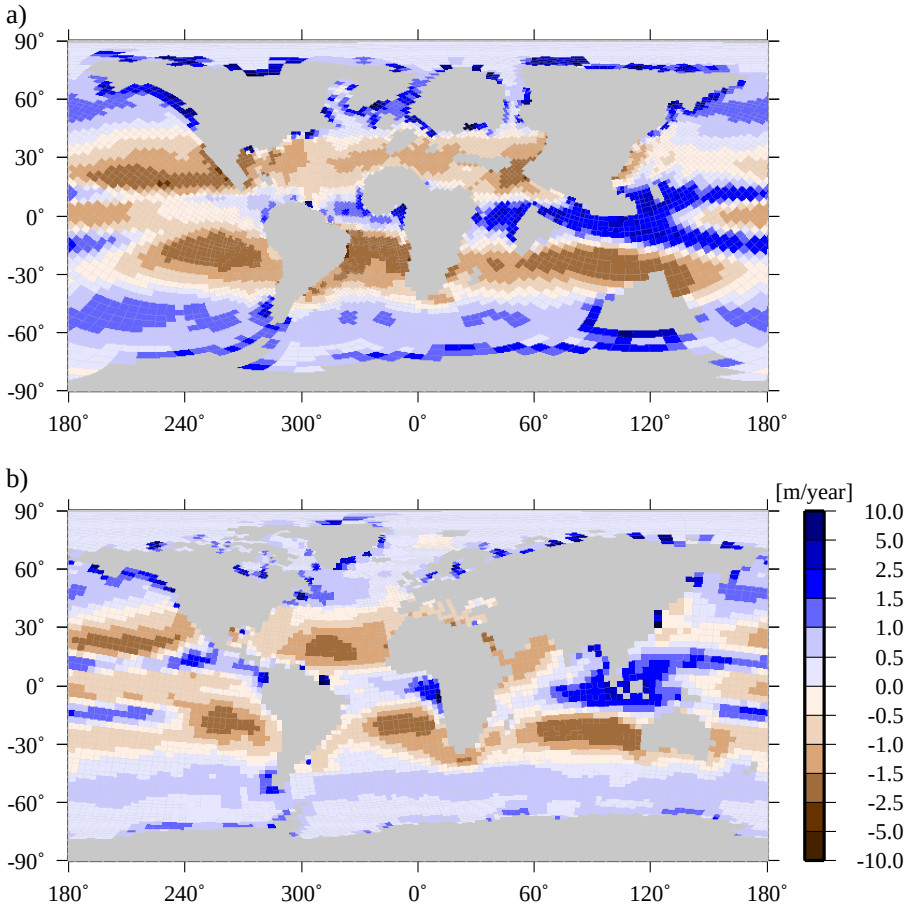

Figure 4.3: Annual mean total precipitation minus evaporation plus river runoff into the ocean averaged over the last 200 years of (a) PE, and (b) PR.

transport amounts to about 5 Sv. It is composed of an eastward barotropic flow of about 7 Sv from the Pacific into the Atlantic along the coastline of South America. This eastward flow is partly compensated by a westward flow into the Pacific of about 2 Sv around the southern tip of North America (Figure 4.2).

4.2.2 Meridional overturning circulation (MOC)

The PE global meridional overturning circulation (MOC) is weaker than the MOC in PR (Figure 4.4), but the large-scale structures of the MOCs in PE and PR are quite similar. Both PE and PR show North Atlantic sinking. The maximum value of the PE Atlantic MOC amouts to about 12 Sv at 40° N and 800 m depth. For comparison, the maximum value of the Atlantic MOC in PR amounts to more than 15 Sv at 30° N and 1300 m depth. The Antarctic Bottom Water (AABW) outflow in PR amounts to more than 6 Sv, less than 3 Sv of this outflow reach the North Atlantic. In PE, AABW formation is much weaker.

During the last 200 years of PE, AABW is mostly formed in the South Pacific, but there is also some sinking in the South Atlantic and Indian Ocean (Figure 4.4). Note that the Southern Ocean sinking exhibits a large temporal variability. Deep water formation occurs in episodic flushes. The flushes in the South Pacific seem to be anticorrelated to the flushes in the South Atlantic and Indian Ocean (Figure 4.5). However, we have not yet understood the processes that lead to these flushes.

As in PR, there is no sinking in the North Pacific in PE because of too low sea surface salinities. The sea surface salinity in the North Pacific in PE only amounts to about 31 psu, which is about 4 psu lower than in the proto-Labrador Sea. In the North Atlantic as well as the North Pacific, precipitation and river runoff exceed evaporation (Figure 4.3). The large difference between the North Atlantic and North Pacific sea surface salinities could arise because the proto-Gulf Stream carries saltier water than the proto-Kuroshio (Figures 4.7 and 4.1). Moreover, there is an inflow of surface water with very low salinities from the Arctic Ocean through the shallow Bering Strait into the North Pacific.

On a basin-wide scale, the global ocean circulation in PE with sinking in the North Atlantic and upwelling in the North Pacific resembles the global oceanic 'conveyor belt' as found in PR and the present-day real ocean. However, the MOC as illustrated in Figure 4.4 as a basin-wide integrated streamfunction belies the rather complex zonal structure of the actual ocean circulation.

In the PE Atlantic, warm (Figure 4.6a), saline (Figure 4.7a), subtropical surface water flows northward along the east coast of North America into the proto-Labrador Sea (Figure 4.1a). On its way, the surface water cools down to approximately 290 K, maintains a salinity of about 35 psu, and becomes the densest surface water in the northern hemisphere (about 1026 $\mathrm{kg\,m^{-3}}$, Figure 4.8a). Because the surface water is so

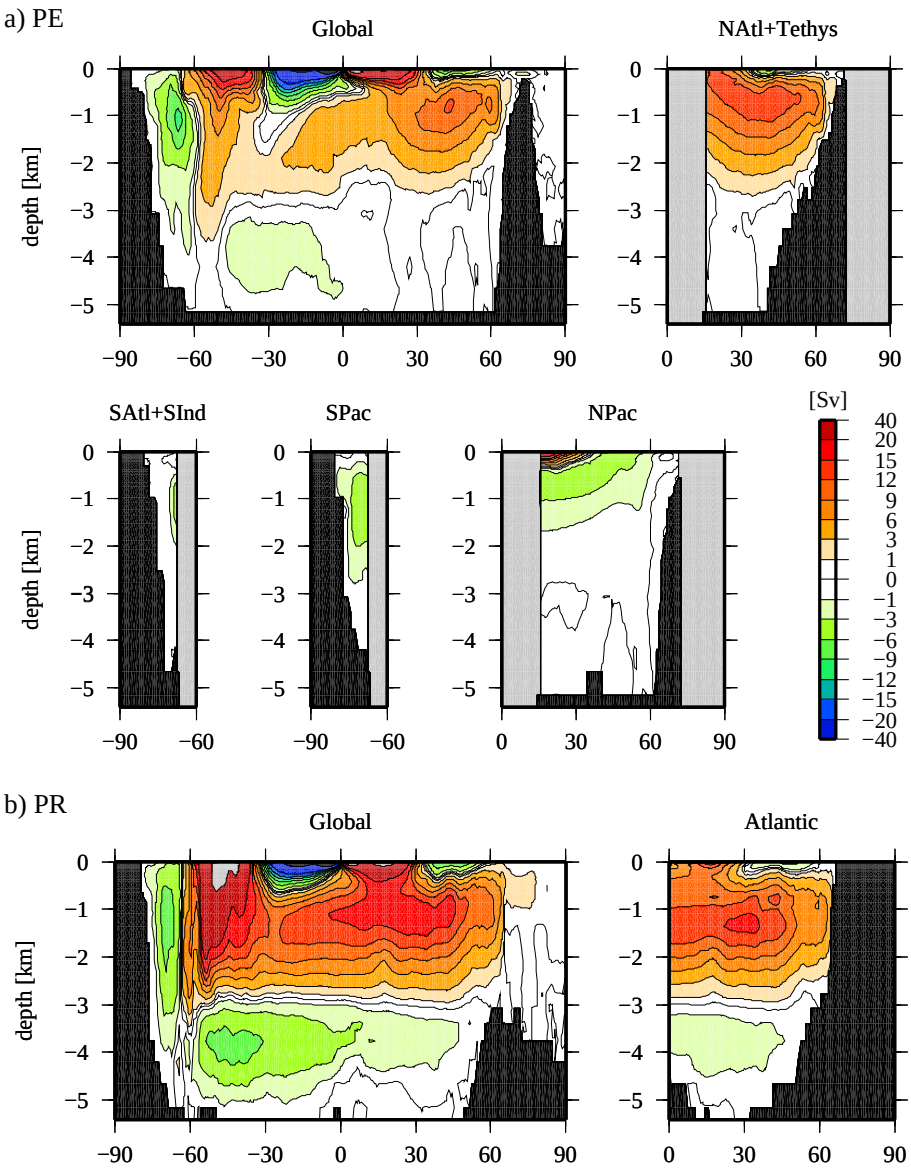

Figure 4.4: Meridional overturning circulation (MOC) averaged over the last 200 years for (a) PE; computed for the global ocean (Global), the North Atlantic and Tethys (NAtl+Tethys), the South Atlantic and Indian Ocean (SAtl+Ind), the South Pacific (SPac), and the North Pacific (NPac), and (b) PR. Contour intervals are as indicated in the color scale; positive values correspond to clockwise circulation as viewed from reader's perspective.

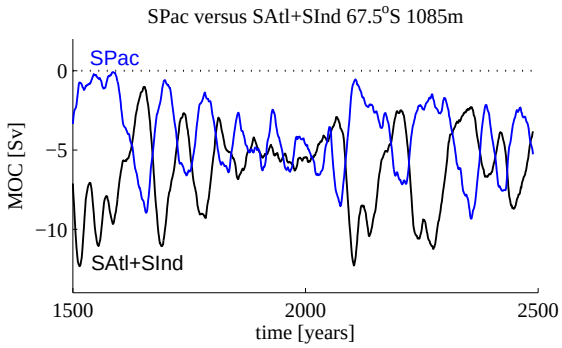

Figure 4.5: Time series of the meridional overturning circulation (MOC) in PE at 67.5° S at 1085 m depth integrated over the South Pacific (blue), and the South Atlantic and Indian Ocean (black).

dense, the water column easily becomes unstable, and convection occurs (Figure 4.9a). This convection and the net sinking as seen from the MOC (Figure 4.4a) lead to the formation of North Atlantic Deep Water (NADW). This NADW spreads southward first as a relatively wide stream until it becomes a narrower western boundary current along the coast of North America (Figure 4.10a). Although the Central American Isthmus in PE is open, the NADW crosses the equator below the sill and follows the South American east coast through the Atlantic into the Southern Ocean. In PR, the densest surface water in the Atlantic forms in the Norwegian Sea north of the Greenland-Scotland ridge (Figure 4.8b); deep convection occurs in the Norwegian Sea and around the southern tip of Greenland (Figure 4.9b).

PE surface water in the Southern Ocean is even heavier than in the proto-Labrador Sea (Figure 4.8a). Relative to the surface water in the proto-Labrador Sea, surface water in the South Pacific (proto-Ross Sea) is about 2 psu fresher (Figure 4.7a), but about 10 K colder (Figure 2.3.1a). In PE, deep convective events occur in the South Atlantic (or proto-Weddell Sea), Southern Indian Ocean, and the South Pacific (Figure 4.9a). In PR, deep convection mainly occurs in the South Atlantic (Figure 4.9b).

Convection and sinking in the proto-Labrador Sea in PE are associated with a heat release of up to 150 Wm^{-2} from the ocean to the atmosphere (Figure 4.12). By contrast, the oceanic heat release associated with the NADW formation in PR is concentrated at the deep water formation sites in the Norwegian Sea. The largest oceanic heat release in the Southern Ocean is located south-east of proto-Australia, and in the South Pacific. By contrast, the largest oceanic heat release in the Southern Ocean in PR occurs along the Antarctic coast south of Africa, which is also the Southern Ocean area of deep convection in PR.

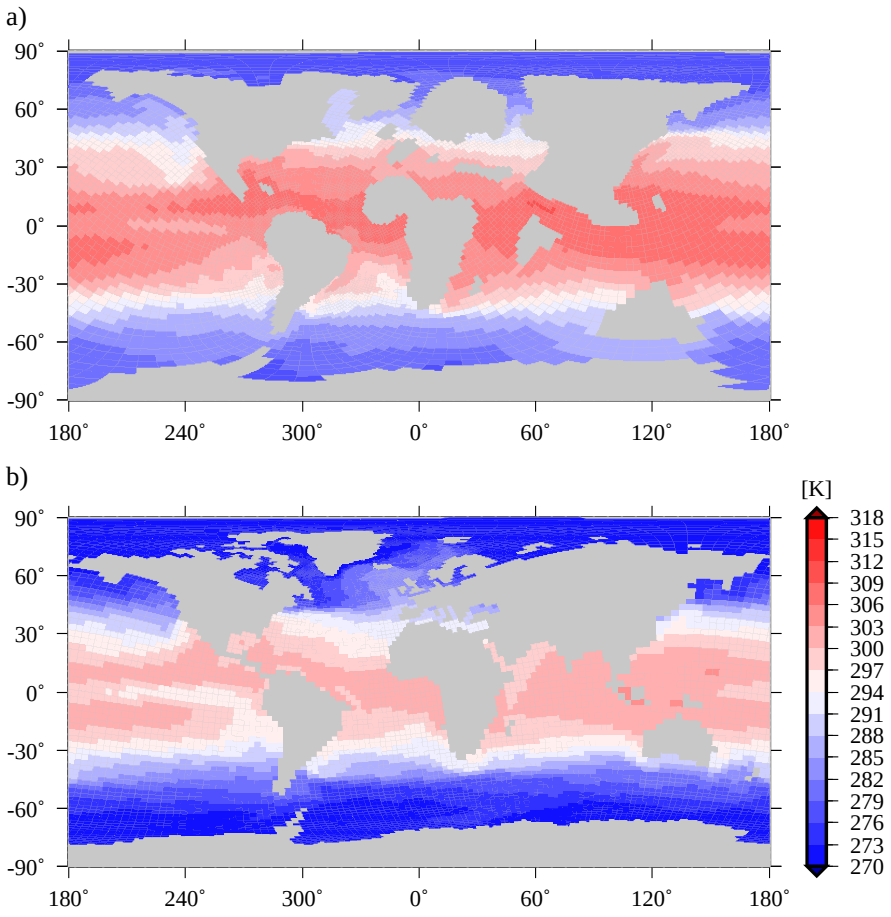

Figure 4.6: Sea surface temperature (uppermost 12 m) averaged over the last 200 years for (a) PE, and (b) PR.

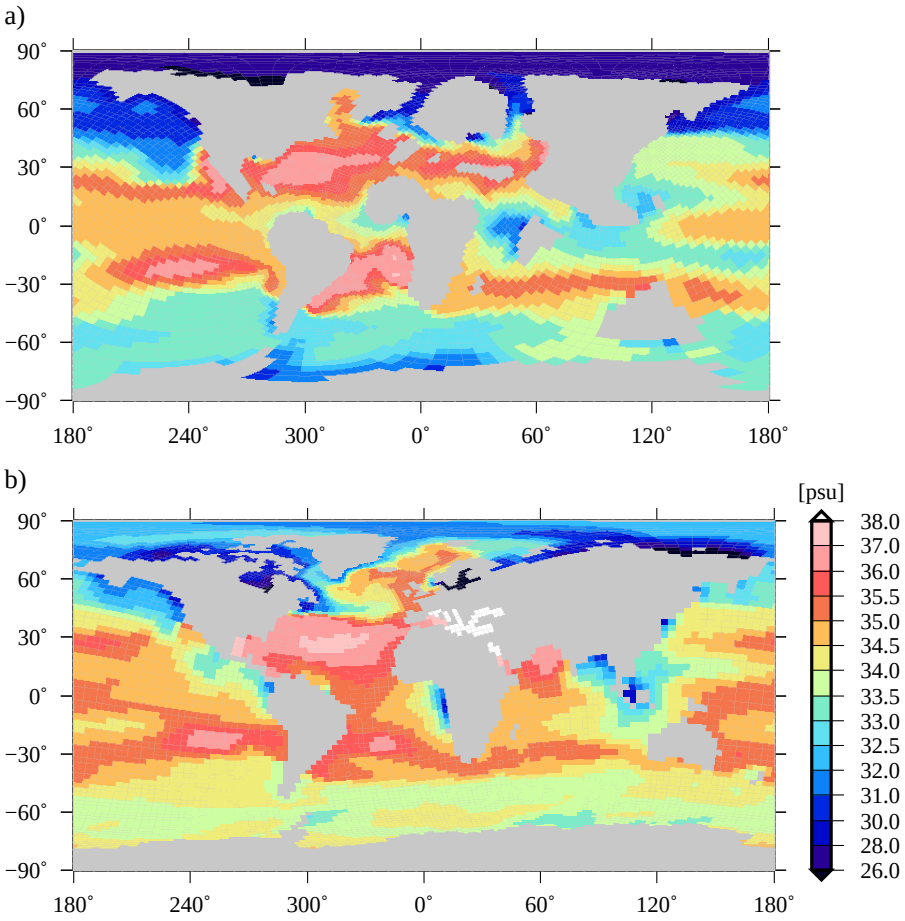

Figure 4.7: Sea surface salinity (uppermost 12 m) averaged over the last 200 years for (a) PE, and (b) PR.

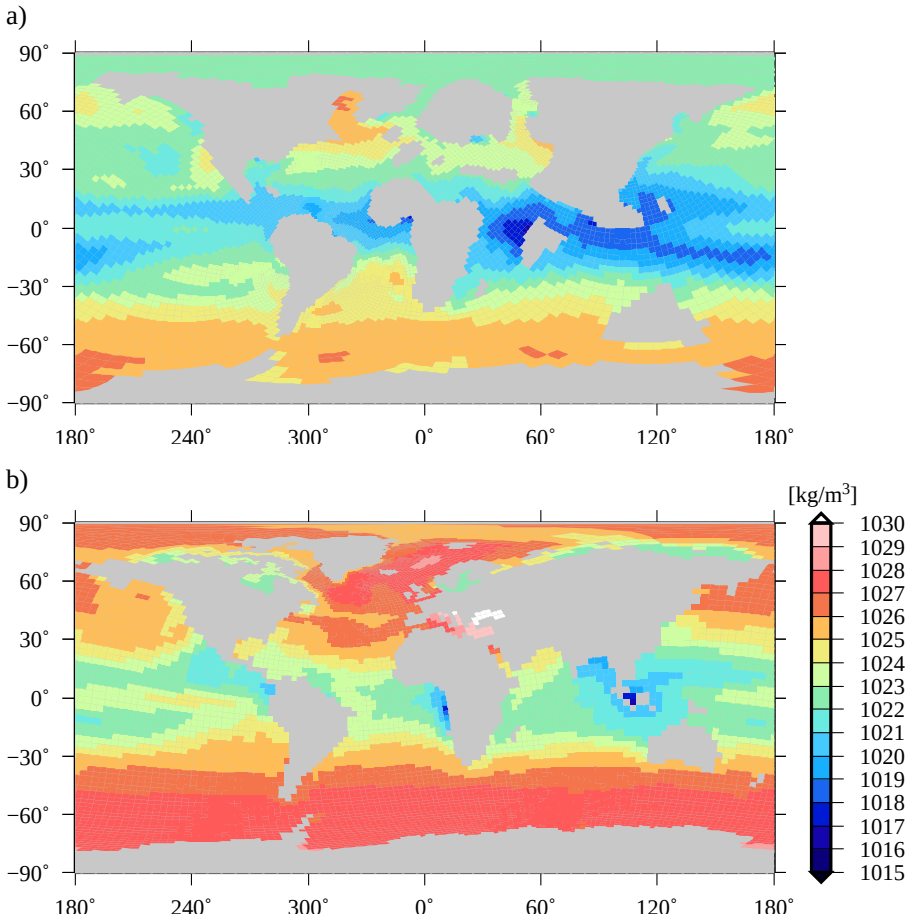

Figure 4.8: Density of the surface water (uppermost 12 m) averaged over the last 200 years for (a) PE, and (b) PR.

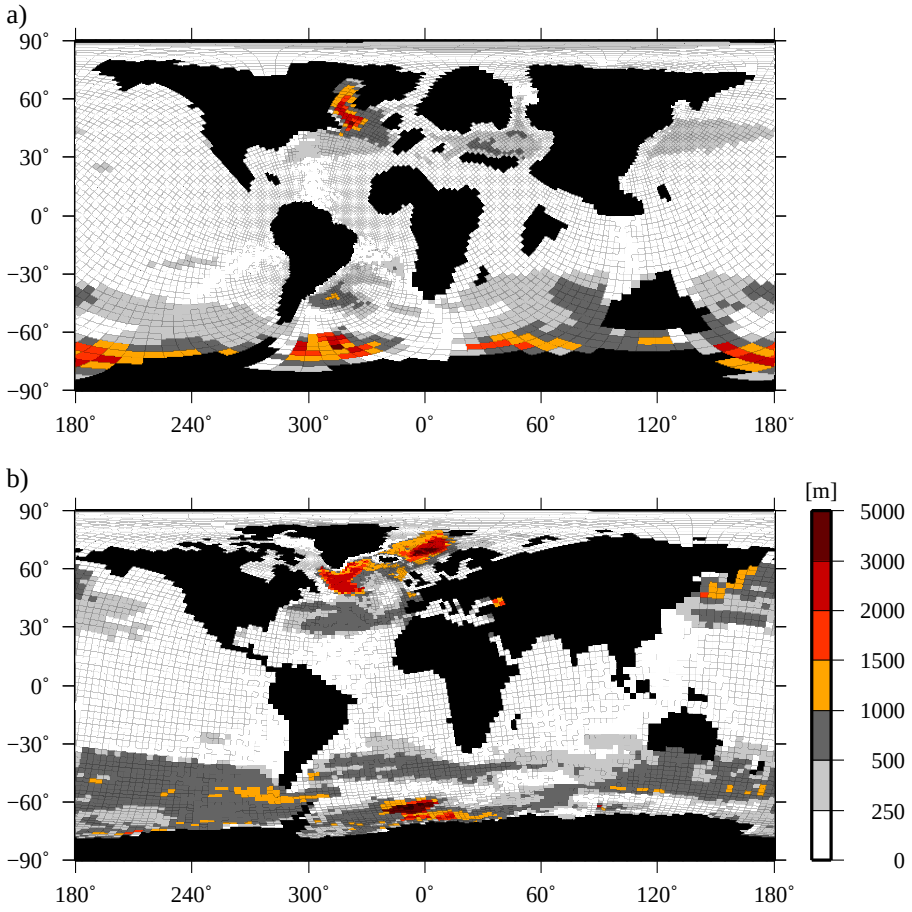

Figure 4.9: Maximum convective depth during the last 200 years of (a) PE, and (b) PR.

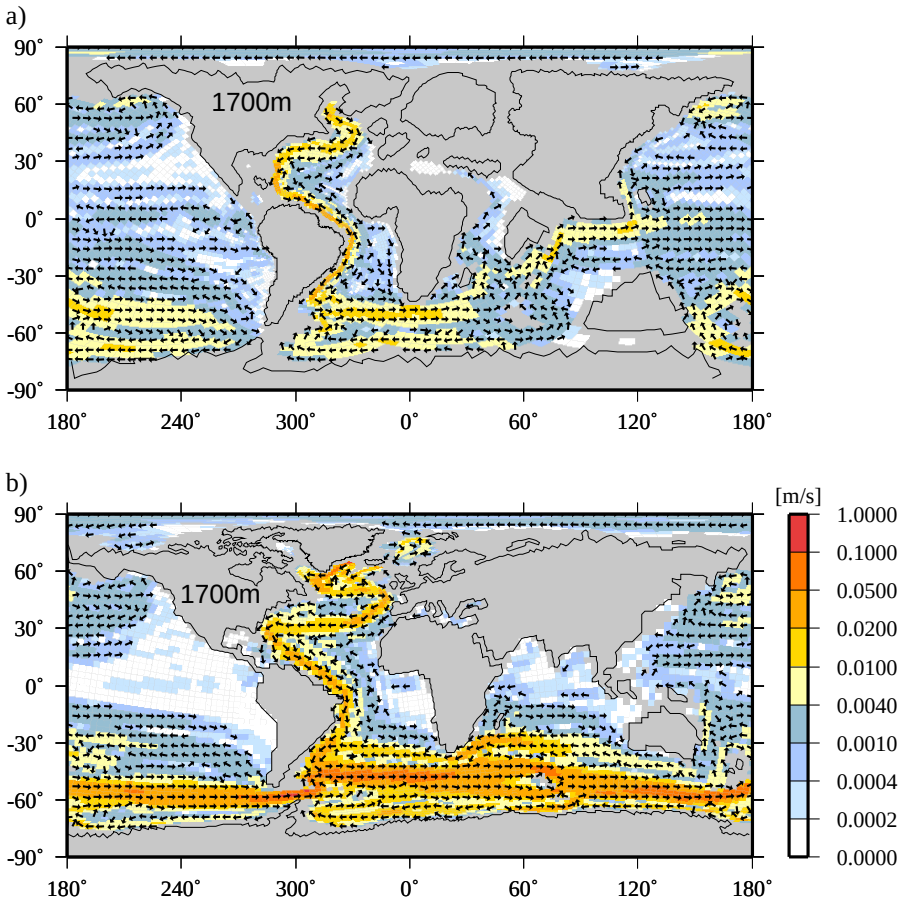

Figure 4.10: Horizontal velocity at 1700 m depth averaged over the last 200 years of (a) PE, and (b) PR; for readability, the velocity vectors are interpolated onto a coarse regular grid; background colors indicate the magnitude of the velocity.

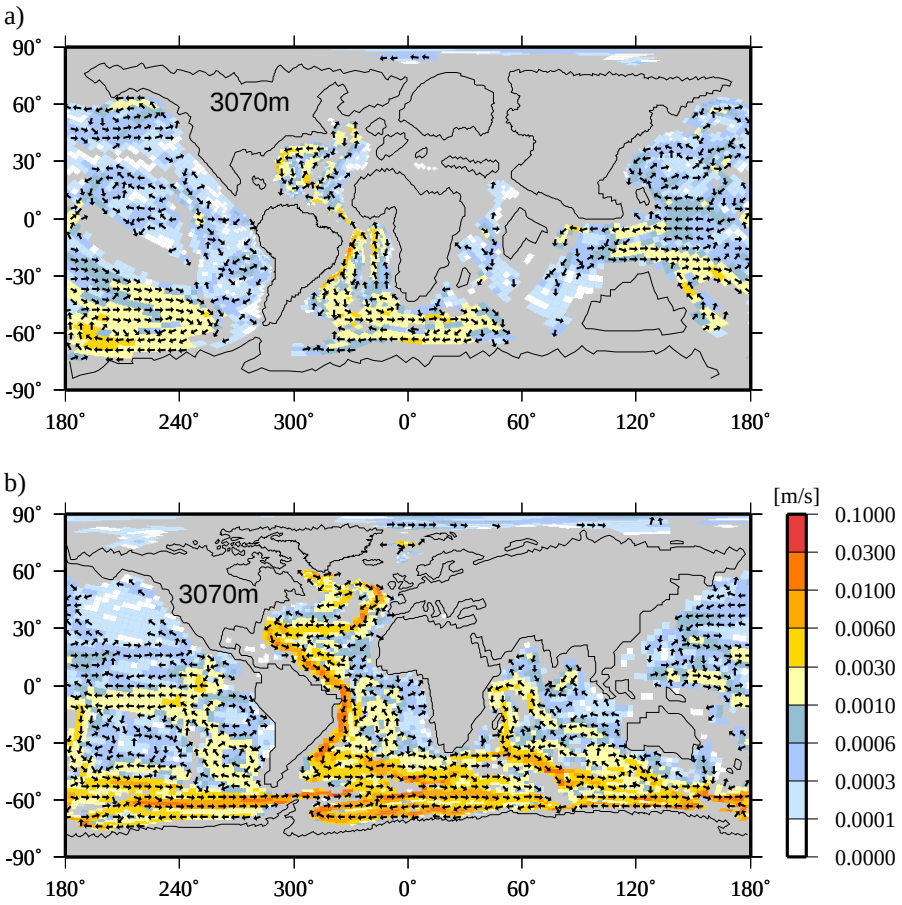

Figure 4.11: Horizontal velocity at 3070 m depth averaged over the last 200 years of (a) PE, and (b) PR; for readability, the velocity vectors are interpolated onto a coarse regular grid; background colors indicate the magnitude of the velocity.

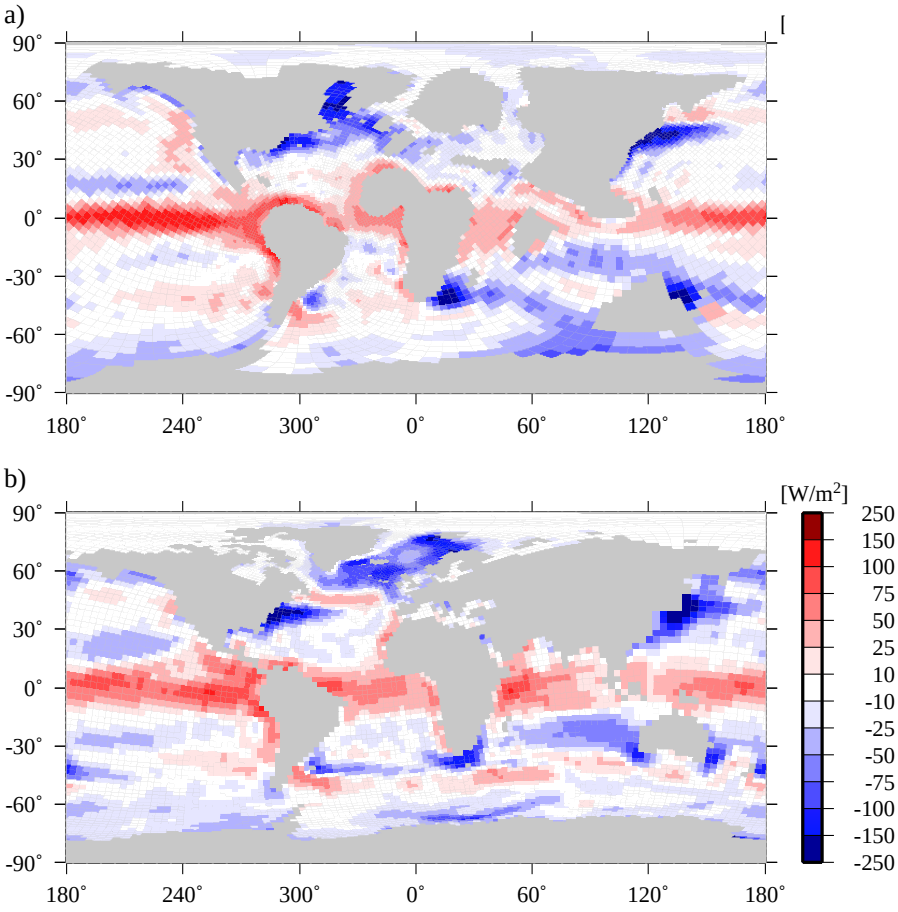

Figure 4.12: Ocean heat uptake averaged over the last 200 years for (a) PE, and (b) PR.

4.3 Sensitivity of the MOC to atmospheric pCO_2

In this section, we study the sensitivity of the PE MOC to a variation of the atmospheric pCO_2. The respective experimental setup is described in Section 3.1.2.

In PE3, we increase pCO_2 from 560 to 840 ppm within 40 years. In response to this increase, the NADW formation rate decreases from about 15 Sv to less than 10 Sv within 200 years, before it recovers to 12 Sv during the subsequent 700 years (Figure 4.13a). Moreover, the NADW formation becomes more shallow in PE3 compared to PE2 (Figures 4.4a and 4.14). While the southward NADW flow occurs between 800 and 3000 m depth in PE2, it occurs between 800 and 2000 m depth in PE3. Consistent with the shallower overturning, the maximum depth of convection in the proto-Labrador Sea is reduced in PE3 compared to PE2 (Figure 4.15a compared to Figure 4.9a). The southern hemisphere overturning in PE3 becomes weaker and shallower (Figure 4.13b-d). The globally integrated MOC at 67.5° S and 1085 m depth decreases from about 10 Sv to less than 3 Sv within a few decades. While Southern Ocean deep water sinks to depths of more than 2000 m in PE2 (Figure 4.4a), it only sinks to about 1000 m in PE3 (Figure 4.14). However, the response in the South Pacific differs from the response in the South Atlantic and Indian Ocean. While the South Pacific overturning seems to remain shut down, the South Atlantic and Indian Ocean deep water formation seems to slowly recover from its initial, fast shutdown (Figure 4.13c). The South Atlantic and Indian Ocean overturning also shows increasing temporal variability during its recovery. This indicates that the actual long-term behaviour of the deep water formation in the South Atlantic and Indian Ocean in PE3 may be somewhat similar to the oscillatory long-term behaviour in PE2. However, the locations of deep convection in the South Atlantic and Indian Ocean during the last 200 years of PE3 differ from those during the last 200 years of PE2. In particular, convection at the Antarctic coastline south of Africa is deeper in PE3 than in PE2. This deeper convection in PE3 is associated with a larger oceanic heat release to the atmosphere compared to PE2 (Figure 4.18b compared to Figure 4.12a). This indicates that the amplification of the PE3-PE2 SST difference at the Antarctic coastline south of Africa (Figure 4.16a) is caused by enhanced convection in PE3. Note that the largest reconstructed SST increase (Thomas et al. 2002) is also situated in that area. However, remember that the South Atlantic and Indian Ocean deep water formation especially in PE2 exhibits a large centennial variability. We have not yet tested these results against that temporal variability.

As described in Chapter 3, the pCO_2 increase to 1120 ppm in PE4 leads to a runaway climate. In that runaway climate, the Southern Ocean deep water formation is shut down entirely after a few decades (Figure 4.13b-d). The sinking in the North Atlantic decreases more or less steadily, until it shuts down abruptly about 400 years after the pCO_2 stabilisation. A closer look reveals that the MOC at 42.5° N and 740 m depth not only decreases to zero, but becomes slightly negative (Figure 4.17a). The North

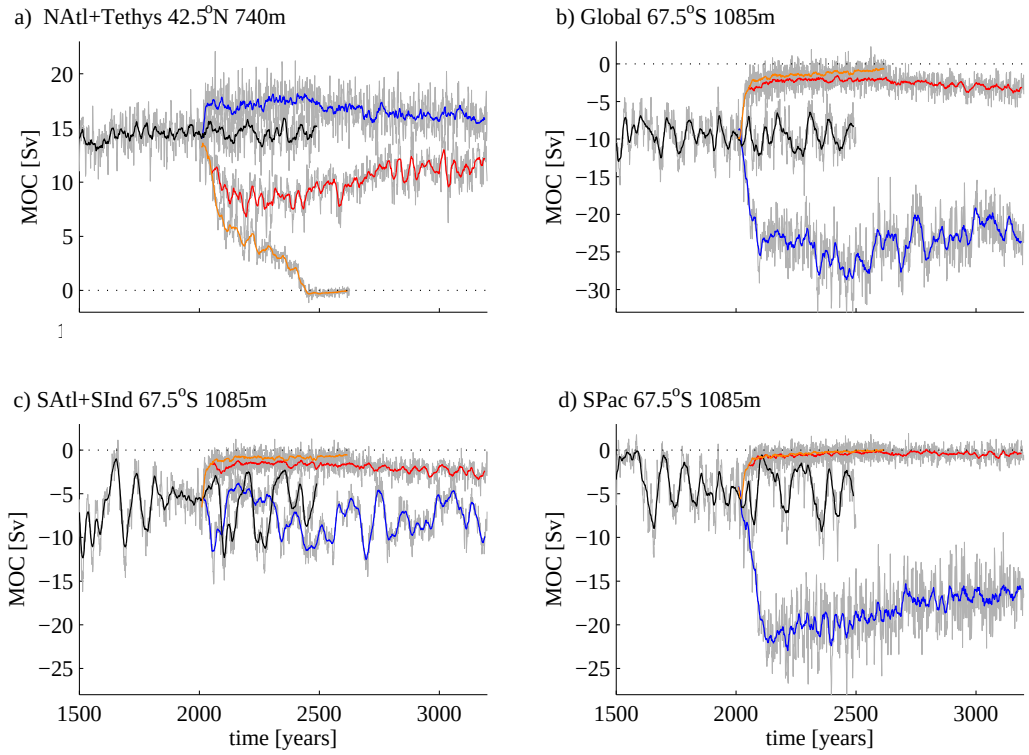

Figure 4.13: Time series of the meridional overturning circulation (MOC) for (a) 42.5° N and 740 m depth integrated over the North Atlantic and Tethys, (b) at 67.5° S and 1085 m depth integrated over the global domain, (c) at 67.5° S and 1085 m depth integrated over the South Atlantic and Southern Indian Ocean, and (d) at 67.5° S and 1085 m depth integrated over the South Pacific basin for PE1 (blue), PE2 (black), PE3 (red), and PE4 (orange).

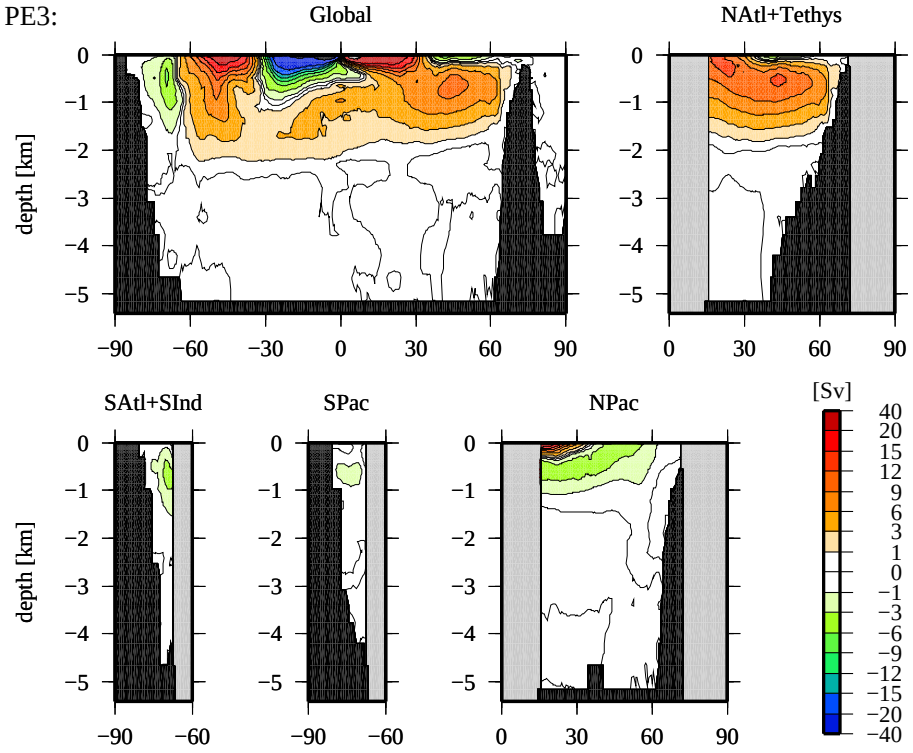

Figure 4.14: Meridional overturning circulation (MOC) during the last 200 years of PE3 for the global ocean (Global), the North Atlantic and Tethys (NAtl+Tethys), the South Atlantic and Indian Ocean (SAtl+SInd), the South Pacific (SPac), and the North Pacific (NPac). Contour intervals are as indicated in the color scale; positive values correspond to clockwise circulation as viewed from reader's perspective.

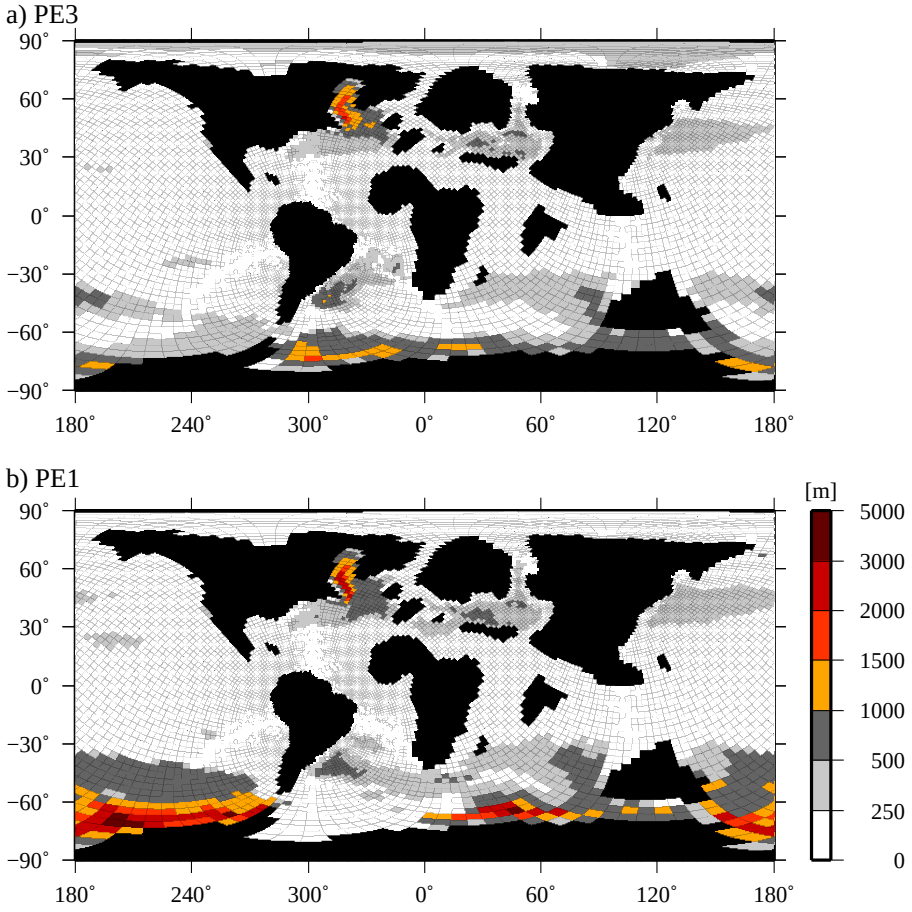

Figure 4.15: Maximum convective depth during the last 200 years of (a) PE3, and (b) PE1.

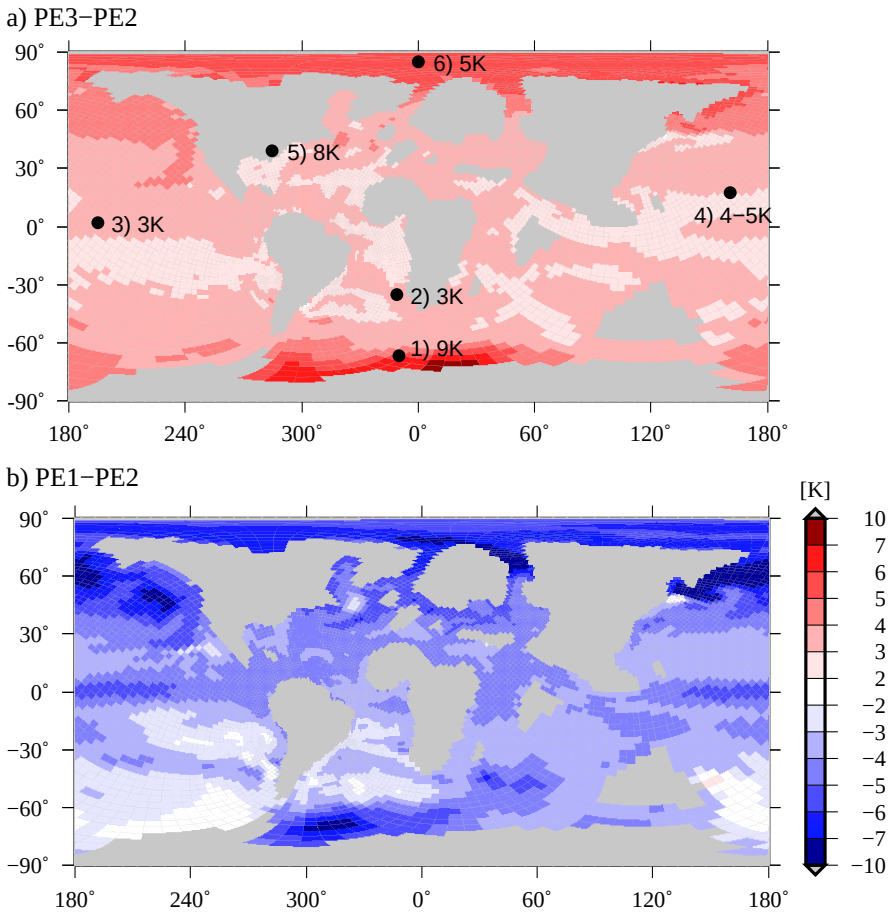

Figure 4.16: (a) Annual mean PE3-PE2 sea surface temperature (SST) difference; as in Figure 3.3 of Chapter 3, black dots indicate the paleo-locations for temperature reconstructions by 1) Thomas et al. (2002, based on $\delta^{18}O$), 2) and 3) Tripati and Elderfield (2004, based on Mg/Ca ratios assuming the Mg/Ca ratio of seawater to be 5.15 mmol/mol), 4) Zachos et al. (2003, based on TEX_{86}), 5) Zachos et al. (2006, based on TEX_{86}), and 6) Sluijs et al. (2006, based on TEX_{86}); the numbers indicate the reconstructed SST increase during the PETM. (b) Annual mean PE1-PE2 SST difference. SST differences computed from the last 200 years of each simulation.

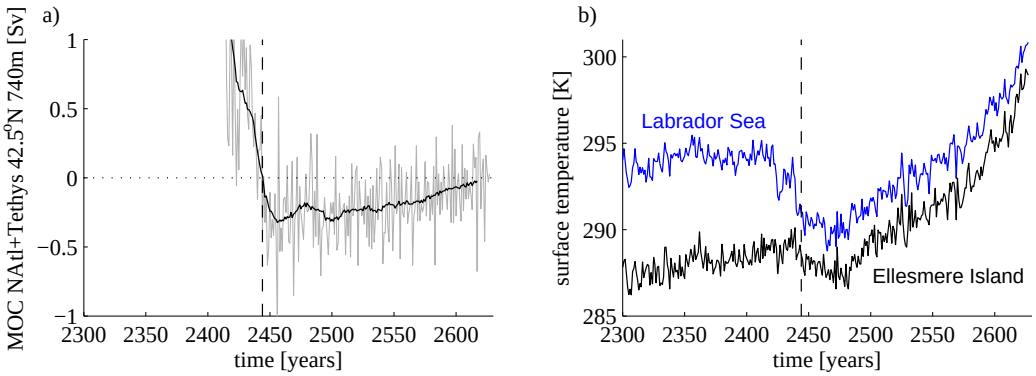

Figure 4.17: (a) Zooming into the PE4 MOC time series from Figure 4.13a (at 42.5° N and 740 m depth integrated over the North Atlantic and Tethys). (b) Time series of the annual mean sea surface temperature in the central Labrador Sea (blue, 65° N 322.5° E), and the annual mean land surface temperature on Ellesmere Island (black, 72° N 315° E); the vertical dashed lines indicate the change of sign of the MOC in year 2444.

Atlantic sinking turns into a weak North Atlantic upwelling. Sinking and convection in the Labrador Sea involve an oceanic release of large amounts of heat to the atmosphere (Figure 4.12a). The shutdown of Labrador Sea sinking is associated with a shutdown of the oceanic heat release (Figure 4.18). The change in the overturning circulation from sinking to weak upwelling during the runaway effect in PE4 leads to a cooling of the Labrador Sea surface by more than 4 K within less than 50 years, and explains the sudden, transient drop of the global mean surface temperature around the year 2444 during PE4 as seen in Figure 3.2. This cooling in response to the NADW shutdown is not only seen at the sea surface. Also, for example, the annual mean land surface temperatures on Ellesmere Island —where Estes and Hutchinson (1980) found the PE alligator remains— cool by about 2 K. At the end of PE4, the meridional overturning below 1000 m depth basically stands still (Figure 4.19).

In PE1, the experiment with pCO_2 decrease from 560 to 280 ppm, the North Atlantic MOC becomes stronger by about 2 Sv (Figure 4.13a), and it significantly deepens (Figure 4.20). The integrated South Atlantic plus Indian Ocean deep water formation hardly changes in PE1 compared to PE2 (Figure 4.13c). However, we find that convection in the proto-Weddell Sea completely shuts down in PE1 (Figure 4.15b). This indicates that the integrated South Atlantic and Indian Ocean sinking originates solely from the Southern Indian Ocean in PE1. This shutdown of the proto-Weddell Sea deep water formation is associated with a shutdown of the oceanic heat release to the

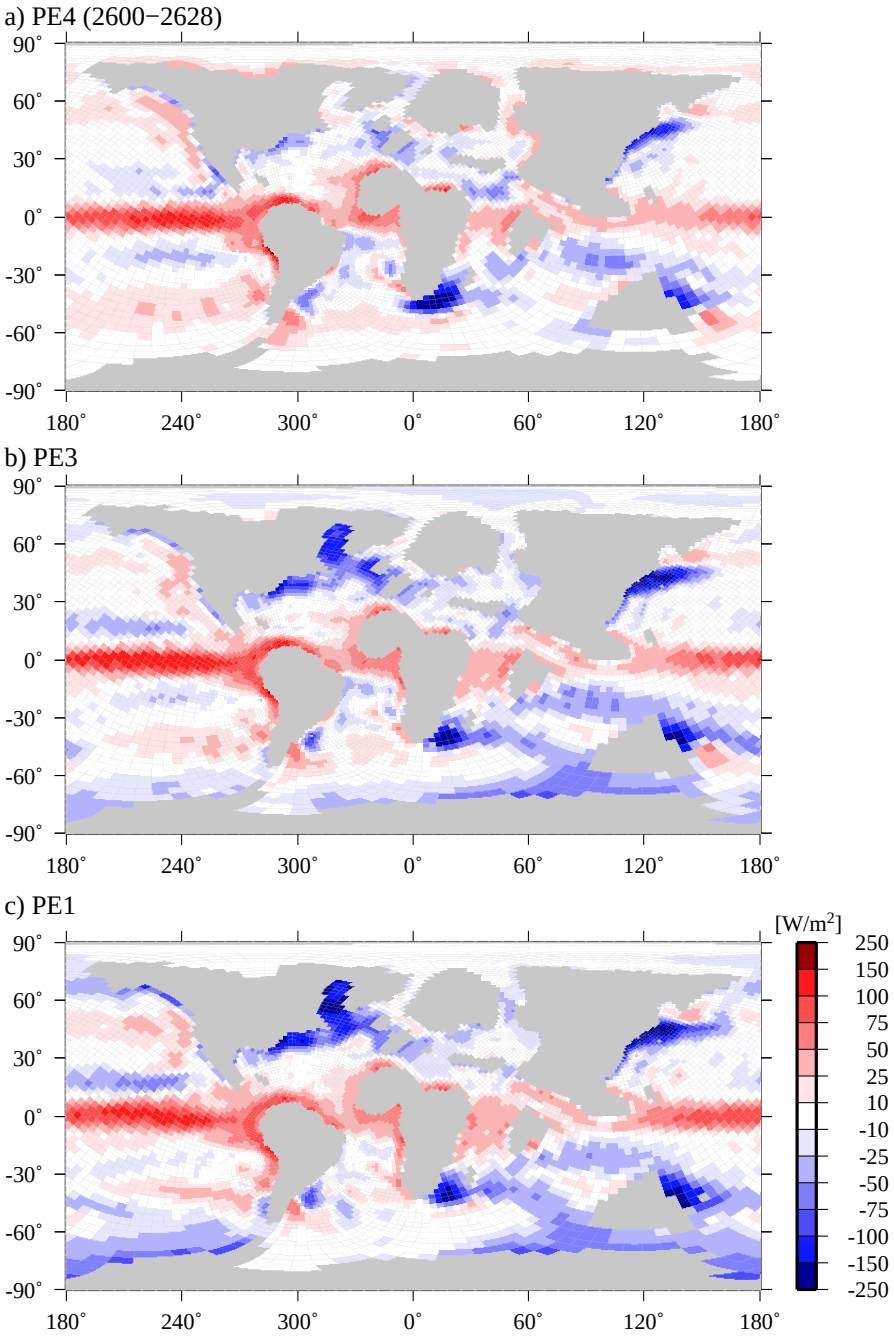

Figure 4.18: Ocean heat uptake for (a) PE4 (average of years 2600 to 2628), (b) PE3 (average of years 3000 to 3199), and (c) PE1 (average of years 3000 to 3199).

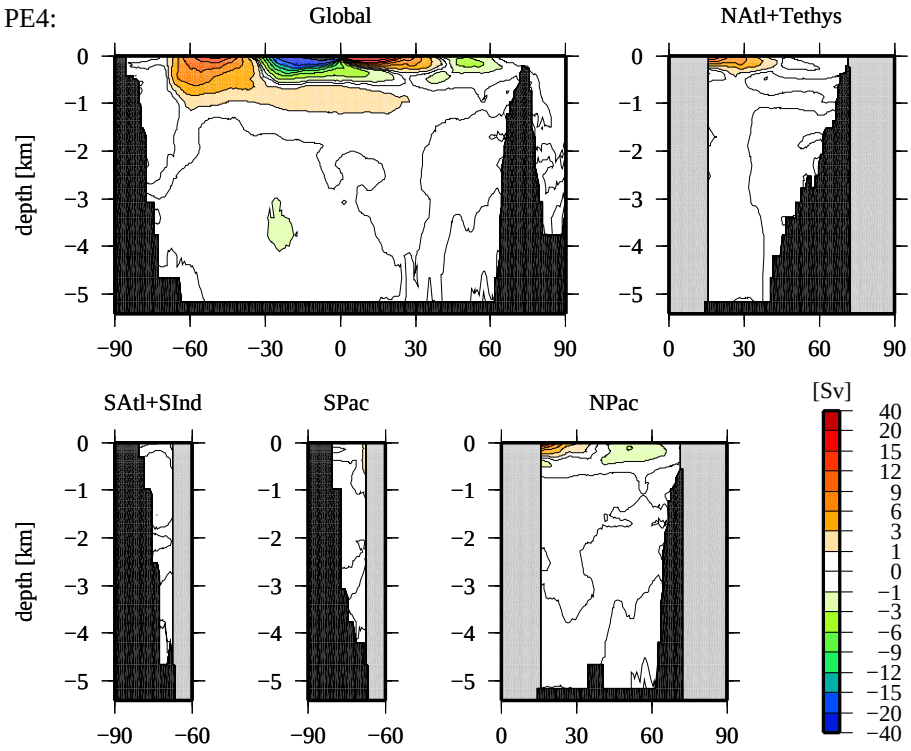

Figure 4.19: Meridional overturning circulation (MOC) averaged over the years 2600 to 2628 of PE4 for the global ocean (Global), the North Atlantic and Tethys (NAtl+Tethys), the South Atlantic and Indian Ocean (SAtl+SInd), the South Pacific (SPac), and the North Pacific (NPac). Contour intervals are as indicated in the color scale; positive values correspond to clockwise circulation as viewed from reader's perspective.

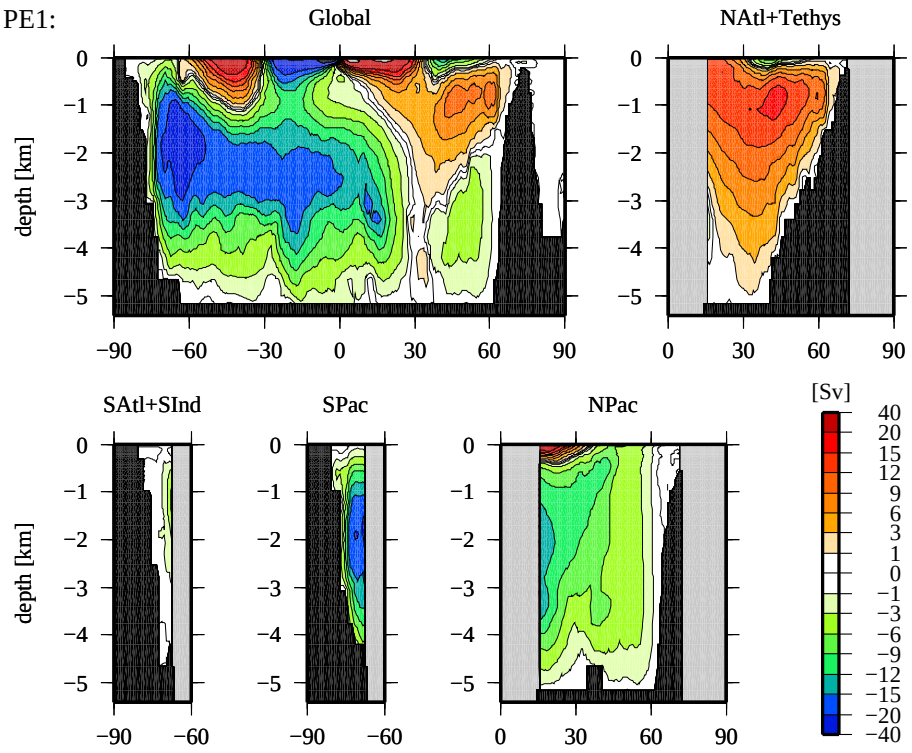

Figure 4.20: Meridional overturning circulation (MOC) during the last 200 years of PE1 for the global ocean (Global), the North Atlantic and Tethys (NAtl+Tethys), the South Atlantic and Indian Ocean (SAtl+SInd), the South Pacific (SPac), and the North Pacific (NPac). Contour intervals are as indicated in the color scale; positive values correspond to clockwise circulation as viewed from reader's perspective.

atmosphere (Figure 4.18c), and an amplification of the proto-Weddell Sea surface temperature decrease during PE1 (Figure 4.16b). In the South Pacific, decreasing pCO_2 causes a transition from sporadic, weak deep water formation to strong, steady deep water formation (Figure 4.13d). This strong South Pacific sinking is associated with an increased oceanic heat release to the atmosphere in PE1 compared to PE2 (Figure 4.12c compared to Figure 4.12a). Similar to the warm surface water in the Labrador Sea because of deep water formation, the South Pacific SSTs in PE1 are relatively high; this explains the small South Pacific SST decrease in PE1 compared to PE2 (Figure 3.3b). After its formation, the South Pacific deep water in PE1 flows northward between a depth of 2000 m and the ocean bottom (Figure 4.20), mostly as a deep western boundary current (Figure 4.21). Note that this deep, northward western boundary current makes a detour into the Indian Ocean.

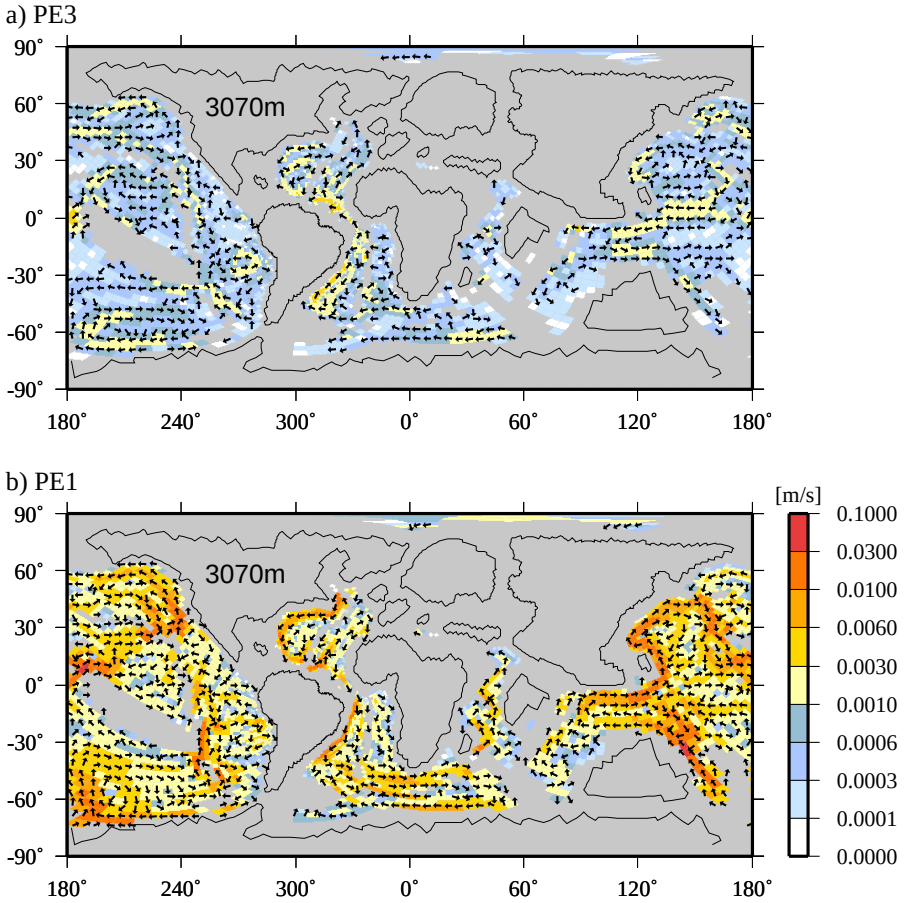

Figure 4.21: Horizontal velocity at 3070 m depth averaged over the last 200 years of (a) PE3, and (b) PE1; for readability, the velocity vectors are interpolated onto a coarse regular grid; background colors indicate the magnitude of the velocity.

4.4 Ocean circulation reconstructions

One way to obtain information about the PE ocean circulation is to study carbon isotope ratios from benthic foraminifera. Benthic foraminifera are calcite-shelled zooplankta living at the bottom of the ocean. The δ^{13}C composition of their shell reflects the isotopic composition of the surrounding water at the time of calcification. Since deep water becomes isotopically more negative with time due to the rain of organic material that progressively adds ^{12}C, more negative benthic foraminiferal δ^{13}C indicates 'older' deep water (e.g., Corfield 1994).

Miller et al. (1987) showed evidence from benthic foraminiferal δ^{13}C that the *western* Atlantic Newfoundland, American, and Brazil basins (Sites 20, 21, 144, 356, 357, 384) were filled with 'old' bottom water during the late Paleocene, suggesting absense of NADW formation. By contrast, we find NADW formation in all our stable PE climate simulations. However, the NADW formation in our simulation becomes shallower for larger CO_2 concentrations. This indicates that deep western Atlantic waters may have been poorly ventilated despite North Atlantic sinking. Miller et al. (1987) also found evidence that the *eastern* Atlantic Cape Basin (Site 524) was filled with 'young' bottom water. They suggested that this 'young' bottom water originated from the Antarctic, since (1) the 'old' bottom water in the western Atlantic indicated that the North Atlantic/Arctic was not the source region, and (2) oxygen isotope comparisons supported a high-latitude source region precluding the Tethys. The 'young' eastern Atlantic bottom water is consistent with our simulated deep convection in the proto-Weddell Sea in PE2, and the northward deep water track in the eastern Atlantic at about 3000 m depth (Figures 4.9a and 4.11a).

Tripati and Elderfield (2005) investigated benthic foraminiferal δ^{13}C from the tropical North Pacific (Site 1209, Shatsky Rise) and the subtropical eastern South Atlantic (Site 527, Walvis Ridge). For the late Paleocene, they inferred that the South Atlantic was more ventilated than the North Pacific. This is consistent with our simulation. We find deep convection in the proto-Weddell Sea, while there is neither convection nor sinking in the North Pacific. Actually, except for PE1, the North Pacific is not even ventilated by the MOC associated with the southern hemisphere sinking (Figures 4.4a and 4.14). During the latest Paleocene, prior to the CIE associated with the PETM, intermediate waters exhibited a warming, the South Atlantic became less ventilated, and the North Atlantic became slightly more ventilated. Tripati and Elderfield (2005) suggested that, during the PETM, warm and saline deep water was formed in the North Pacific. According to our simulations, increased pCO_2 leads to a reduced, shallower MOC and to reduced convection at least in the North Atlantic, bottom water in the North Atlantic should become less ventilated.

Nunes and Norris (2006) compared four South Atlantic and Southern Ocean δ^{13}C records (Sites 525, 527, 690, 738) to three North Atlantic δ^{13}C records (Sites 401, 1051,

ALM). They found that, for the time period before the PETM, the average δ^{13}C of the southern sites was about 0.15‰ higher than the average δ^{13}C of the northern sites. From this difference, they concluded that deep water most likely flew northward in the Atlantic. In contrast to this conclusion by Nunes and Norris (2006), the largest Atlantic deep water flow in our simulation is southward (Figure 4.10). However, the simulated southward track is a western boundary current, while the two South Atlantic sites with high δ^{13}C used by Nunes and Norris (2006) are located on the Walvis Ridge in the *eastern* Atlantic. Such high δ^{13}C (i.e. 'young' water) in the eastern Atlantic would again be in line with the simulated proto-Weddell Sea sinking and northward deep water track in the eastern Atlantic around 3000 m depth (Figure 4.11).

Nunes and Norris (2006) found that the sign of the δ^{13}C difference between the northern and southern sites changed during the PETM. They concluded that the ocean circulation may have switched from southern sinking before the PETM to northern sinking during the PETM. Our simulations indicate that increasing pCO_2 (mimicking the onset of the PETM) leads to a generally weaker MOC and to shallower convection. Hence, according to our simulations, from the broad perspective of southern versus northern hemisphere sinking as discussed by Nunes and Norris (2006), the δ^{13}C gradient should not have changed. However, the comparison of the last 200 years of PE1, PE2, and PE3 suggests that, locally, the South Atlantic may have become slightly more ventilated in response to a pCO_2 increase (remember 1. proto-Weddell Sea convection in PE2, but not in PE1, and 2. small area at Antarctic coastline south of Africa with increased convection in PE3 compared to PE2). If at all, this would suggest a change of the δ^{13}C gradient in the opposite direction of that inferred by Nunes and Norris (2006).

Thomas et al. (2003) used fish tooth Neodymium (Nd) isotopic records from eight DSDP and ODP sites to reconstruct the PE deep water circulation. Neodymium mainly originates from continental weathering and runoff. After its drainage into the ocean as dissolved and suspended material, Nd remains in the ocean for about 1000 years. Due to this short residence time relative to the mixing time of the oceans (several 1000 years), Nd can be used to classify different deep water masses. Fish teeth acquire their high Nd concentrations during a diagenetic reaction at the sediment/water interface. Thus Nd isotopes from fish teeth reflect the isotopic composition of the overlying bottom water. Thomas et al. (2003) found that fish teeth from the Atlantic, Southern Ocean, and Indian Ocean (Sites 549, 401, 1051, 527, 690, 213) were characterised by relatively non-radiogenic Nd, while fish teeth from the Pacific (Site 865) were characterised by more radiogenic Nd. They concluded that the Pacific had a different source of Nd than the Atlantic, Indian, and Southern Ocean, and suggested that the Atlantic, Indian, and Southern Ocean were bathed by a common water mass. They argued that the North Atlantic as a source of the common deep water was unlikely, since (1) the Labrador Sea had just begun opening, and (2) δ^{18}O reconstructions indicate that the surface water in

the Southern Ocean was much colder than in the North Atlantic. Therefore, Thomas et al. (2003) suggested that deep water was formed in the Southern Ocean before and during the PETM. However, in our numerical simulation, we find NADW formation in the Labrador Sea *even though* SSTs in the Labrador Sea are up to 10 K warmer than in the Southern Ocean. And actually, our simulations indicate that the SSTs in the Labrador Sea were so high (at least partly) *because* of deep water formation.

4.5 Discussion and conclusions

In our control simulation with 560 ppm pCO_2, which is the simulation that best matches reconstructed pre-PETM surface temperatures, we find North Atlantic Deep Water (NADW) formation in the proto-Labrador Sea and a southward western boundary current at about 800 to 3000 m depth. Deep water in the southern hemisphere forms in centennial flushes in the South Atlantic and Indian Ocean, and in the South Pacific. In addition to the deep, southward, western boundary current in the Atlantic, we also find a deep, northward transport in the eastern Atlantic at about 3000 m depth.

Irrespective of the CO_2 concentration, all our stable solutions exhibit sinking and deep convection in the proto-Labrador Sea. Only during the unstable simulation with 1120 ppm pCO_2 do we find a shutdown of the sinking. This shutdown immediately leads to a cooling not only of the proto-Labrador Sea, but also, for example, at the paleo-location of Ellesmere Island. This indicates that the Labrador Sea and Ellesmere Island in our stable simulations would be colder, if there was no NADW formation in the proto-Labrador Sea. We speculate that deep water formation in the proto-Labrador Sea contributed to the living conditions for alligators on Ellesmere Island.

Increasing pCO_2 from 560 to 840 ppm leads to a generally weaker, shallower convection and weaker, shallower meridional overturning. Our analysis indicates that increasing pCO_2 may have led to enhanced convection at the coastline of Antarctica south of Africa, increased ocean heat release, and a local amplification of the warming in the proto-Weddell Sea, consistent with a large reconstructed SST increase. This result indicates that changes in the ocean circulation can lead to large, local differences in the SST response to a variation of atmospheric pCO_2. In turn, the regional patterns of SST changes during the PETM may contain valuable information about the ocean cirulation changes. We propose that SST changes derived from proxy data may be used as an indicator for ocean circulation changes.

Assume that the long-term behaviour of PE1 resembles the pre-PETM climate state (although the PE1 high-latitudes are probably too cold). Moreover, assume that a pCO_2 increase to 560 ppm starting from PE1 will finally yield PE2 again. Then, our simulations indicate that the PETM may have been associated with the onset of deep convection in the proto-Weddell Sea. We do not know whether such an onset of deep water formation would lead to bottom water warming. However, even if such a change

did lead to bottom water warming, the change of the deep water formation would have a relatively small areal extent. The amount of methane that could have been released in response to this ocean circulation change is probably quite small. We conclude that, according to our simulations, ocean circulation changes did not lead to the dissolution of large amounts of methane hydrates.

The coupled NCAR CCSM Eocene simulation described by Huber et al. (2003) showed a different meridional overturning structure. They also found sinking in the North Atlantic (about 15 Sv). But their simulation did not show any deep convection nor sinking in the southern hemisphere. Instead, they found sinking in the North Pacific to about 2000 m depth. This difference may be related to differences in the bathymetry between the CCSM Eocene setup and our PE setup. In the setup of Huber et al. (2003), the Arctic Ocean is completely isolated, while our Arctic Ocean is connected to the Atlantic, to the Tethys, and to the Pacific. The surface-water of the Arctic Ocean in our simulations has a very low salinity. This low-salinity water is transported southward through the Bering Strait into the North Pacific. We speculate that this fresh-water input has the potential to inhibit North Pacific deep water formation in our simulations. Whether or not the Bering Strait was closed during the PE is currently under discussion (Winguth, personal communication).

The ocean GCM control simulation described by Bice and Marotzke (2002) showed southern hemisphere overturning of about 60 Sv, and a northern hemisphere overturning of about 3 Sv. Introducing a land bridge between proto-Britain and Greenland as a barrier to North Atlantic flow led to a northern hemisphere overturning of about 20 Sv in their runs. The bathymetry we use does not have that land bridge between Britain and Greenland, but we still find NADW formation of about 15 Sv. Moreover, our simulations do not support the very strong southern hemisphere overturning.

Bice and Marotzke (2002) found a sudden onset of sinking in their North Pacific in response to multiplying their prescribed moisture flux (precipitation minus evaporation) by 1.6. In our simulations, the strength of the hydrological cycle is modified in response to the pCO_2 variation. However, we do not find North Pacific deep water formation. Because of uncertainties in the boundary conditions, for example, regarding the Bering Strait or the land bridge between proto-Britain and Greenland, and because we do not know whether the PE climate model solutions as described here are unique (there may be more than one long-term solution to our PE climate model setup for each CO_2 concentration), we cannot rule out the hypothesis that an ocean circulation switch as suggested by Bice and Marotzke (2002) caused the methane hydrate dissociation. But our simulations do not support that hypothesis. Moreover, we note that the multiplication of P-E by 1.6 is large compared to the hydrological cycle changes in our stable pCO_2 sensitivity experiments (Figure 4.22).

We note that our solution of the PE ocean circulation is relatively similar to the present-day circulation (or, to PR). For example, we find NADW formation in PE

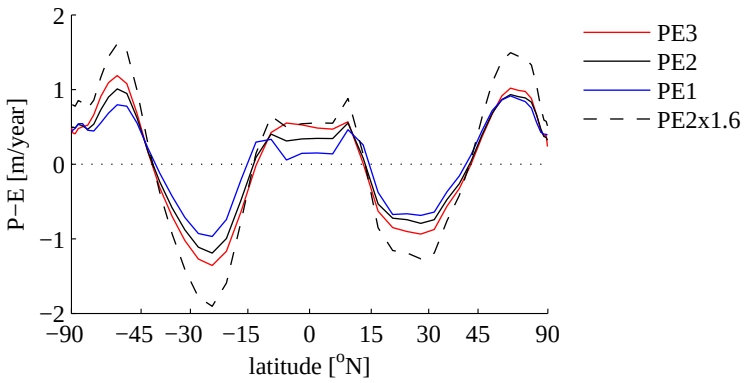

Figure 4.22: Zonal mean annual mean precipitation minus evaporation (P-E) computed from the last 200 years of PE3 (red), PE2 (black), and PE1 (blue); the dashed line indicates the zonal mean P-E field of PE2 multiplied by 1.6 to imitate the 60 % increase at which Bice and Marotzke (2002) found the onset of North Pacific sinking.

despite the open Central American Isthmus. Maier-Reimer et al. (1990) found a shutdown of the NADW formation in response to an opening of the Central American Isthmus in a present-day setup of an ocean GCM. This illustrates that the described PE ocean circulation solution is a result of the combination of all boundary condition differences (in this case also including the atmospheric forcing). The various PE-PR boundary condition differences interact, and it is not always meaningful to isolate the effect of a single difference in boundary conditions.

The inhomogeneous vertical and zonal structure of the convection and meridional overturning in the Atlantic in our simulations challenges previous conclusions from 'deep water age' reconstructions, which are based on single, local ocean drilling sites. Nunes and Norris (2006) inferred southern hemisphere deep water formation from carbon isotope data. We argue that the relatively shallow NADW-track in combination with South Atlantic convection and a northward flow of Antarctic bottom water in the eastern Atlantic, in other words, co-existing northern and southern hemisphere deep water formation, may also be consistent with the carbon isotope records. Our simulations do not show any increase in deep water formation in the northern hemisphere in response to increased pCO_2. Hence, our simulations do not support the notion of Nunes and Norris (2006) that the onset of the PETM was associated with a switch from southern hemisphere to northern hemisphere deep water formation.

Chapter 5

Conclusions and outlook

5.1 Conclusions

To conclude this thesis, we answer the questions posed in the introduction (Chapter 1).

(1) Can we simulate the warm PE climate with its low equator-to-pole temperature gradient using ECHAM5/MPI-OM?

We are getting close. To our knowledge, we have obtained the first coupled PE simulation with moderate greenhouse gas forcing that is warm enough at high latitudes to keep the poles free from sea ice, while reasonably matching the lower-latitude SST reconstructions. However, if we take the SST proxy data by Sluijs et al. (2006) at face value, the simulated Arctic surface temperature is still too cold.

(2) What mechanisms may have led to the warm PE climate and the low temperature gradient?

To answer this question, we compare the PE climate simulation to a pre-industrial reference (PR) using a zero-dimensional energy balance model as a diagnostic tool. We find that, according to our simulations, the warm PE climate with its low equator-to-pole temperature gradient was mostly due to a smaller (compared to PR) longwave emissivity especially at high latitudes. The global-mean longwave cloud radiative effect in PE does not differ much from that in PR, but we find that the longwave cloud radiative effect may have contributed to the lower equator-to-pole temperature gradient. We attribute most of the emissivity reduction to an increased atmospheric water vapour content in PE compared to PR. The removed glaciers and associated lower Antarctic topography also contributed to the low PE equator-to-pole temperature gradient. Compared to the emissivity changes, the darker surface at high latitudes associated with the lack of glaciers, a relatively dark land surface and vegetation, the lack of sea ice, and the reduction of snow cover had a relatively small effect. The surface albedo effect was diminished by a larger shortwave radiative effect above the darker surface.

According to our model, the zonally integrated meridional heat transport by the atmosphere and the ocean during the PE was not very different from the present-day transport. Actually, our results indicate that the zonally integrated meridional heat transport by the ocean was probably even weaker than at present (confirming the results of Huber and Sloan 2001). However, locally, the ocean heat transport may have been very important. For example, we find North Atlantic Deep Water (NADW) formation in the proto-Labrador Sea, and our results indicate that this NADW formation may have contributed to relatively high surface temperatures — and thus to the living conditions for alligators — on proto-Ellesmere Island.

(3) What was the atmospheric pCO_2 before the PETM / how much greenhouse gas forcing do we need to match the reconstructed PE temperatures?

We find that reducing pCO_2 to 280 ppm starting from the PE control simulation with 560 ppm leads to a global cooling of about 4.7 K, a cooling of up to 11 K in the Arctic, and regrowing sea ice, which is in contrast to proxy data that suggest warm and sea-ice-free high latitudes even before the PETM (Sluijs et al. 2006). Our PE simulation with a CO_2 concentration of 560 ppm is the best equivalent to the reconstructed pre-PETM surface temperatures. We conclude that the pre-PETM atmospheric CO_2 concentration was probably about 500 ppm. Note that the concentrations of other greenhouse gases such as methane or nitrous oxide during the PE are uncertain. In our simulations, we assume pre-industrial values. A different greenhouse gas mix with possibly lower pCO_2 may also lead to a similar PE model-data match.

(4) Does our PE model exhibit a large enough climate sensitivity to support the hypothesis that a methane release caused the PETM?

Yes. According to our model, increasing pCO_2 from 560 ppm to 840 ppm leads to an increase of the global-mean surface temperature by 3.8 K. The warming amounts to about 3 K at low latitudes and up to 5 K at high latitudes and (although at the lower bound) matches the reconstructed surface temperature increase during the PETM at some locations. This pCO_2 increase by 280 ppm is equivalent to the addition of less than 600 Pg C to the atmosphere. Even if the global methane hydrate reservoir was smaller than at present (<2000 Pg C, Buffett and Archer 2004), a total collapse of the hydrate reservoir would leave some space for ocean and biosphere carbon uptake, leaving enough carbon in the atmosphere to explain the warming during the PETM.

Note that a warming by 3.8 K in response to the 1.5-fold pCO_2 increase is equivalent to an equilibrium climate sensitivity of about 6.5 K, suggesting that the PE climate was much more sensitive to pCO_2 than previously simulated by Shellito et al. (2003) and

Winguth et al. (submitted). The analysis of the pCO_2 increase experiment using an EBM reveals that about 2/3 of the warming are due to a reduced longwave emissivity, 1/3 of the warming is due to a reduced planetary albedo. Most of the planetary albedo reduction originates from a reduced cloud cover, surface albedo changes are small because there is no sea ice to be melted (a small reduction of the high-latitude surface albedo originates from decreased snowfall). The longwave cloud radiative effect hardly changes. Thus, most of the emissivity-driven warming is due to the radiative effects of the clear-sky atmosphere. Unfortunately, we cannot distinguish between the longwave radiative effects of the different clear-sky atmospheric compartments. However, assuming that we know the direct radiative forcing of CO_2, we attribute the residual and largest part of the clear sky emissivity-driven warming to the increased atmospheric water vapour content.

Increasing pCO_2 to 1120 ppm leads to a destabilisation of the simulated climate; a runaway effect occurs. We find that almost 1/4 of the warming during the runaway is caused by a reduction of the total cloud cover and the consequent relative warming due to reduced reflection of shortwave radiation by clouds. Our results indicate that most of the residual warming is due to a decrease of the clear sky emissivity. We find that prescribing present-day ozone concentrations may lead to artificial warming in warmer-than-present simulations. However, for now, we have not excluded the possibility that another mechanism (i.e., a mechanism other than artificially high tropospheric ozone) causes the runaway climate for 1120 ppm. Using our GCM model setup, we cannot distinguish between the radiative effect of ozone and the other components of the clear-sky atmosphere. Hence, we cannot rule out that the PE runaway climate is an artefact of unrealistic ozone concentrations. Note that, even if the runaway is not an artefact of overstressed parameterisations, it could still be due to the lack of feedback mechanisms from other Earth system components, for example the lack of vegetation feedbacks.

(5) Can we confirm the hypothesis that an ocean circulation switch triggered the PETM using a coupled GCM?

No. According to our simulations, there was no ocean circulation switch that could have triggered the thermal dissociation of large amounts of methane from marine sediments. In our control simulation with 560 ppm pCO_2, which is the simulation that best matches reconstructed pre-PETM surface temperatures, we find NADW formation in the proto-Labrador Sea and a southward western boundary current at about 800 to 3000 m depth. Deep water in the southern hemisphere forms in centennial flushes in the South Atlantic and Indian Ocean, and in the South Pacific. In addition to the deep, southward, western boundary current in the Atlantic, we also find a deep, northward transport in the eastern Atlantic at about 3000 m depth. Increasing pCO_2 leads to a generally

weaker, shallower meridional overturning circulation. We do not find a switch to North Pacific deep water formation, as suggested by Bice and Marotzke (2002). Moreover, our results indicate that the hydrological cycle change that Bice and Marotzke (2002) applied to achieve the circulation switch was very large. However, because of the large uncertainties associated with deep time paleo-simulations, for example uncertainties in the bathymetry, we cannot rule out the possibility that an ocean circulation switch as suggested by Bice and Marotzke (2002) caused the methane hydrate dissociation.

The inhomogeneous vertical and zonal structure of the convection and meridional overturning in the Atlantic in our simulations challenges previous conclusions from 'deep water age' reconstructions, which are based on single, local ocean drilling sites. Nunes and Norris (2006) inferred southern-hemisphere deep water formation from carbon isotope data. We argue that the relatively shallow NADW-track in combination with South Atlantic convection and a northward flow of Antarctic bottom water in the eastern Atlantic, in other words, co-existing northern and southern hemisphere deep water formation, may also be consistent with the carbon isotope records. Our simulations do not show any increase in deep water formation in the northern hemisphere in response to increased pCO_2. Hence, our simulations do not support the notion of Nunes and Norris (2006) that the onset of the PETM was associated with a switch from southern hemisphere to northern hemisphere deep water formation.

5.2 Outlook

We speculate that fresh-water input from the Arctic into the North Pacific has the potential to inhibit North Pacific deep water formation in our PE simulations. Whether or not the Bering Strait was closed during the PE is currently under discussion (Winguth, personal communication). Thus, a possible extension of this study would be to test the sensitivity of our results against the closure of the Bering Strait.

A limitation of this study is the assumption of a globally homogeneous vegetation. One approach to overcome this limitation could be to perform additional land surface sensitivity runs with prescribed vegetation distributions (such as the one reconstructed by Utescher and Mosbrugger 2007). Another approach could be to include interactive vegetation.

The analysis of the standard ECHAM5 output fields combined with the simple EBM as a diagnostic tool has allowed us to constrain the mechanisms that, according to our simulations, caused the warm and sensitive PE climate. However, this model-diagnosis setup is limited. For example, it does not allow us to quantify the radiative effect of water vapour separately from the other greenhouse gases. We have to speculate that water vapour is one main driver of the large PE climate sensitivity, possibly even leading to a runaway climate. Using additional diagnostic tools (such as a multiple column

version of the ECHAM5 radiation scheme) may help to improve the understanding of our simulations, and of the PE climate.

5.3 Résumé

We present the first coupled late Paleocene to early Eocene (PE) climate model solution with moderate pCO_2 that shows relatively warm, sea-ice-free high latitudes, and still reasonably matches lower-latitude sea surface temperature reconstructions. Our runs do not support the notion that an ocean circulation switch triggered the Paleocene/Eocene Thermal Maximum (PETM). However, our results indicate that the PE climate was very sensitive to a variation of pCO_2, which implies that a relatively small input of carbon — possibly from methane hydrates — could have caused the warming during the PETM.

Appendix A

Modified tropopause diagnostic

The ozone parameterisation (Section 3.3) critically depends on the detection of a correct tropopause height. ECHAM5 comes with a module that computes the tropopause height following the definition of the first tropopause of the World Meteorological Organization (1992, WMO). However, we find that this tropopause module becomes inapplicable during the PE runaway climate for a CO_2 concentration of 1120 ppm. The tropopause module fails to detect the correct tropopause at low latitudes, and sets the diagnosed tropopause height to 200 hPa. Consequently, the ozone parameterisation does not remove the artificial ozone surplus from the upper troposphere (Figure A.1; compare to Figure 3.11e). Consequently, the runaway is artificially accelerated (Figure 3.9, red dashed line).

The first tropopause as defined by the WMO is the lowest level at which the lapse rate decreases to 2 K per 1000 m, provided also that the average lapse rate between this level and all higher levels within 2000 m does not exceed 2 K. In the ECHAM5 tropopause module, these criteria are only checked at limited model levels; the search algorithm has an upper and a lower pressure bound. These pressure bounds depend on the maximum and minimum pressure levels for the formation of convective clouds. We decrease the minimum pressure limit to allow for a tropopause search at greater heights. Moreover, we modify the WMO first tropopause definition such that a low temperature gradient is only accepted to define the correct tropopause height, if the lapse rate does not exceed 2 K per 1000 m within *5000 m* above that low gradient (instead of within 2000 m according to the WMO). This accounts for the larger distances between the (higher) levels at lower pressures. With these two modifications, the tropopause module detects correct tropopause heights during PE4 (Figure A.2).

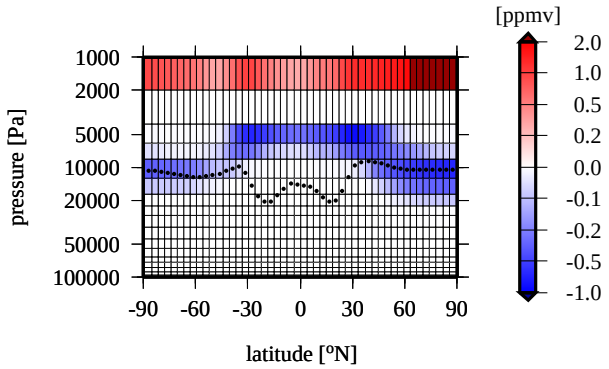

Figure A.1: Differences between the annual mean zonal mean ozone climatology as interpolated from Fortuin and Kelder (1998) and the ozone concentration averaged over the years 2470 to 2479 in the 1120 ppm run without the corrected tropopause detection algorithm; dotted line indicates the zonal mean tropopause height.

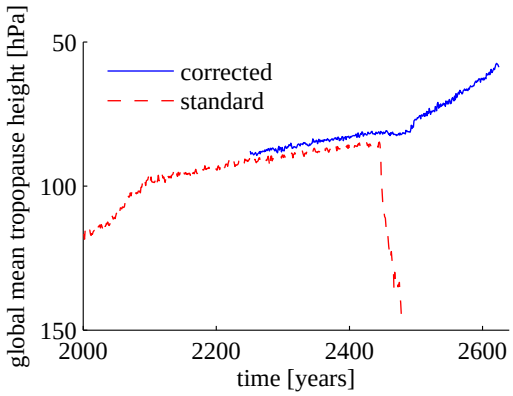

Figure A.2: Time series of the global mean tropopause height for the 1120 ppm run with the original WMO tropopause diagnostic as implemented in the standard version of ECHAM5 (red dashed), and for PE4 with the corrected algorithm for the tropopause detection (blue).

Bibliography

Abbot, D. S. and Tziperman, E.: Sea ice, high-latitude convection, and equable climates, Geophysical Research Letters, 35, 1–5, 2008.

Alley, R. B., Marotzke, J., Nordhaus, W., Overpeck, J., Peteet, D., Jr., R. P., Pierrehumbert, R., Rhines, P., Stocker, T., Talley, L., and Wallace, J. M.: Abrupt Climate Change: Inevitable Surprises, National Academy Press, 2002.

Arakawa, A. and Lamb, V. R.: Computational design of the basic dynamical processes of the CLA general circulation model, Methods Comput. Phys., 17, 173–265, 1977.

Archer, D.: Methane hydrate stability and anthropogenic climate change, Biogeosciences, 4, 521–544, 2007.

Barron, E. J.: Eocene equator-to-pole surface ocean temperatures: a significant climate problem?, Paleoceanography, 2, 729–739, 1987.

Berger, A. L.: Long Term Variations of Daily Insolation and Quaternary Climatic Changes, Journal of the Atmospheric Sciences, 35, 2362–2367, 1978.

Bice, K. L. and Marotzke, J.: Numerical evidence against reversed thermohaline circulation in the warm Paleocene/Eocene ocean, J. Geophys. Res., 106, 11 529–11 542, 2001.

Bice, K. L. and Marotzke, J.: Could changing ocean circulation have destabilized methane hydrate at the Paleocene/Eocene boundary?, Paleoceanography, 17, doi:10.1029/2001PA000 678, 2002.

Bowen, G. J., Beerling, D. J., Koch, P. J., Zachos, J. C., and Quattlebaum, T.: A humid climate state during the Paleocene/Eocene thermal maximum, Nature, 432, 495–498, 2004.

Brasseur, G. and Solomon, S.: Aeronomy of the Middle Atmosphere, D. Reidel Publishing Company, second revised edition, 1986.

Bretagnon, P. and Francou, G.: Planetary theories in rectangular and spherical variables - VSOP 87 solutions, Astronomy and Astrophysics, 202, 309–315, 1988.

Buffett, B. and Archer, D.: Global inventory of methane clathrate: sensitivity to changes in the deep ocean, Earth Planetary Science Letters, 227, 185–199, 2004.

Chapman, S.: On ozone and atomic oxygen in the upper atmosphere, Phil. Mag., 10, 369, 1930.

Corfield, R. M.: Palaeocene oceans and climate: An isotopic perspective, Earth-Science Reviews, 37, 225–252, 1994.

Covey, C. and Barron, E.: The Role of Ocean Heat Transport in Climatic Change, Earth-Science Reviews, 24, 429–445, 1988.

Denman, K. L., Brasseur, G., Chidthaisong, A., Ciais, P., Cox, P. M., Dickinson, R. E., Hauglustaine, D., Heinze, C., Holland, E., Jacob, D., Lohmann, U., Ramachandran, S., da Silva Dias, P. L., Wofsy, S. C., and Zhang, X.: Couplings Between Changes in the Climate System and Biogeochemistry, in: Climate Change 2007: The Physical Science Basis. Contribution of Working Group I to the Fourth Assessment Report of the Intergovernmental Panel on Climate Change [Solomon, S., D. Qin, M. Manning, Z. Chen, M. Marquis, K.B. Averyt, M. Tignor and H.L. Miller (eds.)], Cambridge University Press, Cambridge, United Kingdom and New York, NY, USA, 2007.

Dickens, G. R., O'Neil, J. R., Rea, D. K., and Owen, R. M.: Dissociation of oceanic methane hydrate as a cause of the carbon isotope excursion at the end of the Paleocene, Paleoceanography, 10, 965–971, 1995.

Endal, A. S. and Sofia, S.: Rotation of Solar Type Stars. I. Evolutionary Models for the Spin-down of the Sun, Astrophys. J., 243, 625–640, 1981.

Estes, R. and Hutchinson, J. H.: Eocene lower vertebrates from Ellesmere Island, Canadian Arctic Archipelago, Palaeogeography, Palaeoclimatology, Palaeoecology, 30, 325–347, 1980.

Fahey, D. W.: Twenty Questions and Answers About the Ozone Layer: 2006 Update, Scientific Assessment of Ozone Depletion: 2006 [Reprinted from *Scientific Assessment of Ozone Depletion: 2006*, Global Ozone Research and Monitoring Project - Report No. 50, 572 pp. World Meteorological Organization, Geneva, Switzerland, 2007], World Meteorological Organization, Geneva, Switzerland, 2007.

Forster, P., Ramaswamy, V., Artaxo, P., Berntsen, T., Betts, R., Fahey, D., Haywood, J., Lean, J., Lowe, D., Myhre, G., Nganga, J., Prinn, R., Raga, G., Schulz, M., and Dorland, R. V.: Changes in Atmospheric Constituents and in Radiative Forcing, in: Climate Change 2007: The Physical Science Basis. Contribution of Working Group I to the Fourth Assessment Report of the Intergovernmental Panel on Climate Change [Solomon, S., D. Qin, M. Manning, Z. Chen, M. Marquis, K.B. Averyt, M. Tignor

and H.L. Miller (eds.)], pp. 129–234, Cambridge University Press, Cambridge, United Kingdom and New York, NY, USA, 2007.

Fortuin, J. P. F. and Kelder, H.: An ozone climatology based on ozonesonde and satellite measurements, Journal of Geophysical Research - Atmospheres, 103, 31 709–31 734, 1998.

Fouquart, Y. and Bonnel, B.: Computations of solar heating of the earth's atmosphere: A new parameterization, Beitr. Phys. Atmos., 53, 35–62, 1980.

Gent, P. R., Willebrand, J., McDougall, T., and McWilliams, J. C.: Parameterizing eddy-induced tracer transports in ocean circulation models, J. Phys. Oceanogr., 25, 463–474, 1995.

Greenwood, D. R. and Scott, L. W.: Eocene continental climates and latitudinal temperature gradients, Geology, 23, 1044–1048, 1995.

Griffies, S. M.: The Gent-McWilliams skew flux, J. Phys. Oceanogr., 28, 831–841, 1998.

Hagemann, S.: Report No. 336: An Improved Land Surface Parameter Dataset for Global and Regional Climate Models, Tech. rep., Max Planck Institute for Meteorology, Hamburg, Germany, 2002.

Hagemann, S., Botzet, M., Dümenil, L., and Machenhauer, B.: Report No. 289: Derivation of global GCM boundary conditions from 1 km land use satellite data, Tech. rep., Max Planck Institute for Meteorology, Hamburg, Germany, 1999.

Handley, L., Pearson, P. N., McMillan, I. K., and Pancost, R. D.: Large terrestrial and marine carbon and hydrogen isotope excursions in a new Paleocene/Eocene boundary section from Tanzania, Earth and Planetary Science Letters, 275, 17–25, 2008.

Hibler, W. D.: A Dynamic Thermodynamic Sea Ice Model, J. Phys. Oceanogr., 9, 815–846, 1979.

Higgins, J. A. and Schrag, D. P.: Beyond methane: Towards a theory for the Paleocene-Eocene Thermal Maximum, Earth and Planetary Science Letters, 245, 523–537, 2006.

Huber, B. T., McLeod, K. G., and Wing, S. L.: Warm Climates in Earth History, Cambridge University Press, 2000.

Huber, M.: Climate Change: A Hotter Greenhouse?, Science, 321, 353–354, 2008.

Huber, M. and Sloan, L. C.: Heat transport, deep waters, and thermal gradients: Coupled simulation of an Eocene Greenhouse Climate, Geophys. Res. Let., 28, 3481–3484, 2001.

Huber, M., Sloan, L. C., and Shellito, C.: Early Paleogene oceans and climate: a fully coupled modelling approach using NCAR's CCSM, in: Wing, S.L., Gingerich, P.D., Schmitz, B., Thomas, E. (Eds.), Causes and Consequences of Globally Warm Climates in the Early Paleogene, Geological Society of America Special Paper Vol. 369, pp. 25–47, 2003.

Jacobson, M. Z.: Fundamentals of Atmospheric Modelling, Cambridge University Press, 1999.

Jungclaus, J. H., Keenlyside, N., Botzet, M., Haak, H., Luo, J.-J., Latif, M., Marotzke, J., Mikolajewicz, U., and Roeckner, E.: Ocean Circulation and Tropical Variability in the Coupled Model ECHAM5/MPI-OM, J. Climate, 19, 3952–3972, 2006.

Katz, M. E., Cramer, B. S., Mountain, G. S., Katz, S., and Miller, K. G.: Uncorking the bottle: What triggered the Paleocene/Eocene thermal maximum methane release?, Paleoceanography, 16, 549–562, 2001.

Kennett, J. P. and Stott, L. D.: Abrupt deep-sea warming, palaeoceanographic changes and benthic extinctions at the end of the Palaeocene, Nature, 353, 225–229, 1991.

Kump, L. R. and Pollard, D.: Amplification of Cretaceous Warmth by Biological Cloud Feedbacks, Science, 320, 195, 2008.

Kvenvolden, K.: Gas hydrates: Geological perspective and global change, Rev. Geophys., 31, 173–187, 1993.

Laskar, J., Robutel, P., Joutel, F., Gastineau, M., Correia, A. C. M., and Levrard, B.: A long term numerical solution for the insolation quantities of the Earth, Astronomy & Astrophysics, 428, 261–285, 2004.

Lin, S. J. and Rood, R. B.: Multidimensional flux-form semi-Lagrangian transport, Mon. Wea. Rev., 124, 2046–2068, 1996.

Lohmann, U. and Roeckner, E.: Design and performance of a new cloud microphysics parameterization developed for the ECHAM4 general circulation model, Climate Dyn., 12, 557–572, 1996.

Lott, F. and Miller, M. J.: A new subgrid-scale orographic drag parameterization: 1st formulation and testing, Quart. J. Roy. Meteor. Soc., 123, 101–127, 1997.

Luo, J.-J., Massen, S., Roeckner, E., Madec, G., and Yamagata, T.: Reducing climatology bias in an ocean-atmosphere CGCM with improved coupling physics, J. Climate, 18, 2344–2360, 2005.

Maier-Reimer, E., Mikolajewicz, U., and Crowley, T.: Ocean general circulation model sensitivity experiment with an open Central American Isthmus, Paleoceanography, 5, 349–366, 1990.

Markwick, P. J.: 'Equability,' continentality, and Tertiary 'climate': The crocodilian perspective, Geology, 22, 613–616, 1994.

Markwick, P. J.: Fossil crocodilians as indicators of Late Cretaceous and Cenozoic climates: implications for using palaeontological data in reconstructing palaeoclimate, Palaeogeography, Palaeoclimatology, Palaeoecology, 137, 205–271, 1998.

Marsland, S. J., Haak, H., Jungclaus, J. H., Latif, M., and Röske, F.: The Max-Planck-Institute global ocean/sea ice model with orthogonal curvilinear coordinates, Ocean Modelling, 5, 91–127, 2003.

McElroy, M. B.: Sources and Sinks of nitrous oxide, in: Proceedings of the Nato Advanced Study Institute on Atmospheric Ozone: Its Variation and Human Influences, pp. 345–364, U.S. Department of Transportation, Washington, D.C. 20591, 1980.

Miller, K. G., Janecek, T. R., Katz, M. E., and Keil, D. J.: Abyssal circulation and benthic foraminiferal changes near the Paleocene/Eocene boundary, Paleoceanography, 2, 741–761, 1987.

Mlawer, E. J., Taubman, S. J., Brown, P. D., Iacono, M. J., and Clough, S. A.: Radiative transfer for inhomogeneous atmospheres: RRTM, a validated k-correlated model for the longwave, J. Geophys. Res., 102, 16 663–16 682, 1997.

Nunes, F. and Norris, R. D.: Abrupt reversal in ocean overturning during the Palaeocene/Eocene warm period, Nature, 439, 60–63, 2006.

Pacanowski, R. C. and Philander, S. G. H.: Parameterization of vertical mixing in numerical models of tropical oceans, J. Phys. Oceanography, 11, 1443–1451, 1981.

Pagani, M., Caldeira, K., Archer, D., and Zachos, J. C.: An Ancient Carbon Mystery, Science, 314, 1556–1557, 2006a.

Pagani, M., Pedentchouk, N., Huber, M., Sluijs, A., Schouten, S., Brinkhuis, H., Damste, J. S. S., Dickens, G. R., and the Expedition 302 Scientists: Arctic hydrology during global warming at the Palaeocene/Eocene thermal maximum, Nature, 442, 671–675, 2006b.

Panchuk, K., Ridgwell, A., and Kump, L.: Sedimentary response to Paleocene-Eocene Thermal Maximum carbon release: A model-data comparison, Geology, 36, 315–318, 2008.

Pearson, P. N. and Palmer, M. R.: Atmospheric carbon dioxide concentrations over the past 60 million years, Nature, 406, 695–699, 2000.

Peltier, W. R.: Earth System History, in: Encyclopedia of Global Environmental Change, Volume One, The Earth system: physical and chemical dimensions of global environmental change, pp. 31–60, John Wiley and Sons, Ltd, 2003.

Randall, D., Wood, R., Bony, S., Colman, R., Fichefet, T., Fyfe, J., Kattsov, V., Pitman, A., Shukla, J., Srinivasan, J., Stouffer, R., Sumi, A., and Taylor, K.: Climate Models and Their Evaluation, in: Climate Change 2007: The Physical Science Basis. Contribution of Working Group I to the Fourth Assessment Report of the Intergovernmental Panel on Climate Change [Solomon, S., D. Qin, M. Manning, Z. Chen, M. Marquis, K.B. Averyt, M. Tignor and H.L. Miller (eds.)], pp. 589–662, Cambridge University Press, Cambridge, United Kingdom and New York, NY, USA, 2007.

Roeckner, E., Bäuml, G., Bonaventura, L., Brokopf, R., Esch, M., Giorgetta, M., Hagemann, S., Kirchner, I., Kornblueh, L., Manzini, E., Rhodin, A., Schlese, U., Schulzweida, U., and Tompkinsi, A.: The atmospheric general circulation model ECHAM5, Tech. rep., Max Planck Institute for Meteorology, Hamburg, Germany, available online at http://www.mpimet.mpg.de, 2003.

Röhl, U., Bralower, T., Norris, R., and Wefer, G.: New chronology for the late Paleocene thermal maximum and its environmental implications, Geology, 28, 927–930, 2000.

Royer, D. L., Wing, S. L., Beerling, D. J., Jolley, D. W., Koch, P. L., Hickey, L. J., and Berner, R. A.: Paleobotanical Evidence for Near Present-Day Levels of Atmospheric CO_2 During Part of the Tertiary, Science, 292, 2310–2313, 2001.

Schmidt, H., Brasseur, G. P., Charron, M., Manzini, E., Giorgetta, M. A., Diehl, T., Fomichev, V. I., Kinnison, D., Marsh, D., and Walters, S.: The HAMMONIA Chemistry Climate Model: Sensitivity of the Mesopause Region to the 11-Year Solar Cycle and CO2 Doubling, Journal of Climate, 19, 3903–3931, 2006.

Semtner, A. J.: A Model for the Thermodynamic Growth of Sea Ice in Numerical Investigations of Climate, J. Phys. Oceanogr., pp. 379–389, 1976.

Sewall, J. O., Sloan, L. C., Huber, M., and Wing, S.: Climate sensitivity to changes in land surface characteristics, Global and Planetary Change, 26, 445–465, 2000.

Sexton, A. J., Wilson, P. A., and Pearson, P. N.: Microstructural and geochemical perspectives on planktic foraminiferal preservation: 'Glassy' versus 'Frosty', Geochemistry Geophysics Geosystems, 7, 2006.

Shackleton, N. and Boersma, A.: The climate of the Eocene ocean, J. geol. Soc. London, 138, 153–157, 1981.

Shellito, C. J., Sloan, L. C., and Huber, M.: Climate model sensitivity to atmospheric CO_2 levels in the Early-Middle Paleogene, Palaeogeography, Palaeoclimatology, Palaeoecology, 193, 113–123, 2003.

Sloan, L. C.: Equable climates during the early Eocene: significance of regional paleogeography for North American climate, Geology, 22, 881–4, 1994.

Sloan, L. C. and Pollard, D.: Polar stratospheric clouds: A high latitude warming mechanism in an ancient greenhouse world, Geophysical Research Letters, 25, 3517–3520, 1998.

Sloan, L. C., Walker, J. C. G., and Jr., T. C. M.: Possible role of oceanic heat transport in early Eocene climate, Paleoceanography, 10, 347–356, 1995.

Sluijs, A., Schouten, S., Pagani, M., Woltering, M., Brinkhuis, H., Damste, J. S. S., Dickens, G. R., Huber, M., Reichart, G.-J., Stein, R., Matthiessen, J., Lourens, L. J., Pedentchouk, N., Backman, J., Moran, K., and the Expedition 302 Scientists: Subtropical Arctic Ocean temperatures during the Palaeocene/Eocene thermal maximum, Nature, 441, 610–613, 2006.

Svensen, H., Planke, S., Malthe-Soerenssen, A., Jamtveit, B., Myklebust, R., Eidem, T. R., and Rey, S. S.: Release of methane from a volcanic basin as a mechanism for initial Eocene global warming, Nature, 429, 542–545, 2004.

Sykes, L. R., McCanna, W. R., and lan L. Kafka: Motion of Caribbean Plate during last 7 million years and implications for earlier Cenozoic movements, Journal of Geophysical Research, 87, 10 656–10 676, 1982.

Tanré, D., Geleyn, J.-F., and Slingo, J. M.: First results of the introduction of an advanced aerosol-radiation interaction in the ECMWF low resolution global model, in: Aerosols and their climatic effects, pp. 133–177, 1984.

Thomas, D. J., Zachos, J. C., Bralower, T. J., Thomas, E., and Bohaty, S.: Warming the fuel for the fire; evidence for the thermal dissociation of methane hydrate during the Paleocene-Eocene thermal maximum, Geology, 30, 1067–1070, 2002.

Thomas, D. J., Bralower, T. J., and Jones, C. E.: Neodymium isotopic reconstruction of late Paleocene-early Eocene thermohaline circulation, Earth and Planetary Science Letters, 209, 309–322, 2003.

Thomas, E.: Cenozoic mass extinctions in the deep sea: What perturbs the largest habitat on Earth?, in: Mass extinctions and other large ecosystem perturbations: extraterrestrial and terrestrial causes, pp. 1–24, The Geological Society of America Special Paper 424, Boulder, CO, 2007.

Thomas, E. and Shackleton, N. J.: The Palaeocene-Eocene benthic foraminiferal extinction and stable isotope anomalies, Geological Society London, Special Publication, 101, 401–441, 1996.

Thomas, E., Brinkhuis, H., Huber, M., and Röhl, U.: An Ocean View of the Early Cenozoic Greenhouse World, Oceanography (special issue feature), 19, 94–103, 2006.

Trenberth, K. E. and Smith, L.: The mass of the atmosphere: A constraint on Global Analyses, Journal of Climate, 18, 864–875, 2005.

Tripati, A. and Elderfield, H.: Abrupt hydrographic changes in the equatorial Pacific and subtropical Atlantic from foraminiferal Mg/Ca indicate greenhouse origin for the thermal maximum at the Paleocene-Eocene Boundary, GEOCHEMISTRY GEOPHYSICS GEOSYSTEMS, 5, 2004.

Tripati, A. and Elderfield, H.: Deep-Sea Temperature and Circulation Changes at the Paleocene-Eocene Thermal Maximum, Science, 308, 1894–1898, 2005.

Utescher, T. and Mosbrugger, V.: Eocene vegetation patterns reconstructed from plant diversity - A global perspective, Palaeogeography, Palaeoclimatology, Palaeoecology, 247, 243–271, 2007.

Winguth, A., Shellito, C., Shields, C., and Winguth, C.: Response of Early Eocene Climate to Greenhouse Gas Forcing - A Model Study with CCSM3, Journal of Climate, submitted.

World Meteorological Organization: International Meteorological Vocabulary, Geneva: World Meteorological Organization, 1992.

Zachos, J., Rohl, U., Schellenberg, S., Sluijs, A., Hodell, D., Kelly, D., Thomas, E., Nicolo, M., Raffi, I., Lourens, L., McCarren, H., and Kroon, D.: Rapid Acidification of the Ocean During the Paleocene-Eocene Thermal Maximum, Science, 308, 1611–1615, 2005.

Zachos, J. C., Pagani, M., Sloan, L., Thomas, E., and Billups, K.: Trends, rhythms, and aberrations in global climate 65 Ma to Present, Science, 292, 686, 2001.

Zachos, J. C., Wara, M. W., Bohaty, S., Delaney, M. L., Petrizzo, M. R., Brill, A., Bralower, T. J., and Premoli-Silva, I.: A Transient Rise in Tropical Sea Surface

Temperature During the Paleocene-Eocene Thermal Maximum, Science, 302, 1551–1554, 2003.

Zachos, J. C., Schouten, S., Bohaty, S., Quattlebaum, T., Sluijs, A., Brinkhuis, H., Gibbs, S. J., and Bralower, T. J.: Extreme warming of mid-latitude coastal ocean during the Paleocene-Eocene Thermal Maximum: Inferences from TEX_{86} and isotope data, Geology, 34, 737–740, 2006.

Acknowledgement

I wish to thank my advisor Prof. Dr. Jochem Marotzke for his support, his reassuring trust, and his rational advice whenever I needed it. I would like to thank my co-advisor Dr. Johann H. Jungclaus for cheering me up, and for always taking the time to discuss whatever issues when I knocked on his door. Thanks to Prof. Dr. Detlef Stammer for chairing my panel meetings, and for his support especially during the change of topic.

I would like to thank the IMPRS-ESM and the ocean group at the MPI-M. It has been a pleasure to meet so many fellow students and colleagues, some of them became my friends. Special thanks to Dr. Antje Weitz and Cornelia Kampmann for their organisational and mental support. Thanks to 'the Comer Family' for financial support, and for very motivating roundtables. Thanks to the administration especially for dealing with my 'PhD-contract pause'. Thanks to the German Climate Computation Centre, and to the Central IT Services for their technical support.

I would like to thank Dr. Karen L. Bice for providing the paleo-reconstruction of the PE topography, for interesting discussions, and for her kind hospitality during my short stay in Woods Hole. I wish to thank Dr. Robin S. Smith. He pointed out to me that my runaway simulations may be artificially caused by too high ozone concentrations in the troposphere. That saved this work. Thanks also to Dr. Sebastian Rast and Dr. Hauke Schmidt for their help implementing the ozone parameterisation. I would also like to thank Dr. Marco Giorgetta, Dr. Sebastian Rast, Dr. Erich Roeckner, and Dr. Monika Esch for their support while I was searching for the numerical instability that led to so many of the beloved lookup-table-overflows. I would like to thank Dr. Helmuth Haak, Michael Botzet, and Dr. Stephan Lorenz for their support and their interest in my work, and Dr. Uwe Mikolajewicz for (admittedly tough but) very helpful discussions.

Thanks especially to Minke Beckmann, Stefanie Wykarius, Anke Bachmann, Yvonne Schmitz, Aiko Voigt, Nils Fischer, Florian Rauser, Anne-Kristin Anweiler, Antje Tittebrand, Martin Scharffenberg, Steffen Grünler, Sascha Hölig, Ronny Petrik, Dr. Rita Seiffert, Fanny Adloff, Annette Lilje, Freja Vamborg, Dr. Dirk Notz, Rosina Grimm, Daniel Bakosch, Maria Paz Chidichimo, Anna Kildemoes, Dr. Dirk Rannacher, and Waldemar Matis for their supporting and/or distracting company, for absorbing frustration, and for making me feel comfortable in Hamburg. I would like to thank my sister, my brother-in-law, and my parents for their support throughout my studies.

Die gesamten Veröffentlichungen in der Publikationsreihe des MPI-M
„Berichte zur Erdsystemforschung“,
„Reports on Earth System Science“,
ISSN 1614-1199

sind über die Internetseiten des Max-Planck-Instituts für Meteorologie erhältlich:

http://www.mpimet.mpg.de/wissenschaft/publikationen.html



ISSN 1614-1199